Title
Structure, Mechanics and Synthesis of Nanoscale Carbon and Boron Nitride

Permalink
https://escholarship.org/uc/item/7cc4c33d

Author
Rousseas, Michael

Publication Date
2013

Peer reviewed|Thesis/dissertation

Structure, Mechanics and Synthesis of Nanoscale Carbon and Boron Nitride

by

Michael Rousseas

A dissertation submitted in partial satisfaction of the
requirements for the degree of
Doctor of Philosophy

in

Physics

in the

Graduate Division

of the

University of California, Berkeley

Committee in charge:

Professor Alex Zettl, Chair
Professor Feng Wang
Professor Liwei Lin

Fall 2013

Structure, Mechanics and Synthesis of Nanoscale Carbon and Boron Nitride

Abstract

Structure, Mechanics and Synthesis of Nanoscale Carbon and Boron Nitride

by

Michael Rousseas

Doctor of Philosophy in Physics

University of California, Berkeley

Professor Alex Zettl, Chair

This thesis is divided into two parts. In Part I, we examine the properties of thin sheets of carbon and boron nitride. We begin with an introduction to the theory of elastic sheets, where the stretching and bending modes are considered in detail. The coupling between stretching and bending modes is thought to play a crucial role in the thermodynamic stability of atomically-thin 2D sheets such as graphene.

In Chapter 2, we begin by looking at the fabrication of suspended, atomically thin sheets of graphene. We then study their mechanical resonances which are read *via* an optical transduction technique. The frequency of the resonators was found to depend on their temperature, as was their quality factor. We conclude by offering some interpretations of the data in terms of the stretching and bending modes of graphene.

In Chapter 3, we look briefly at the fabrication of thin sheets of carbon and boron nitride nanotubes. We examine the structure of the sheets using transmission and scanning electron microscopy (TEM and SEM, respectively). We then show a technique by which one can make sheets suspended over a trench with adjustable supports. Finally, DC measurements of the resistivity of the sheets in the temperature range $600 - 1400$ °C are presented.

In Chapter 4, we study the folding of few-layer graphene oxide, graphene and boron nitride into 3D aerogel monoliths. The properties of graphene oxide are first considered, after which the structure of graphene and boron nitride aerogels is examined using TEM and SEM. Some models for their structure are proposed.

In Part II, we look at synthesis techniques for boron nitride (BN). In Chapter 5, we study the conversion of carbon structures of boron nitride *via* the application of carbothermal reduction of boron oxide followed by nitridation. We apply the conversion to a wide variety of morphologies, including aerogels, carbon fibers and nanotubes, and highly oriented pyrolytic graphite.

In the latter chapters, we look at the formation of boron nitride nanotubes (BNNTs). In Chapter 6, we look at various methods of producing BNNTs from boron droplets, and introduce a new method involving injection of boron powder into an induction furnace. In Chapter 7 we consider another useful process, where ammonia is reacted with boron vapor

generated *in situ*, either through the reaction of boron with metal oxides or through the decomposition of metal borides.

To Epaminondas Rousseas

Contents

II Synthesis of Boron Nitride Nanostructures 57

List of Figures

List of Tables

Acknowledgments

Thanks to my teachers, mentors, friends, classmates, and co-workers; I am lucky and honored to have worked and explored with you.

Part I

Structure and Mechanics of Nanoscale Carbon and Boron Nitride

Chapter 1

Elastic Properties of Sheets

Figure 1.1 shows a remarkable image; it is of a single atomic layer of sp^2-bonded carbon, a graphene membrane, suspended over an aperture 50 microns in diameter. Despite having a tear in it, the membrane is able to support itself (and a good deal of polymer residue on its surface) over a length 500,000 times its effective thickness. As discussed in Reference [1], the membrane owes this exceptional aspect ratio to its elastic properties, i.e. its high Young's modulus and bending rigidity.

We begin our discussion with a brief overview of the elastic properties of 2D sheets. Elastic theory is a beautiful subject, but unfortunately one that is no longer covered in physics programs. The approach taken here is to get to the essential results we'll need for studying graphene resonators in the next chapter.

A 2D sheet differs from a 3D solid in that it can be *bent* as well as *stretched*. In the parlance of the quantum theory of solids, these correspond to the out-of-plane and in-plane phonon modes, respectively. In this regard, sheets are not purely 2D systems, in that they

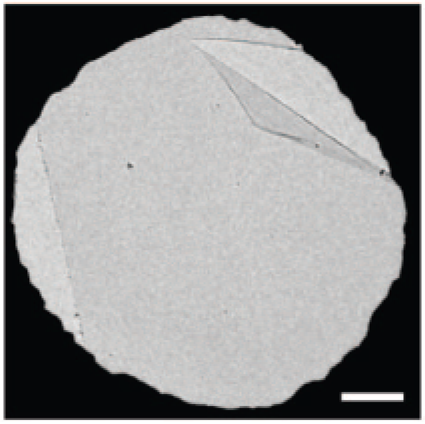

Figure 1.1: A large-area suspended graphene membrane. Scale bar 5 microns. Adapted from Reference [1].

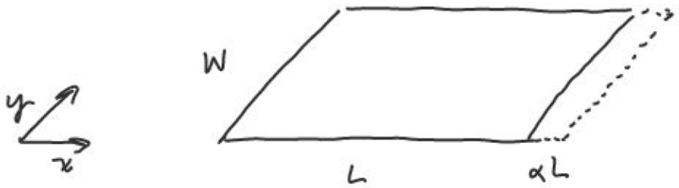

Figure 1.2: A stretched sheet.

have a third degree of freedom which affects their overall shape in 3D space. Anharmonic coupling between the stretching and bending modes of graphene are thought to play an important role in its overall thermodynamic stability, making sheets like those shown in Figure 1.1 possible. We'll touch briefly on this subject at the end of the chapter.

1.1 Stretching

Before considering the bending of a sheet, we'll walk through a simple and familiar example, that of calculating the amount of energy it takes to stretch an elastic sheet in one direction. Let's imagine we he have a sheet of material of width W and length L which is clamped at one end and we stretch it an amount $\Delta L = \epsilon L$ in the x direction by applying a force F to the other end, where ϵ is the strain. The situation is depicted in Figure 1.2. The force distributes itself throughout the length of the sheet, and we expect that for small displacements ΔL, that the material should act like a spring with stiffness k, so that the force obeys Hooke's law: $F = kx$. Intuitively, this stiffness should scale proportionally to the width and inversely with the length, so that $k = YW/L$. The constant Y is a property of the material called the *2D Young's modulus* for obvious reasons; it has units of N/m.

When we stretch the sheet it contracts in the orthogonal direction by an amount $\Delta W = \nu\epsilon W$ due to the Poisson effect, where ν is the *Poisson ratio* of the material. However, this contraction is perpendicular to the applied force, so doesn't affect the total energy. There is a second-order effect since the length along which the force acts is shortened, but we ignore this because the strain is generally assumed to be small.

The amount of energy it takes to stretch the sheet is then

$$E_s = \int_0^{\epsilon L} F dx = \frac{YW}{L} \int_0^{\epsilon L} x \; dx = \frac{YWL\epsilon^2}{2}$$

We see that the total energy scales with the area of the sheet. The energy per unit area is then

$$\frac{E_s}{A} = \frac{1}{2} Y \epsilon^2 \tag{1.1}$$

where $A = LW$ is the area of the sheet.

If we follow this argument through with 3D elastic theory, with a material of Young's modulus E and thickness h and compare the answers, we find that

$$Y = Eh \tag{1.2}$$

When we measure the Young's modulus of the material like graphene, which is reported to be around 1 TPa, what we're actually measuring is the 2D Young's modulus Y. To quote a 3D Young's modulus, we have to put in some number for h, which is conventionally taken to be the interlayer spacing of graphite, or about 0.335 nm, yielding $Y \approx 340$ N/m (see discussion below). This choice for h is, of course, completely arbitrary.

In the general case, where the strains in the sheet vary as a function of (x, y), we describe the deformation of the sheet in terms of the vector $\vec{u}(x, y)$, which gives the displacement of the area element at (x, y) under the deformation. For example, in the example above, we have $\vec{u}(x, y) = \epsilon(x\hat{x} + \nu y\hat{y})$. The stretching energy is then given by

$$E_s = \frac{1}{2}\iint \sigma_{ij} u_{ij} dxdy \tag{1.3}$$

where the indices i and j are summed over x and y. The tensor u_{ij} is the *strain tensor*, whose components are given by

$$u_{ij} = \frac{1}{2}\left(\partial_i u_j + \partial_j u_i\right) \tag{1.4}$$

where $\partial_x = \partial/\partial x$, $\partial_y = \partial/\partial_y$ (formally, we reduce the equations of 3D elasticity by assuming requiring that $u_z = 0$ and that u_x and u_y are independent of z, which is referred to as *plane strain*). The *2D stress tensor* σ_{ij} is given by

$$\sigma = \frac{Y}{1-\nu^2}\begin{pmatrix} u_{xx} + \nu u_{yy} & (1-\nu)u_{xy} \\ (1-\nu)u_{xy} & u_{yy} + \nu u_{xx} \end{pmatrix} \tag{1.5}$$

Note here that in our notation we incorporate the thickness into the stress tensor, so that it has units of N/m; that is, a *surface stress* or *surface tension.* An intuitive way to think about the surface stress is to imagine that we cut a slit in the sheet; the surface stress is then the force per unit length necessary to pull the sheet back together.

In the important case of *biaxial strain*, where $u_x = \epsilon x$, $u_y = \epsilon y$, we have

$$\sigma_{xx} = \sigma_{yy} = Y\epsilon/(1-\nu) \tag{1.6}$$

so that

$$\frac{E_s}{A} = \frac{Y\epsilon^2}{1-\nu} \tag{1.7}$$

where the factor of $1 - \nu$ in the denominator accounts for the extra energy required to counteract the Poisson effect.

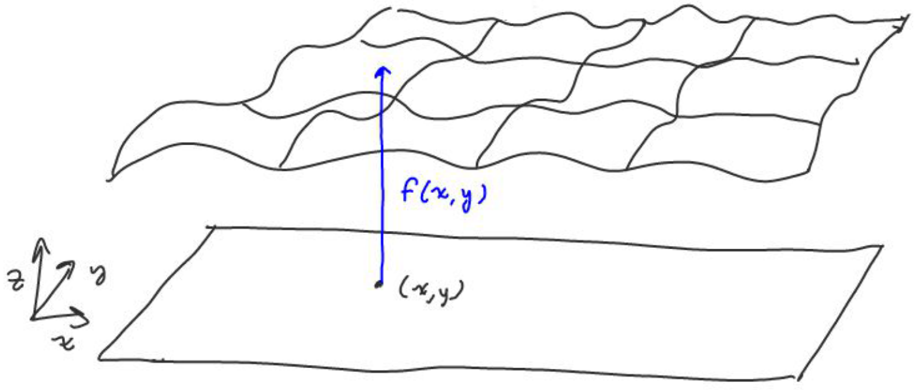

Figure 1.3: A rippled sheet. The sheet lies more or less flat parallel to the xy plane, and its height above the plane is described by $z = f(x, y)$.

Membranes

Suppose now we have a sheet to which we apply a large biaxial stress, and we perturb it, so that it comes out of the xy plane slightly by an amount $f(x, y)$. The situation is depicted in Figure 1.3. The sheet acquires a small additional strain on it, which can now vary along the sheet. The corresponding energy is given by [2]

$$E_s = \text{const.} + \frac{\sigma}{2} \int |\nabla f|^2 \, dA \tag{1.8}$$

Using this energy, we can form a Lagrangian and find the equations of motion. We get

$$\sigma \nabla^2 f = \rho \, \partial_t^2 f - P \tag{1.9}$$

which is known as *Poission's equation*, which is familiar from electrostatics. Here P is the applied force per unit area on the sheet in the z direction. The boundary conditions can be given by either specifying ∇f or f at the boundary of the sheet; we usually use $f = 0$ at the boundary, since we usually draw sheets over a stable rim in order to apply the biaxial stress.

The solutions of course depend on the geometry of the rim and the nature of the surface forces P. To begin with, we'll ignore the surface forces and consider the free vibrations of the membrane. We assume a time dependence $e^{-i\omega t}$, which takes care of the time derivatives to yield

$$\sigma\nabla^2 f + \rho \, \omega f = 0$$

For a square rim with sides of length L, we have the solutions

$$f_{nm}(x, y) = A \sin(k_n x) \sin(k_m y) \tag{1.10}$$

where $k_n = n\pi/L$ where n is a positive integer which serve to label the normal modes of the system. Plugging this solution back into the equation of motion, we get the mode frequencies

$$\omega = \sqrt{\frac{\sigma}{\rho}\left(k_n^2 + k_m^2\right)} \tag{1.11}$$

For a circular memebrane of radius a, the solutions are

$$f_{mn}(r,\theta) = AJ_m(k_{mn}r)\cos(m\theta) \tag{1.12}$$

where J_m is the m^{th} order Bessel function and $k_{mn} = b_{mn}/a$ where b_{mn} is the n^{th} zero of the m^{th} order Bessel function. We list the mode frequencies for reference in Table 1.1.

	$m = 0$	$m = 1$	$m = 2$	$m = 3$
$n = 1$	$\frac{2.405}{2\pi a}\sqrt{\frac{\sigma}{\rho}}$	$1.594 f_{01}$	$2.136 f_{01}$	$2.653 f_{01}$
$n = 2$	$2.296 f_{01}$	$2.918 f_{01}$	$3.501 f_{01}$	$4.060 f_{01}$

Table 1.1: Normal mode frequencies of a circular membrane. Adapted from Reference [3]

1.2 The 2D Young's Modulus of Graphene

The 2D Young's modulus of graphene was first measured directly by Lee *et al.* using a nanoindentation technique. [4] Graphene flakes were exfoliated over circular trenches in a silicon wafer, and an atomic force microscope (AFM) was used to measure the force vs. displacement curves of the resulting membranes. The group determined a value of $Y = 340 \pm 50$ N/m, as quoted above. They also noticed that membranes fabricated in this manner tended to have a remarkably high prestress, up to 0.74 N/m. In the same study, they determined a breaking strength of 42 N/m, *i.e.* the maximum stress that could be applied to a pristine graphene membrane before failure.

1.3 Bending

Now let's consider our thin sheet of material, which is clamped at one end, and instead of stretching, we bend it by appyling a torque to the end of the sheet, which analogously to the stretched case, distributes itself evenly throughout the sheet. The situation is depicted in Figure 1.4. We'll assume without proof that the sheet describes a circular arc throughout the bending. Again, there is a second-order correction which is necessary to keep the distance from the clamp constant, but we again assume that the total angle Θ through which we apply the torque, which is analogous to the strain, is generally small.

In analogy with the stretching of the sheet, we argue that the torque necessary to bend the sheet through an angle θ is $\tau = c\theta$, and that the constant c, which here represents

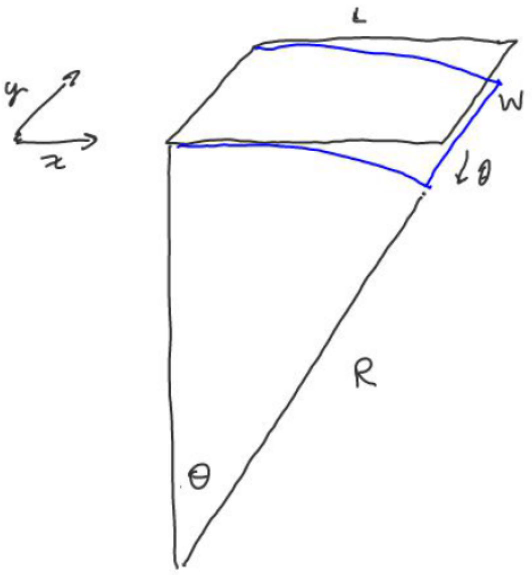

Figure 1.4: A bent sheet.

the bending stiffness, is likewise proportional to the width and inversely proportional to the length: $c = \kappa W/L$. The constant κ is called the *bending rigidity* or *flexural rigidity* of the material; it has units of energy. The total energy necessary to bend the sheet through an angle $\Theta = L/R$ is then

$$E_b = \int_0^{L/R} \tau \, d\theta = \frac{\kappa W}{L} \int_0^{L/R} \theta \, d\theta = \frac{\kappa L W}{2R^2}$$

We see that the total bending energy scales with the area of the sheet, and is inversely proportional to the square of the radius of curvature. The bending energy per unit area is

$$\frac{E_b}{A} = \frac{1}{2}\kappa S^2 \tag{1.13}$$

where $S = 1/R$ is the *curvature* of the sheet.

As an example, let's use this expression to consider the bending energy per unit length of a carbon nanotube, which is often described as a rolled-up strip of graphene. The bending rigidigy of graphene is somewhere in the neighborhood of 1.0 to 1.5 eV; we'll discuss this more below. For a nanotube of radius R, the total bending energy per unit length is then $E_{tube} = \pi\kappa/R$; for a nanotube of diameter 1 nm, this gives an bending energy of about 3.1 to 4.7 eV per nanometer of length. For the tube to be stable, this should be less than the energy gained in the formation of the carbon-carbon bonds at the edges of the original graphene strip, which have an energy of about 5.0 eV, or in the zig-zag direction, about 20 eV per nanometer. Of course, for small diameter tubes, we expect that our linear assumptions will eventually break down.

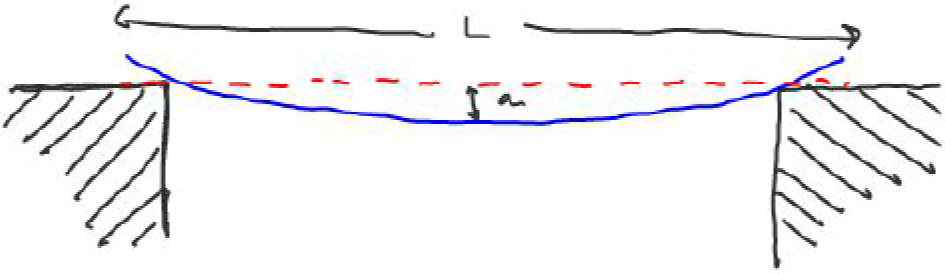

Figure 1.5: A simply supported elastic sheet.

As another simple example, let's consider a sheet of length L and width W that is laid across two supports. We'll ignore the effects of gravity here, except that it keeps the sheet on the supports. Suppose we bend the sheet down at it center by an amount $a \ll L$ as shown in Figure 1.5. Assuming that the curvature is roughly constant, the radius of curvature of the sheet is $R \approx L^2/8a$, so that the bending energy per unit area is

$$\frac{E_b}{A} = \frac{\kappa}{2R^2} \approx \frac{1}{2}\frac{64\kappa}{L^4}\,a^2$$

which is similar to that of a harmonic oscillator displaced from its equilibrium by an amount a. If ρ is the mass per unit area of the sheet, we expect the frequency of small vibrations to go like

$$\omega \sim \frac{8}{L^2}\sqrt{\frac{\kappa}{\rho}}$$

which we'll verify below.

Elastic Thickness

As in the case of stretching, the bending of the sheet can be described with appropriate approximations using 3D elastic theory and a sheet of thickness h. The basic idea is that the inside layers of the material are compressed upon bending, while the outside ones are stretched. The result is that bending rigidity can be related to the Young's modulus according to [5]

$$\kappa = \frac{Eh^3}{12(1-\nu^2)} \tag{1.14}$$

There is also an analogy to the Poisson effect: bending in one direction induces bending in the opposite direction, in a direction orthogonal to the applied torque, as you can verify by bending a rubber eraser between your fingers. In 3D materials this follows from the Poisson effect, since the layers on the inside of the curve expand along the axis of curvature, while those on the outside contract.

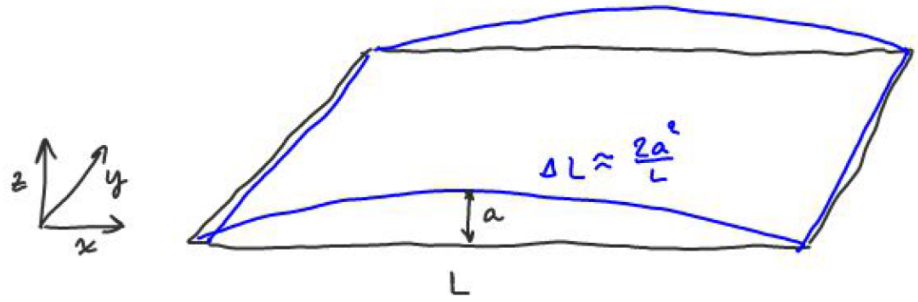

Figure 1.6: A bent and stretched sheet. The original length of the sheet is L, and a stress applied to stretch it into a circular cylindrical arc with a height a above its original plane.

For a 2D material, we can use Equation 1.14 in combination with Equation 1.2 for the 2D Young's modulus to define the *elastic thickness*

$$h_e \equiv \sqrt{\frac{12(1-\nu^2)\kappa}{Y}} \tag{1.15}$$

For graphene, we have $h_e \approx 0.1$ nm. In some sense, this defines the mechanical "thickness" of a graphene sheet.

To understand the significance of the elastic thickness, consider a thin sheet of length L clamped at two ends so that it is initially unstrained, and subject it to a constant curvature S so that bulges out of its original plane by an amount a, as in Figure 1.6. If $a \ll L$, the strain induced by the bulge is approximately $\epsilon \approx 2a^2/L^2$, meaning that the stretching energy per unit area is $E_s/A \approx 2Ya^4/L^4$. The curvature of the surface is meanwhile $S \approx 8a/L^2$, so that the bending energy density is $E_b/A \approx 32\kappa a^2/L^2$. The ratio of these two energies is then

$$\frac{E_s}{E_b} \approx \frac{Ya^2}{16\kappa} \approx \frac{a^2}{h_e^2}$$

The stretching energy quickly dominates over the bending energy as the height of the bulge grows past the elastic thickness, independent of the length of the sheet. On the other hand, it means that a sheet will almost always bend out of plane to accommodate any strain. Suppose we have a square sheet of area A and we heat it up so that it expands, causing a thermal strain ϵ. If the sheet remains flat, its energy goes like $E_s \sim AY\epsilon^2$, while if it bends, it goes like $E_b \sim \kappa\epsilon$, meaning that for $\epsilon \gtrsim h_e^2/A$, the sheet will bend instead of compress to minimize its total energy.

General Bending

For the general case of bending in two orthogonal directions, the situation gets a bit more complicated. To begin, it is intuitively clear that any such bending would require *stretching* the sheet as well. We ignore this stretching energy for the time being; in the next section we'll consider it more carefully.

In the cases we'll be interested in here, the bending of the sheet is generally slight, so that the surface is mostly flat and contains ripples. The situation is identical to that of the membrane, except that there is no applied biaxial strain. In these cases, we can lay the surface generally parallel to the xy plane and describe its out of plane fluctuations by a function $f(x, y)$, which gives the height of the surface above the plane. The general assumption is the that normal vector to the surface is roughly parallel to $\hat{z}$, so that we can estimate the curvature by simply calculating the second derivatives of $f(x, y)$ as we do in elementary calculus. The expression for the bending energy is then given approximately by [2]

$$E_b = \frac{\kappa}{2(1-\nu^2)} \iint \left(\nabla^2 f\right)^2 dA \tag{1.16}$$

where $\nabla^2 = \partial_x^2 + \partial_y^2$ is the Laplacian operator. The integrand in the equation is the square of the *mean curvature* of the surface at the point (x, y). Its geometric interpretation is that if we take a point on the surface and consider all the vertical cross-sections of the curve, there will be two cross-sections which are perpendicular to one another which have the greatest and least curvature, respectively (they can also have the same curvature). These are called the *principle curvatures* of the surface at that point. The mean curvature is just the average of these two curvatures.

Finally, we mention that there is another term in the bending energy which we have not included and is associated with the *Gaussian curvature* of the surface, which is the product of the principle curvatures. It plays an important role in determining the boundary conditions when we consider the equations of motion for sheets with a fixed boundary.

It is also important in the non-linear coupling between bending and stretching modes, since regions of non-zero Gaussian curvature must necessarily be stretched as well as bent. This is the content of the Gauss-Bonnett theorem, which has applications throughout physics; for example, topological insulators.

1.4 Bending Rigidity of Graphene

The bending rigidity of multilayer graphene flakes was measured by Poot and van der Zant using a nano-indentation technique and was found to comply with the h^3 dependence given by classical elastic theory.[6]. However, later studies by Lindahl et al. where the bending rigidity is deduced from the snap-through instability of buckled, suspended few-layer sheets, give a a different result and show that the bending rigidity of one to three layer sheets deviates significantly from the classical result.[7] The authors stress, however, that the estimate is very rough, and unreliable due to the small number of data points available. The analysis is also rather indirect, and depends on a model of snap-through instability that may not be applicable to ultrathin membranes.

On the theoretical end, various calculations point to a value of $\kappa \approx$ 1.0 to 1.5 eV, which is an order of magnitude lower than that expected from Equation 1.14 if extrapolated from measurement of bulk graphite, using $h \approx 0.335$ nm, the interlayer spacing of graphite. This is not at all unexpected, since the derivation of Equation 1.14 depends of the fact that the top layers of the material are stretched while those on the inside are compressed; for single-layer graphene, there are no additional layers involved, and the rigidity instead derives from the overlap of atomic orbitals on either side of the basal plane.[8]

In one approach, one looks at the phonon spectrum of the out-of-plane modes of graphite. As shown below, the dispersion relation for these modes is quadratic it k, and the bending rigidity can be deduced from the curvature.[9] This gives a bending rigidity of 1.2 eV. In another approach, one can model directly the orbital overlap as function of the bond angles and dihedral angles of the basal plane, which gives a prediction of 1.4 eV.[10]. *Ab initio* calculations can also be done, which give similar values. [11]

To my knowledge there has been no direct measurement of the bending rigidity of graphene. In the next chapter, we approach this problem from the study of the resonance frequencies of untensioned graphene resonators, the equations of motion for which we turn to next.

1.5 Bending Equations of Motion

If we can ignore the stretching energy, the equations of motion for a bent surface can be found by performing a functional variation of the bending energy given by Equation 1.16. The math is quite involved and can be found beautifully explained in Landau and Lifchitz.[5] Including time dependence, the result is

$$\kappa \, \nabla^4 g(x, y, t) = P(x, y, t) - \rho \, \frac{\partial^2 f}{\partial t^2} \tag{1.17}$$

where P is the applied force per unit area on the sheet in the $\hat{z}$ direction and ρ is the mass per unit area. The operator $\nabla^4 = (\nabla^2)^2 = \partial_x^4 + 2\,\partial_x^2\,\partial_y^2 + \partial_y^4$ is known as the *biharmonic operator*, and Equation 1.17 as the *biharmonic equation.* On the surface, it closely resembles Poisson's equation for a membrane. However, since the equation is fourth-order in the derivatives, we must specify boundary conditions both for the value *and* the derivatives of f at the boundary. As mentioned above, these boundary conditions come from the variation of the Gaussian term in the bending energy. Examples of boundary conditions are

- clamped, so that both f and $\nabla f = 0$ at the boundary.
- simply supported, where $f = 0$; in this case, the boundary condition on ∇f is complicated; for the simple case of a circular sheet, it simplifies to [5]

$$\frac{\partial^2 f}{\partial r^2} + \frac{\nu}{r}\frac{\partial f}{\partial r} = 0$$

while for a square plate, we have [12]

$$\frac{\partial^2 f}{\partial x^2} + \nu \frac{\partial^2}{\partial y^2}$$

where the derivatives are evaluated along the edge in the $\hat{y}$ direction; a similar expression holds for those along the $\hat{x}$ direction.

- free, where the plate is simply suspended or is held by a point at the center, like a crash cymbal in a drum kit. The boundary conditions are even more complicated here; see Reference [5]

For simplicity, we'll take $P(x, y) = 0$ and consider oscillatory motion $g(x, y, t) = f(x, y)e^{-i\omega t}$, where ω is the circular frequency of the motion. The equation becomes

$$\kappa \nabla^4 f(x, y) = \omega^2 \rho f(x, y)$$

For a simply supported square plate with sides of length L, we try harmonic solutions

$$f_{mn}(x, y) = A_{nm} \sin(nkx) \sin(mky) \tag{1.18}$$

where m and n are positive integers and $k = \pi/L$. The resulting dispersion relation is

$$\omega_{mn} = k^2 \left(m^2 + n^2\right) \sqrt{\frac{\kappa}{\rho}} \tag{1.19}$$

Compared to a square membrane, the mode frequencies have a different spacing, and importantly, *bending modes are dispersive*, with a wavelength dependent velocity. When considering a 2D crystal, Equation 1.19 gives the dispersion relation of long-wavelength, out-of-plane phonons. This is turn has important consequences when considering the thermal expansion and overall stability of the crystal.

In the next chapter, we'll want to also consider the case of circular clamped sheet. It's clear form the boundary conditions that the simple membrane solutions involving ordinary Bessel functions won't work, since the derivative cannot generally vanish at the boundary. Instead, we must combine them with *hyperbolic Bessel functions* I_m, so that the normal modes become [3]

$$f_{mn}(r, \theta) = [A J_m(k_{mn} r) + B I_m(k_{mn} r)]\, cos(m\theta) \tag{1.20}$$

The frequencies of the first few modes are given for reference in Table 1.2.

1.6 Bending and Stretching

As mentioned above, stretching and bending are intimately coupled in a sheet, especially when the amount of bending exceeds the elastic thickness. Formally, this coupling is

	$m=0$	$m=1$	$m=2$	$m=3$
$n=1$	$\frac{1.63}{a}\sqrt{\frac{\kappa}{\rho}}$	$2.08f_{01}$	$3.41f_{01}$	$5.00f_{01}$
$n=2$	$3.89f_{01}$	$5.95f_{01}$	$8.28f_{01}$	$10.87f_{01}$

Table 1.2: Normal mode frequencies of a clamped circular sheet. Adapted from Reference [3]

expressed through the strain tensor. The displacement vector is written as $\vec{u}(x,y) = u_x(x,y)\hat{x} + u_y(x,y)\hat{y} + f(x,y)\hat{z}$, and in place of Equation 1.4 for the strain tensor, we have

$$u_{ij} = \frac{1}{2}\left(\partial_i u_j + \partial_j u_i + \partial_i f\,\partial_j f\right)$$

Using both the stretching and bending energies given by Equations 1.3 and 1.16, we can perform a functional variation and derive the equations of motion for elastic plates. The additional terms in strain tensor involving the product of the derivatives of f account for the additional strain due to bending; since this term is quadratic in the derivatives, it leads to non-linear equations of motion. The results are known as the *Foppl-von Karaman equations*

$$\kappa\,\nabla^4 f - \partial_j(\,\sigma_{ij}\partial_i f\,) = P - \rho\frac{\partial^2 f}{\partial t^2} \tag{1.21}$$

$$\partial_j \sigma_{ij} = 0 \tag{1.22}$$

where the stress tensor σ_{ij} is given by Equation 1.5. They are three coupled, non-linear differential equations for the three components of the displacement vector $\vec{u}(x,y)$. In all known cases, the equations have no known closed-form solution and approximations must be made.

One approximation we can make is that the stresses are uniform, *i.e.* we use a biaxial stress as in Section 1.1 and simply bring the term out from the derivative. The resulting equation is

$$\kappa\nabla^4 f - \sigma\nabla^2 f = P - \rho\frac{\partial^2 f}{\partial t^2} \tag{1.23}$$

where $\sigma = Y\epsilon/(1-\nu)$, which automatically satisfies Equation 1.22. This equation can describe, for example, a membrane which is slightly stiffened by its bending rigidity. Using the solutions compatible for both a simply supported sheet and a membrane, we have the dispersion relation

$$\omega = \sqrt{\frac{\kappa}{\rho}\,k_{mn}^4 + \frac{\sigma}{\rho}\,k_{mn}^2} \tag{1.24}$$

1.7 Thermodynamics of 2D Systems

Before leaving this topic, we mention briefly an important topic involving bending and stretching modes in a 2D system. The story goes back to an argument first present by

Landau and Peirles in the 1930's, and later expanded by Mermin and Wagner, who argued that 2D crystals are inherently unstable. The heart of the argument rests in the height-height correlation function of the sheet, which can be calculated using the bending energy, Equation 1.16. The result is [13]

$$\langle h^2 \rangle \sim L^2 \tag{1.25}$$

where L is the sample size. This relation implies that the out-of-plane fluctuations of the sheet grow with its size, which contradicts the basic assumption in writing down Equation 1.16 that the fluctuations are small. A similar situation emerges when one calculates the normal-normal correlation function, which gives the fluctuations in the orientation of different parts of the sheet.

$$\langle \hat{n}(0) \cdot \hat{n}(R) \rangle \sim \log R \tag{1.26}$$

where R is the separation between the parts of the sheet; this expression diverges with growing sheet separation and again contradicts our basic assumption of small gradients.

The solution around this problem is to take into account the non-linear coupling between the bending and stretching modes, which is captured in Equation 1.21. Nelson has argued that the effect of the non-linear coupling is to stiffen the bending rigidity at large wavelengths, according to

$$\kappa_R(\vec{q}) \sim \frac{\sqrt{k_B T K_0}}{q} \tag{1.27}$$

where k_B is Boltzman's constant, T is the temperature, andK_0 is an elastic coupling constant. [2] For graphene, $K_0 \approx 0.218$ eV/nm^2. This expression is valid for small q. Using this expression, one finds that the normal-normal correlation function remains finite at large separations, but that the problem still remains with the height-height correlation function. This topic is one of current interest in the thermodynamics of 2D systems. In the following chapter, we offer one look at the bending rigidity that may offer some insight into this problem.

Chapter 2

Graphene Mechanical Resonators

In this chapter, we study the elastic properties of graphene via the modes of graphene resonators. As discussed in the previous chapter, the elastic modulus of graphene can be measured *via* nanoindentation of suspended graphene membranes. These membranes tend to have large built-in strains, which makes the determination of the bending rigidity impossible. We begin by outlining the fabrication technique used to make low-tension membranes. We then outline a new process I developed for making large-area suspended graphene; though the resulting resonators were not used in the subsequent study, the technique may prove useful in future studies, especially in cases where one wishes to tailor the supports of the resonators or study larger area sheets. Finally, we look at the modes of our resonators. In the case of circular resonators particularly, we surmise that the modes are likely due to the bending rigidity; we also present some preliminary data on temperature-dependent frequency shifts in these devices, which may point the way to further studies of the interaction of stretching and bending modes in graphene.

The work in the chapter was done in collaboration with Dr. Benjamin Aleman, a former member of the Zettl group. Resonance studies were performed in collaboration with and in the lab of Prof. Feng Wang.

2.1 Fabrication Techniques

Direct Transfer Method

The method used to fabricate graphene mechanical resonators used in our experiment was developed by William Regan and Benjamin Aleman in the Zettl group at Berkeley.[14] The primary difference with previous methods is that no polymers are used to transfer the graphene to its supports, and neither does the graphene ever come into contact with a polymer via an exfoliation process. Also, no solvents are needed to remove PMMA; this means that that the graphene surfaces remain exceptionally clean, and that little or no tension is imparted to the membrane. We describe the method here in detail, emphasizing the points not previously

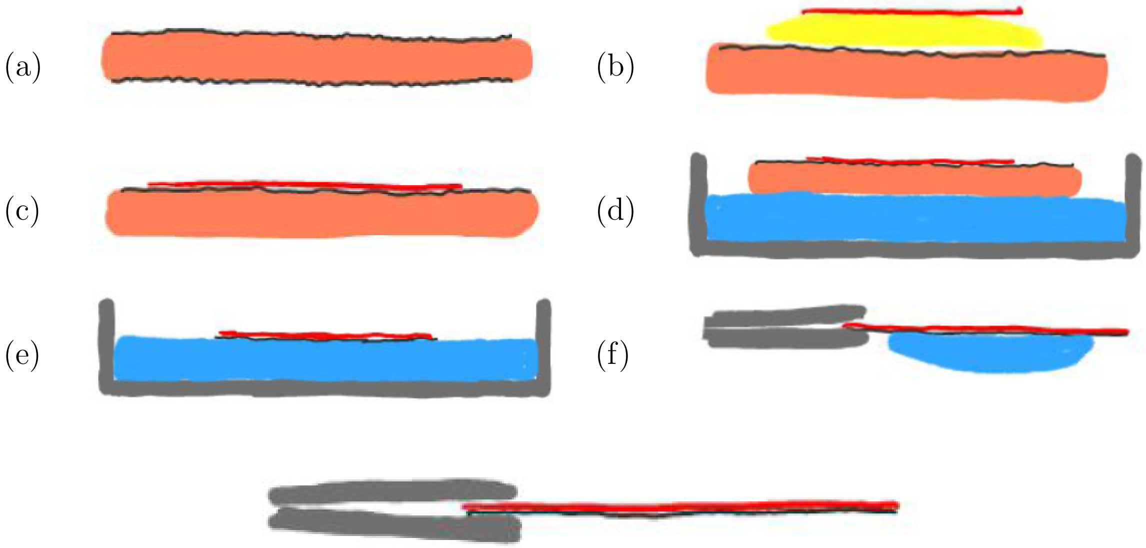

Figure 2.1: Schematic of direct transfer process for fabrication of graphene resonators. (a) graphene (black) on is grown on both sides of a copper foil (orange); (b,c) graphene on one side is removed and a a TEM grid (red) is attached with a drop of isopropanol (yellow); (d,e) copper is removed with an etchant (blue); (f) grid is rinsed and removed and allowed to dry face down

discussed which are important in describing the precise resonator structure we will study.

The method is outlined in Figure 2.1. Graphene is grown on the copper substrate at around 1000 °C in a methane atmosphere. After growth, the graphene on one side of the copper is removed via a short oxygen plasma treatment. This helps in subsequent etching of the copper, and avoids free-floating graphene in the etchant solution.

The graphene is then transferred to a TEM grid which is coated with a thin amorphous carbon layer with holes in it, referred to as “holey carbon” or by its trade name, Quantifoil. We use two types of holey carbon: one with 7 micron square holes (SPI Quantifoil S 7/2), and another with 2 micron diameter circular holes (SPI Quantifoil R 2/2). The holey carbon is about 10 nm thick, and the holes have a “lip” around 5 nm in radius. This lip is likely the result of the process used to fabricate the holey carbon, in which carbon is evaporated onto a plastic form, which is subsequently dissolved.[15, 16] Additionally, the holey carbon is very delicate, so in order to increase the yield of the resonators, the TEM grid has been previously prepared by evaporating about 100 nm of gold onto its back side. This also adds considerable mass to the supports for the graphene resonators.

We take our copper with graphene on it and cut out a small square, about 5 mm on a side, so that a 3 mm diameter TEM grid will mostly cover the surface. A small drop of isopropanol is placed on the side of the copper which still has graphene on it, and the grid is

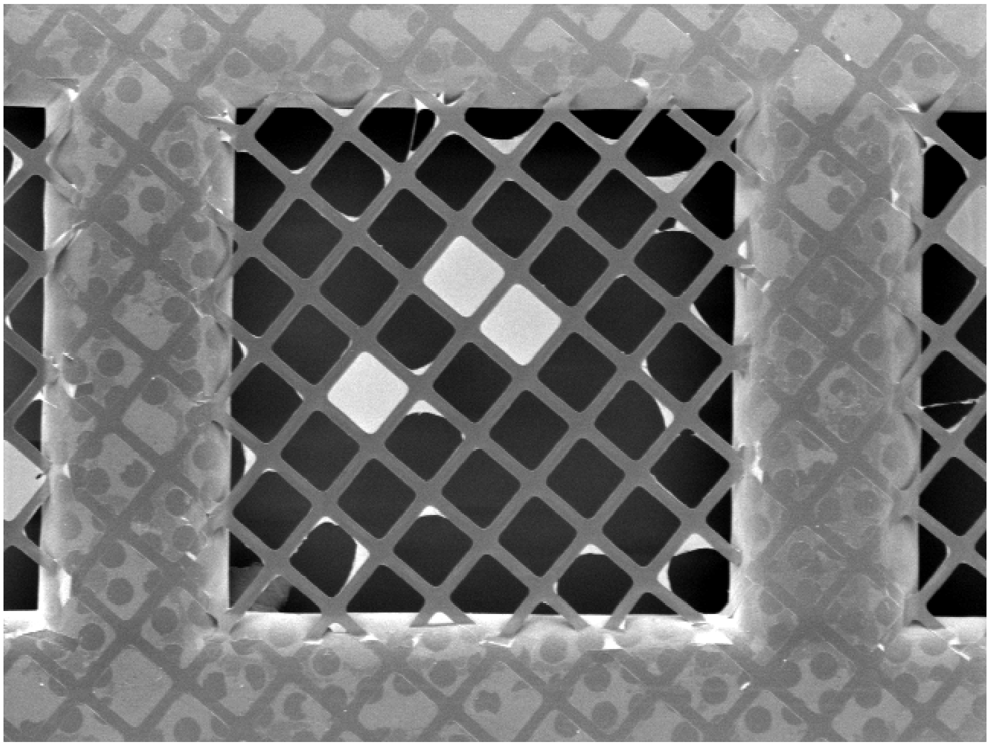

Figure 2.2: SEM image of 7 micron square graphene resonators.

placed with the holey carbon face down on top of the drop. As the isopropanol evaportates, the holey carbon is drawn down onto the surface of the graphene; graphene is very "sticky" material owing to its vertical π orbitals, and so adheres strongly to the holey carbon film. After the isopropnal has evaporated and the sample is dry, the copper square can now be picked up and shaken gently, and the TEM grid will hold on.

Next, the copper is etched away by floating it with the grid face up on the surface of an etchant solution; either iron chloride or sodium persulfate can be used here. After the copper has been completely etched, which typically takes a couple of hours, the grid is picked up with tweezers and floated on top of a bath of deionized water. Several baths can be used to make sure that the etchant solution is totally diluted. It is important in all of these steps that the grid stays on the surface of the water or etchant; dropping the grid into the bath invariably destroys the suspended graphene portions.

After proper rinsing, the grid is removed with tweezers and kept face down as the remaining drop of water dries. In the process of evaporating, the drop only sees the continuous surface of the graphene. Therefore, the film cannot be pulled down onto its supports *via* surface tension, as is the case with films that have been immersed in acetone or another solvent. Additionally, the curve of the lip of the graphene support prevents it from being pulled tight *via* van der Waals forces.

Figure 2.2 shows an SEM images of some resulting 7 micron square graphene resonators.

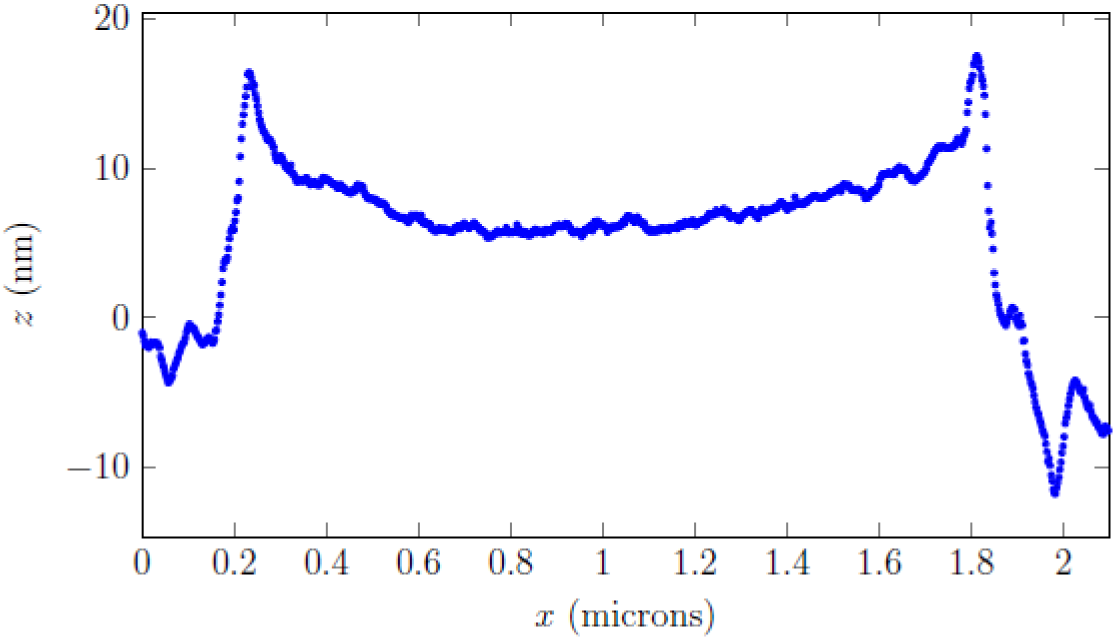

Figure 2.3: AFM height profile of a 2 micron diameter circular membrane. Data courtesy of B. Aleman.

The contrast of the graphene in the SEM can be improved by operating the SEM at 1 kV accelerating voltage. The resonators appear exceptionally clean, and the yield is acceptable for the purposes of the experiment. Prior to conducting the resonance measurements, a survey is taken of the grids in the SEM so that the location of the intact resonators can be determined; the asymmetric mark in the center of the grid is used as a reference point.

Figure 2.3 shows an AFM profile taken from a 2 micron diameter circular resonator. The graphene appears to be draped over the hole, and to be slightly buckled downward, forming a bowl with a maximum depth of about 5 nm, which corresponds to a radius of curvature of approximately 100 microns. The sharp edges on either side of the graphene are due to the lip in the holey carbon. While some of the graphene has adhered to about 5 nm of the lip, it comes off it before becoming fully tensioned. The indication is then that the graphene on the circular holes is more or less slack, with little or no tension imparted to by its supports.

Patterned PMMA Method

In the course of the experiment, it was desirable to fabricate larger area resonators, both in order to increase the amplitude of the vibrations hence increasing the signal strength, and to be able to better isolate single resonators. Commercially available TEM grids have holes only up to 5 microns in diameter, so a different approach was taken, where the holes were made in a thin PMMA layer that was later adhered to a gold TEM grid.

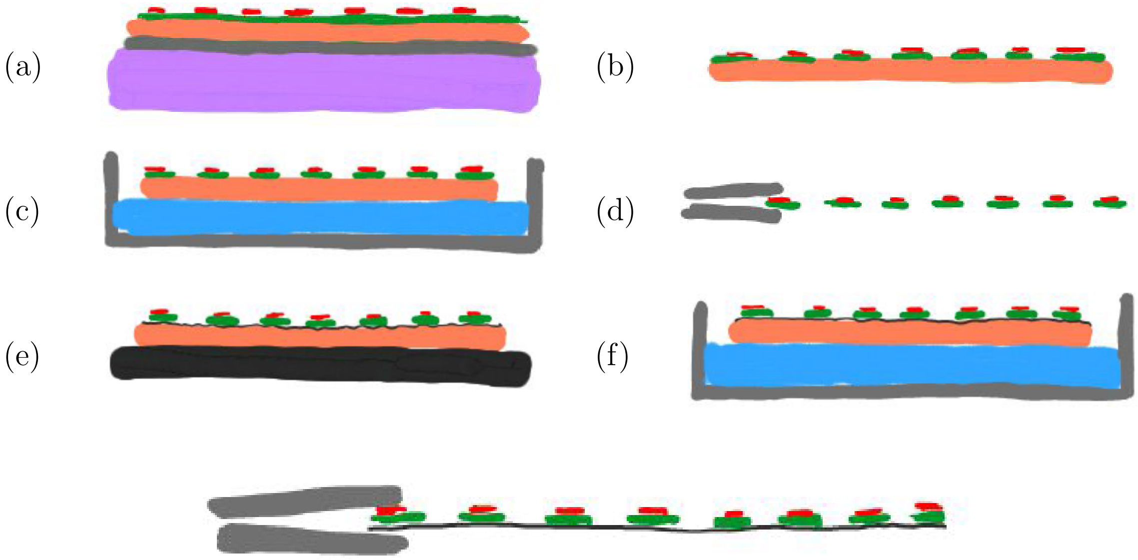

Figure 2.4: Schematic of patterned PMMA method. (a) copper foil (orange) is mounted onto a silicon chip (purple) using double-sided tape (grey); PMMA (green) is spun on and a TEM grid (red) is placed on top before drying; (b) the copper foil is removed from the chip and holes are patterned the the PMMA between the grid lines; (c,d) the copper foil is removed with an etchant (blue); (e) the grid is glued to a copper foil with graphene (black) grown on it with a hot plate (dark grey); (f) the copper is then etched, leaving the grid with the graphene attached.

The process is outlined in Figure 2.4. First a small piece of copper was first attached to a small silicon chip cut into a square about 1 cm on a side using double-sided tape. Following a recommendation by Qin Zhou, a thick layer of PMMA was then spin coated onto copper using A11 concentration with a spin rate of between 1500 and 2000 rpm. While the PMMA was still wet, the gold TEM grid was laid on top with the flat side down. The PMMA was then cured on a hot plate at 160 °C for 60 seconds, after which time the gold grid was firmly embedded.

Next, the Nano-Pattern Generation System (NPGS) in an scanning electron microscope (SEM) was programmed to pattern circles with diameters ranging from 2 microns to 32 microns. One hole was patterned in each cell of the grid. The PMMA was then developed and the copper was etched away using sodium persulfate. Figure 2.5 shows an optical micrograph of the resulting grid. The holes are well defined, although alignment of the NPGS system was problematic, so that the larger holes tended to intersect the grid supports.

The next step was to attach the grid to a copper substrate onto which graphene had been grown as discussed in the direct transfer method above. Various attempts were made at the direct transfer method, however, the surface of the PMMA was generally not flat enough so

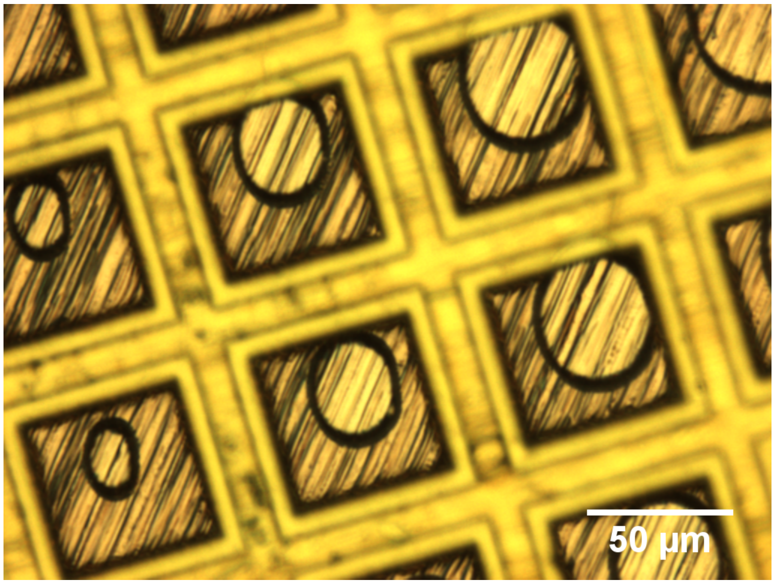

Figure 2.5: Optical micrograph of PMMA holes patterned onto a 300 mesh gold TEM grid.

that van der Waals attraction was not sufficient to keep the grid on the copper. Instead, the grid was placed on top of the copper and pressed flat between two microscope slides. The grid was then placed on a hot plate and observed with a scope. The temperature on the hot plate was set to around 160 °C and the sample watched carefully as it heated up. Once it was clear that the PMMA was beginning to melt, it was quickly removed and cooled. The grid was now firmly attached to the graphene surface. Figure 2.6 shows the grid after attaching to graphene coated copper. It can be seen that the heating process distorts the holes somewhat; this was particularly evident for thicker PMMA films. There is also a small amount of PMMA that has spilled over into some of the holes.

Finally, the copper substrate was etched using the same process as described for the direct transfer method above. After rinsing and proper drying, the holes were checked for suspended graphene. Yield was rather low, however, some of the larger holes with diameter between 20 and 40 microns were found to be spanned by suspended graphene, albeit with a good amount of contamination. The contamination actually helped to identify the graphene, as it was clear something was holding it up. The presence of monolayer graphene was confirmed using Raman spectroscopy and looking for the signature G and 2D peaks, with the absence of a D peak.

It is quite remarkable that graphene can span such large holes, even supporting polymer residues many thousands of times its own weight. Much of this is owing to its high 2D Young's modulus. It is interesting to speculate on how large graphene membranes can get. Booth *et al.* have reported intact graphene membranes up to 50 microns in diameter, slightly larger than those reported here.[1] It would be interesting to further develop and extend this technique, particularly in finding a adhesive substrate to replace PMMA which would also

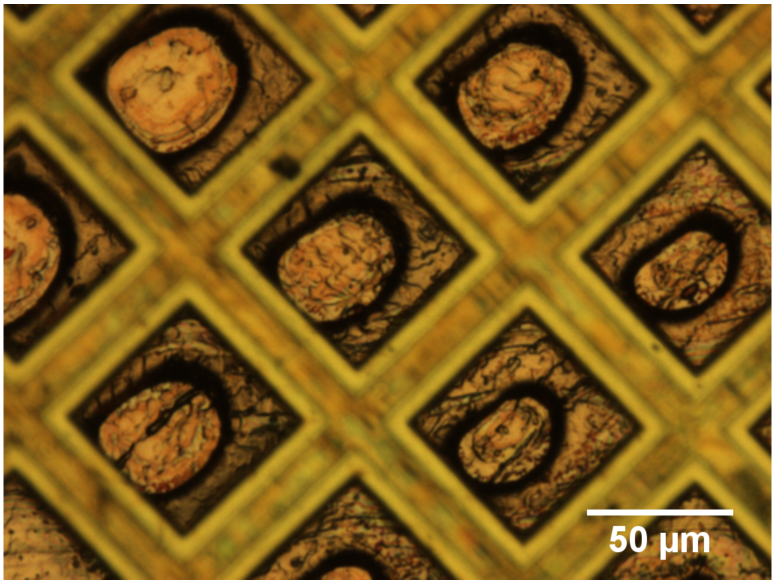

Figure 2.6: Optical micrograph of PMMA holes attached to a graphene surface.

be compatible with electron microscopy.

Unfortunately, I was not able to perform further characterization of the membranes to evaluate tension and surface morphology. This was done with membranes fabricated by Benjamin Aleman using the direct transfer method, to which we turn next.

2.2 Optical Transduction Technique

We'll first describe the optical transduction technique used to perform the resonance studies. The basic idea is to form a Fabry-Perot cavity using the graphene as one of the walls. The technique is similar to that used in previous studies of graphene resonators. [17] The Fabry-Perot cavity is formed by taping the TEM grid onto a polished silicon chip, whose surface acts as a stationary mirror. Since the reflection coefficient of graphene in the optical range is quite small, we only consider single reflections in the cavity. If the incoming light ray has intensity I_0, the reflected intensity is then to a good approximation

$$I \approx I_0 \left(T_{\mathrm{G}}^2 R_{\mathrm{Si}} + 2T_{\mathrm{G}} \sqrt{R_{\mathrm{G}} R_{\mathrm{Si}}} \cos\left(\frac{4\pi d}{\lambda}\right)\right)$$

where $R_{\mathrm{G}} \approx 1.3 \times 10^{-4}$ and $T_{\mathrm{G}} \approx 0.98$ are the reflectivity and tranmissivity of graphene [18], $R_{\mathrm{Si}} \approx 0.4$ is the reflectivity of silicon (we use a 532 nm laser, see below), d is the distance between the center of the graphene shell and the silicon, and λ is the wavelength of the probe light. If we allow the shell to vibrate according to $d(t) = d_0 + A\cos\omega t$, and assuming that

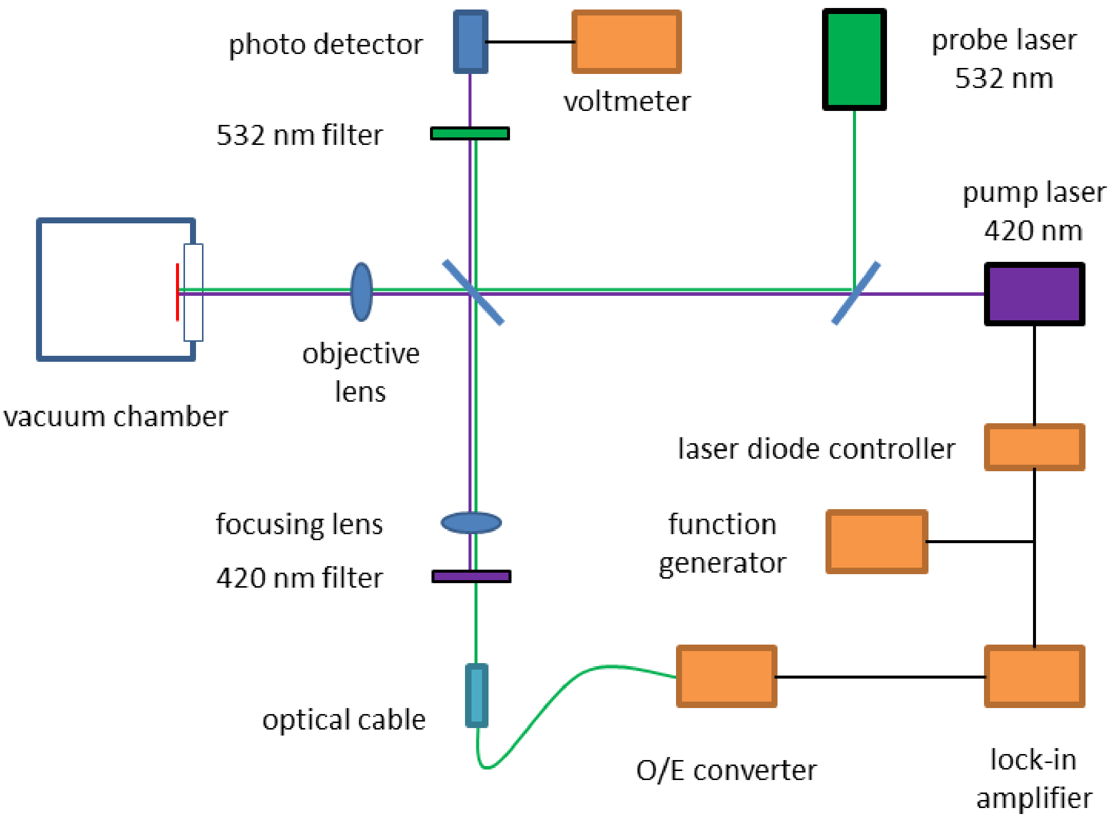

Figure 2.7: Schematic of the Fabry-Perot interferometer used to measure the spectrum of graphene mechanical resonators.

A/λ is small, plugging in relevant numbers we have to a good approximation

$$I \approx I_0 \left(0.38 + \frac{0.17A}{\lambda} \sin \left(\frac{4\pi d_o}{\lambda} \right) \cos \omega t \right)$$

The small time-dependent component of the reflected intensity can be picked up by a lock-in amplifier referenced to the driving signal. Though we cannot control d_0, we have lots of resonators to choose from and can scan them until one with a measurable signal is found.

The setup is illustrated in Figure 2.7. We'll walk through the alignment process, as it was important in getting a good signal; this involves adding each element of the setup in turn. First, the Fabry-Perot device is mounted inside of a vacuum chamber (in this case a simple cross-junction) by taping it face-out to the back side of a view port. The chamber is evacuated using a turbo-pumping station to about 1 microtorr. A green 532 nm diode laser with an output of 100 microwatts, which serves at the probe which forms the interference pattern, is reflected off an adjustable half-silvered mirror and directed onto the device after passing through a second half-silvered mirror oriented at 45 °as shown. The vacuum chamber is mounted on 3-axis stage; the light from the laser is allowed to fall on the wall of the lab and the tilt of the chamber is adjusted so that the spot reflected from the surface of the view-port overlaps with the one reflected from the sample. A second diode laser, operating at 420 nm with an adjustable output between 1 and 5 milliwatts, which will serve as the pump to actuate the resonance, is then aligned with the first using a series of adjustable mirrors (not shown). Its reflection from the second half-silvered mirror is directed towards a photodiode, which measures its power; the light from the probe laser is filtered prior to reaching the photodiode.

Next, an objective lens mounted onto a 3-axis stage is placed between the half-silvered mirror and the sample so that the sample lies at its focal point. The optic axis of the objective is adjusted until defocusing causes the laser spot to breathe in and out without shifting position. The sample can be viewed by shining a white light into the sample chamber; this was done with a retractable mirror between the two half-silvered mirrors (not shown). The image is formed by placing a focusing lens with a 15 mm focal length about 30 cm down the optic axis from the objective and is viewed with a CCD camera (not shown). The light is shone into the camera via another retractable mirror after the focusing lens (not shown) .

To measure the resonances, the end of an optical cable is placed in the image plane of the focusing lens. It was found that placing the fiber slighly to the side of the central spot improved the quality of the signal; this is likely because as the graphene fluctuates, it comes in and out of the focus of the laser. The laser light from the pump is filtered out, and the signal from the probe is fed into an optical/electrical (O/E) converter whose output is fed into the input of a lock-in amplifier. The pump laser's power is modulated by about 100 microwatts through a function generator whose output is T'ed to the reference of the lock-in amplifier. The reference frequency and output of the lock-in are read by a computer as the function generator is swept over the relevant range of frequencies, here between 500 kHz and 2 MHz.

2.3 Actuation

When the laser falls on the graphene, it of course heats it up. Assuming the power is uniform across the spot, we can solve the heat equation $-k\nabla T = \vec{q}$, where $k \approx 5000$ W/mK is the thermal conductivity of graphene [19] to yeild the temperature profile

$$T(r) = \frac{I\alpha}{kha_{\mathrm{l}}^2}\left(a^2 - r^2\right) + T_0$$

where $h = 0.35$ nm is the "thickness" of graphene, I is the intensity of the laser, α is the fine structure constant (the absorbance of graphene), a is the radius of the base of the shell, a_{l} is the radius of the laser spot, and T_0 is the temperature of the supports, assumed to be at room temperature. To simplify the discussion, we'll take the average of the temperature over the shell.

$$\Delta T = \frac{I\alpha}{2kh}\left(\frac{a}{a_l}\right)^2 \tag{2.1}$$

The increased temperature can have two effects on the resonators.

- it can cause a proportional strain in the graphene according to $\epsilon_\mathrm{T} = \alpha_\mathrm{T}\Delta T$ where α_T is the thermal expansion coefficient of graphene.
- It can cause a stiffening of the bending rigidity according to Equation 1.27.

In either case, the elastic properties of the sheet are changed. If we now allow the power of the laser to fluctuate according to $I(t) = I_0 + I_t cos\omega t$, the bending rigidity and/or stress fluctuates accordingly, and we expect that a resonance will occur when ω matches a resonance frequency of the shell. The amplitude of the vibrations increases until they loose energy at a rate consistent with the damping in the system. The phenomenon is that of *parametric resonance*, where a periodic change in the parameters of the resonator act as an effective driving force. A often-cited example is that of a child on a swing, where the effective length of the swing changes as the child lift and lowers their legs.

2.4 Spectrum of Square Graphene Resonators

We begin by looking at the spectra of the 7 micron square resonators; example of two spectra are shown in Figure 2.8. In both cases, we see a series of well-resolved Lorentzian peaks in the frequency range 400 kHz to about 1.2 MHz. We assign the lowest frequency peak to the fundamental (1,1) mode of the resonator, and work upwards. In the top spectrum, we see that the degenerate (2,1) mode is split into two peaks, indicating that some asymmetric mass and/or strain is present in that membrane. In the bottom spectrum, the (2,1) mode remains unsplit, but a number of smaller peaks are present which cannot be assigned unambiguously to the modes of the resonator; they are perhaps due to interactions with the modes of the substrate.

In the membrane model, we can determine the strain in the resonator by using Equation 1.11 and using Equation 1.6 for the stress. We have

$$\epsilon = \frac{4f^2\rho L^2}{Y(n^2+m^2)} \tag{2.2}$$

where $f = \omega/2\pi$ is the measured frequency in Hz. For the mass density ρ, we have to consider the mass of impurities as well, which can be considerable, since the mass density of graphene is small: $\rho_\mathrm{G} \approx 7.6 \times 10^{-7}$ kg/m^2. As a rough estimate, we can use TEM images by Regan and Aleman using our direct transfer process to gauge the impurity level [14] and put $\rho \approx 10^{-6}$ kg/m^2. Using this and $Y = 340$ N/m, we have based on the (1,1) mode $\epsilon \approx 10^{-6}$. 1 When considering the ratios of the mode frequencies, we see that in both cases, the higher modes are somewhat upshifted compared to the expected ratios of membrane; for example, the (2,1) mode should be $\sqrt{5/2} \approx 1.58$ times the fundamental, and the (2,2) modes should be twice the fundamental. We can account for this by considering the bending rigidity of the

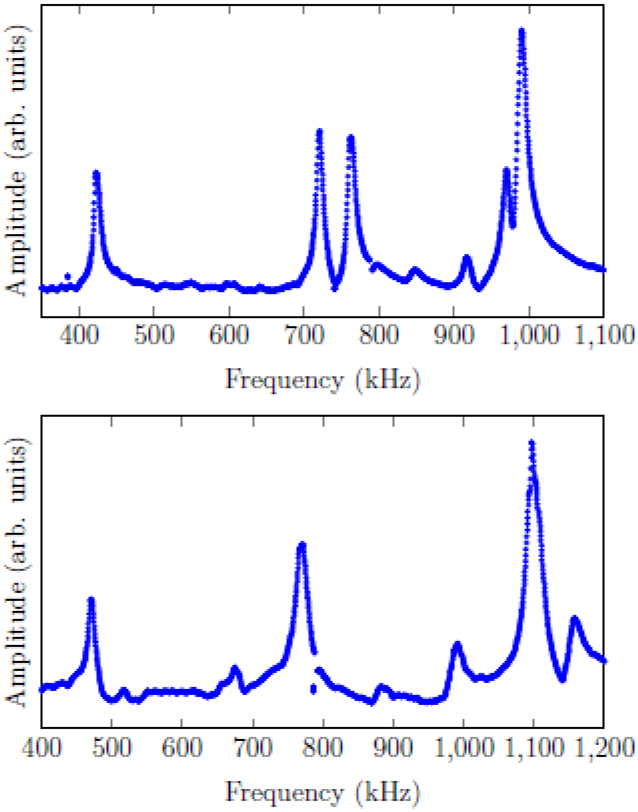

mode	f (kHz)	f/f_{11}
(1,1)	424	1.00
(2,1)	720	1.70
(1,2)	764	1.80
(2,2)	991	2.34

mode	f (kHz)	f/f_{11}
(1,1)	470	1.00
(2,1)	769	1.63
(2,2)	1099	2.33

Figure 2.8: Spectra of 7 micron square graphene resonators. The red line indicates a model fit to Lorenztians. To the right of each spectrum the mode assignment and frequencies are shown along with their ratios to the fundamental.

membrane. Using Equation 1.24, we can calculate the expected ratios of the higher modes to the fundamental; after a bit of algebra, we get

$$\left(\frac{\omega_{mn}}{\omega_{11}}\right)^2 = \frac{(n^2+m^2)\left[(n^2+m^2)^2\pi^2 h_e^2 + 12(1+\nu)L^2\epsilon\right]}{8\pi^2 h_e^2 + 24(1+\nu)L^2\epsilon} \tag{2.3}$$

where again $h_e \approx 0.1$ nm is the elastic thickness. In the denominator, the first term is negligible compared with the second (we ignore the rigidity in calculating the strain from the fundamental mode for the same reason); however in the numerator, the strong dependence on the mode numbers gives us a measurable correction. We find for example

$$\frac{\omega_{21}}{\omega_{11}} \approx 1.62, \ \frac{\omega_{22}}{\omega_{11}} \approx 2.27$$

which is in better agreement with the observed ratios, particularly for the unsplit (2,1) modes; it is possible that whatever causes the splitting of the degenerate modes may also be responsible for the increased upshift in frequency.

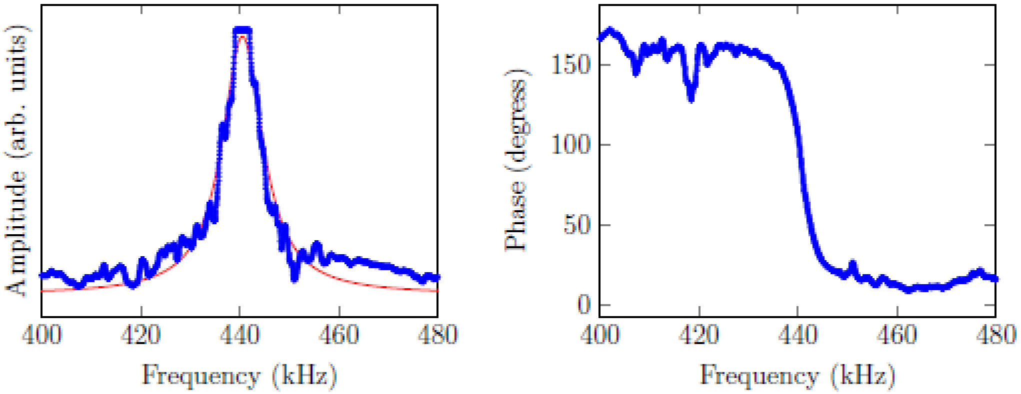

Figure 2.9: Amplitude and phase of a 7 micron square graphene resonator.

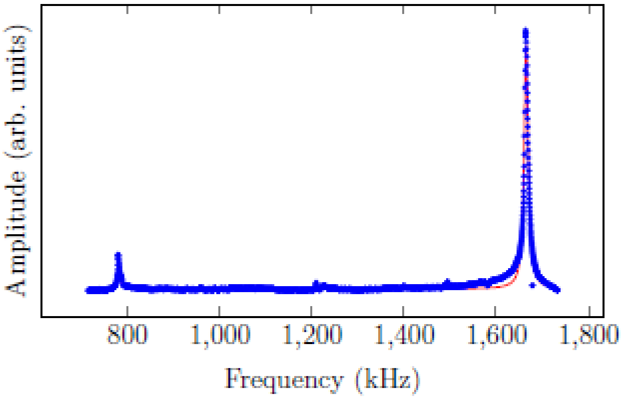

mode	f (kHz)	f/f_{01}
(0,1)	780	1.00
(1,1)	1664	2.13

Figure 2.10: Spectrum of 2 micron diameter circular membranes.

We also examine the individual peaks by scanning over them slowly. The lock-in records both quadratures of signal, so that both the amplitude and the relative phase between the response and driving signal can be determined. Figure 2.9 shows the amplitude and phase response of the fundamental mode of a 7 micron square graphene resonator. The peak is fairly well matched to a Lorentzian; the center of the peak is at approximately 440 kHz, with a full-width-at-half-maximum (FWHM) of about 10 kHz, giving a quality factor $f/\Delta f \approx 44$. The phase is seen to undergo a 180 degree shift as the driving frequency passes through the resonance, as expected for a linear oscillator.

2.5 Spectrum of Circular Graphene Resonators

Figure 2.10 shows the spectrum of a 2 micron diameter circular resonator. Two peaks are clearly resolved, which we assign to the (0,1) and (1,1) modes, respectively. If we treat the

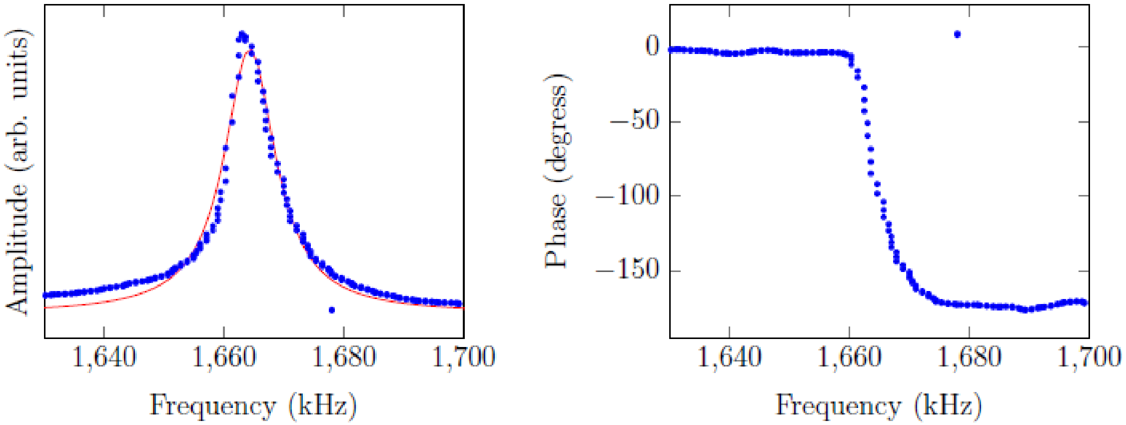

Figure 2.11: Amplitude and phase response of a 2 micron circular graphene resonator.

resonator as a membrane, using the values in Table 1.1 we arrive at strain of $\epsilon \approx 10^{-10}$, which is a very small number. Also, the ratios of the fundamental to the (1,1) mode do not match up with those of a membrane. On the other hand, if we treat the resonator as a clamped sheet with a finite bending rigidity, we have for the fundamental mode, from Table 1.2

$$f_{01} = \frac{1.624}{a^2}\sqrt{\frac{\kappa}{\rho}} \approx 796 \text{ kHz}$$

which comes very close to the measured value of the resonator; the discrepancy may have to do with our approximation of the mass density. Moreover the ratio of the fundamental to the first harmonic comes very close to the expected value, again from Table 1.2, of 2.08.

In general, the peaks measured from the circular resonators tended to be sharper and more well-defined than those from the square resonators. Figure 2.11 shows the amplitude and phase of the higher harmonic in Figure 2.10. The peak is much narrower, with a FWHM of about 6.2 kHz, yield a quality factor of about 270, which is a great improvement over that of the square membranes. The phase likewise shows a clear 180 degree phase shift as the driving frequency is swept through the resonance, again indicating a good linear response.

2.6 Intensity-Dependent Frequency Shifts

As mentioned above, the mean power level of the pump laser could be varied between 0 and 5 milliwatts. We investigated the dependence of the spectra on the mean power, and found that significant frequency shifts would occur. Figure 2.12 shows a series of spectra taken at various power levels. The intensity has been normalized to that of the spectrum shown in Figure 2.10. Both the fundamental mode and the higher harmonic shifted in proportion to one another, maintaining their relative frequencies to within a few percent. The shift was quite dramatic; at a relative intensity of about 100, the frequencies were both about

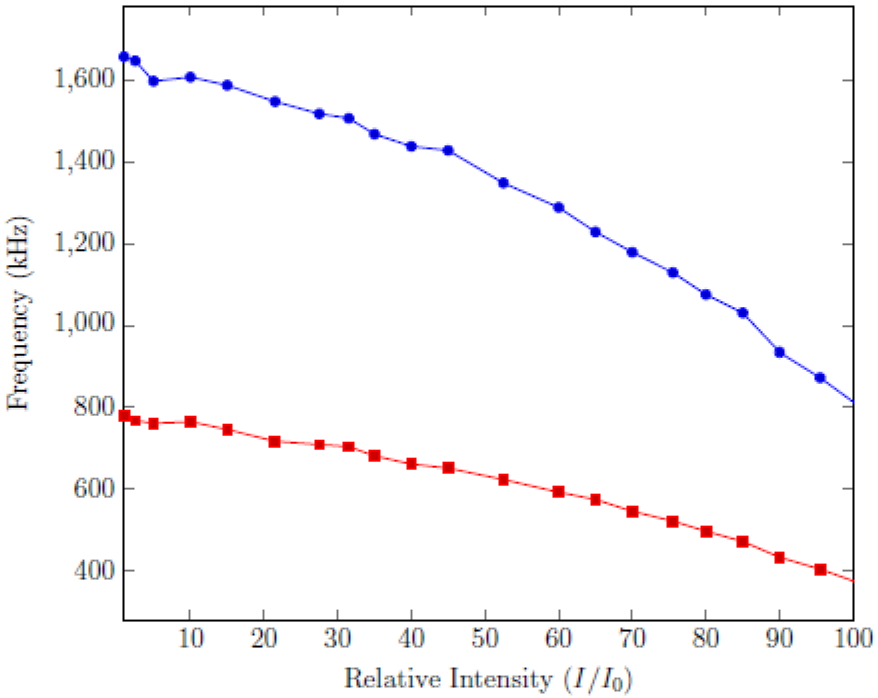

Figure 2.12: Intensity-dependent resonance frequencies of a circular graphene resonator. The red line shows the center frequency of the fundamental mode; the blue line shows that of the (1,1) mode.

half of their initial value. The shifts themselves are approximately quadratic in the relative intensity.

Another interesting feature of the shifts was the change in the quality factor of the peaks. As the peaks shifted, their amplitude and widths also changed accordingly. The dependence of the quality factor on the relative intensity is shown in Figure 2.13. At low relative intensities, the quality factors tended to be quite high and would vary significantly. At a relative intensity of about 45 and above they were uniformly around 50, or about the same as those of the square membranes.

It is admittedly hard to make sense of this data. The increased intensity of course heats up the resonators, so the effects are most likely a result of increased temperature. One possibility is that there is some small amount built-in strain in the resonators which is released as the temperature increases. This would imply that the thermal expansion coefficient of the graphene is positive in this temperature range; while some studies has pointed to this possibility, the evidence in the literature is far from conclusive. [13, 20] Lastly, the behavior of the quality factor may indicate some kind of interaction between the stretching and bending modes; it is possible that as the strain and/or bending rigidity change with temperature, that coupling between these modes leads to changes in the loss

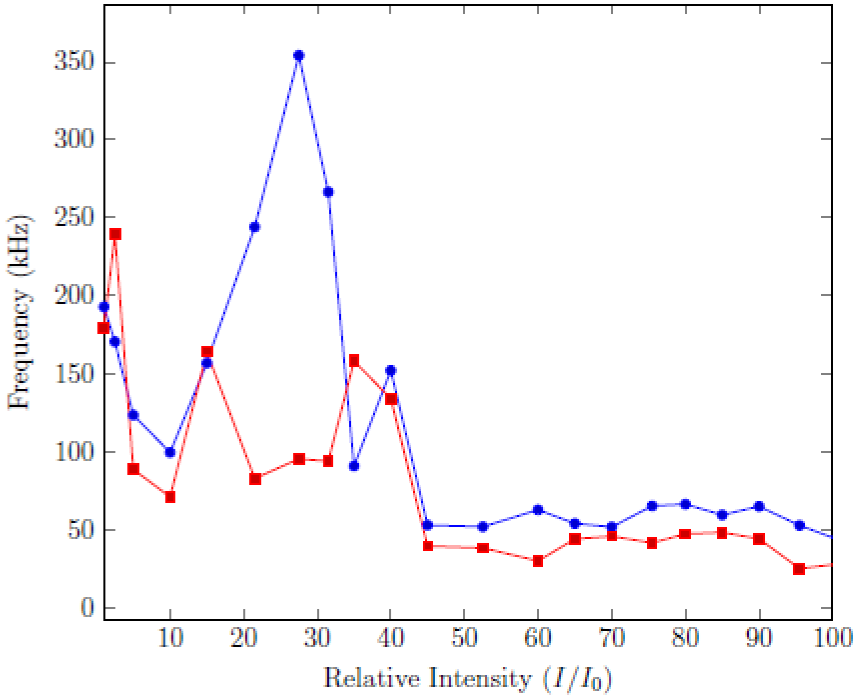

Figure 2.13: Intensity-dependent quality factors of a circular graphene resonator. The red line shows the quality factor of the fundamental mode; the blue line shows that of the (1,1) mode.

mechanisms for the resonators.

Chapter 3

Ultrathin Nanotube Sheets

Graphene is not the only ultrathin material we can make from sp^2 bonded carbon. In this brief chapter, we describe the fabrication of ultrathin nanotube sheets, some observations of the their behavior in solvents, and some experiments conducted on Joule heating.

3.1 Fabrication

The fabrication technique I used was inspired by that of Wu and Chen. [21] Nanotubes are first dispersed in a solution of 1% by weight sodium dodecyl sulfate (SDS), a common surfactant used to suspend nanotubes in aqueous solutions. The type of nanotube was also important; it was found that nanotube that had a macroscopic "fluffy" character, like HiPCo single-walled tubes or NanotechLabs multi-walled tubes, tended to make much better films as well; "sooty" materials like CoMoCat tubes tended to do very poorly. Low concentrations, of a few mg/L, were generally used, resulting in a solution with a greyish tint. I avoided ultrasonication as much as possible, as this tended to break the tubes us up and result in lower strength film. The solution was instead heated to around 60 °C and stirred for a several days, with brief sonication intervals of about 30 seconds every few hours to break up large chunks.

Prior to fabricating the films, the solutions were allowed to settle for a few hours so that larger chunks would precipitate out. A few milliliters of the solution was then pulled through a vacuum-filtration system and the nanotubes were collected on a 25 mm diameter cellulose filter. It was important to pull the solution through slowly, making sure that it was more or less still throughout the process; a rate of about 0.5 mL/second was ideal.

After the solution was pulled through, the filter was checked visually to gauge the thickness of the film. Thicker films tended to be a dark grey in appearance, while the thinnest film were barely visible against the white background of the filter. Copious amounts of water were then pulled through the film, again slowly to avoid disturbing the nanotubes, until it was evident that most of the excess surfactant had been washed away. The filter was then removed, and a small square, usually around 5 mm on a side, was cut out with a razor blade.

To separate the film from the filter, a modification to Wu and Chen's process was developed. A small splash of acetone was added to a petri dish and swirled around to just wet the bottom of the dish. The filter paper was placed with the nanotubes facing up on the wet surface until it just started to dissolve. A few more milliliters of acetone was added and swirled vigorously until the film started to peel off. This takes some practice to get right. I found the process to be easiest when the film was removed while the filter was still wet with water from the filtration process. When then the film comes off, the dish was tilted, moving the film to one side, and the half-dissolved filter paper was wiped up with a tissue.

Next, the petri dish was filled with acetone and covered, and the film was allowed to float in the solvent for about one hour. Afterwards, the acetone was exchanged, and the process repeated two to three times. Getting rid of most of the remaining cellulose on the filter is important; for ultra-clean film, more exchanges with acetone are desirable.

Crumpling

As the films, especially the thinnest ones, floated in the acetone, they underwent an interesting Browning-like motion. The films would fluctuate and fold on themselves occasionally, and would unfold under slight agitation. In one set of informal experiments, I tried changing out the solvent to chloroform, and noticed that the film would flatten out considerably; exchange to isopropanol would make the film crumple up. This is likely due to the varying polarity of the solvents. Cholorform has relative polarity (to water) of 0.259, while those of acetone and isopropanol are 0.355 abd 0.546m respectively. [22] As the polarity decreases, it appears the the film becomes less crumpled; carbon nanotubes are nonpolar, so this crumpling may be an effect of the film wanting to decrease its surface area to avoid the polar solvent. It would be interesting to check this behavior against film thickness as well as the temperature of the solvent; it may be possible to observe a crumpling transition, as in the theory of liquid membranes. [23] Here again, the interplay between the bending rigidity and surface stress on the film comes into play.

3.2 Suspended Films

After being properly cleaned in solvents the films could be picked up onto apertures, resulting in suspended nanotube films. I used a variety of apertures, though most precise and easiest to work with were TEM aperture grids with holes ranging from 50 to 1000 microns (SPI). Getting the film to lay flat across the apertures was tricky; I usually had to chase the film around as it floated in the solvent for some time, and tease it with the end of my tweezers to make it lay flat. The advantage of using TEM aperture grids was that the films could be observed in the TEM.

Representative images are shown in Figure 3.1. At low magnification, we see that the film has a good amount of residue; the film however is strong enough to support residues that appear to be much thicker than the nanotubes themselves. Moreover, the tubes appear

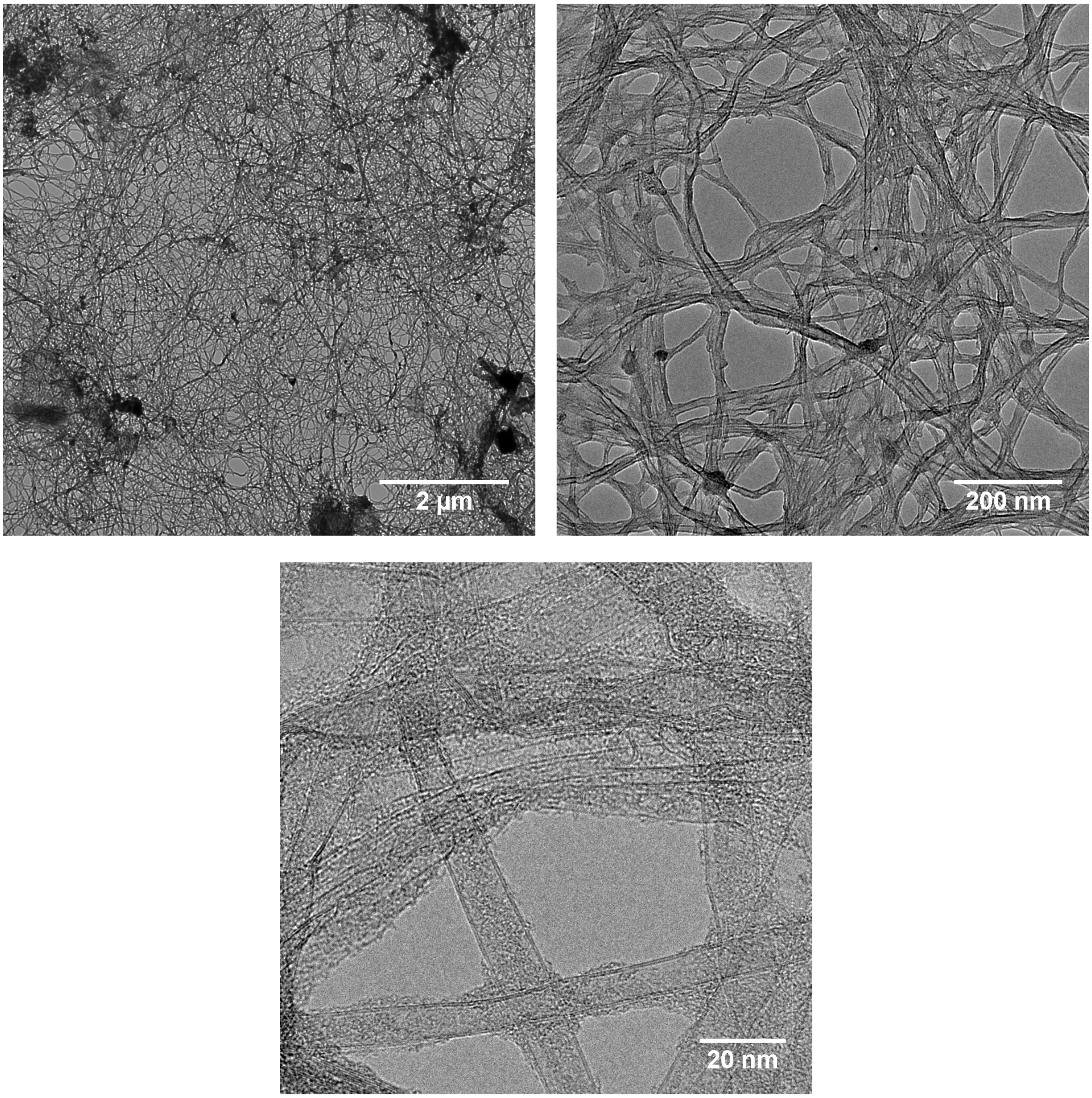

Figure 3.1: TEM images of a suspended carbon nanotube film.

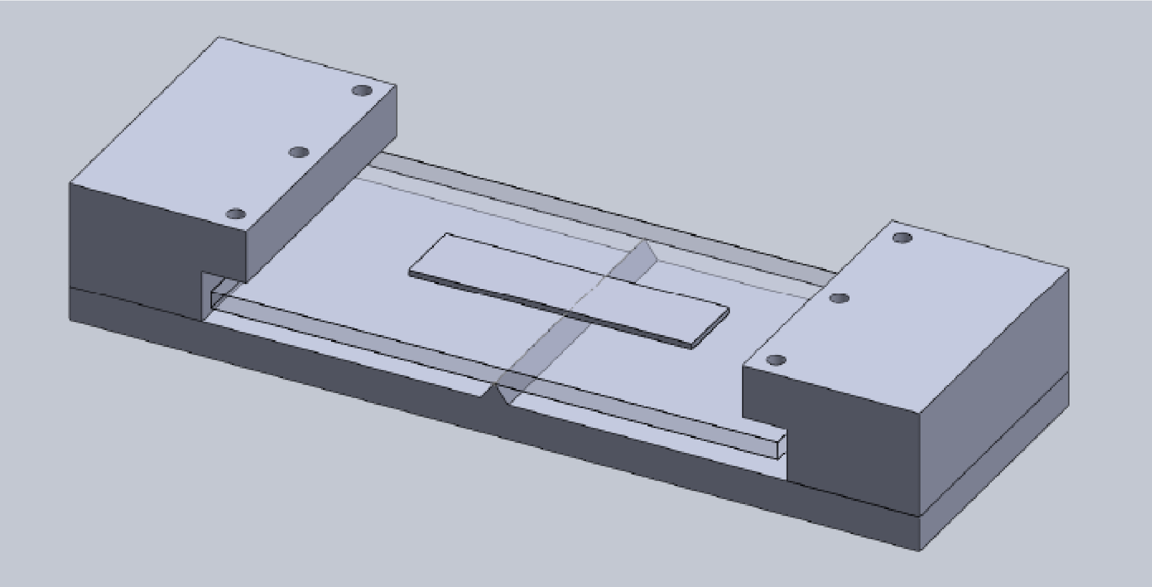

Figure 3.2: CAD drawing of device used to make adjustable trenches in silicon.

to be rather well dispersed and uniform. At higher magnifications we see that the tubes have largely been unbundled and form a disperse network. Residue can also be seen on the surface of the nanotubes. This is likely residual SDS, which even with thorough rinsing is difficult to remove completely.

3.3 Films Suspended over Adjustable Trenches

In another set of trials, I was able to suspend the films over trenches with an adjustable width, formed by a crack in a silicon wafer. Electronic-grade silicon tends to cleave along very straight lines and is easy to work with; the suggestion to use silicon to make precise trenches was given to me by Dr. Jannik Meyer. To make precise cracks, I began by gluing 5 mm wide by 2 cm long silicon strips to the center of a glass slide. Before gluing, the back side of a the silicon was scratched with a diamond scribe near its center. The slide was then mounted into a custom-built "cracker" device that I made in the machine shop. It is similar in design to devices used to make break junctions.

A CAD drawing of the device is shown in Figure 3.2. The glass slide is balanced on a fulcrum made from two round-headed screws (shown as a wedge in the drawing). Torque is applied to either end of the glass slide *via* #1 screws (72 turns per inch) that are inserted into the threaded holes shown on the supports. For the initial crack, the slide was flipped over so that the silicon chip was between the two fulcrum screws, and the end screws were slowly tightened until a faint "click" could be heard; this was the result of a hairline fracture in the silicon. The slide was then flipped over, and the crack observed in an optical microscope.

With the right finesse, cracks with an equilibrium width as small as 1 micron with fairly parallel edges could be produced in this manner. The width of the crack could then be adjusted by tightening the screws on the supports.

To make suspended nanotube devices, a film of nanotubes was first made as described above and picked up onto the silicon strip before it was mounted onto the glass slide. If one is very careful, the crack could be produced in such a way that the nanotubes span the resulting trench. Such a device could be used, for example, to study the effect of strain on the nanotubes. It may also be possible to suspended graphene or few-layer boron nitride in this manner, which would open the possibility of studying strain effects on these material as well. Lastly, per a suggestion by Prof. Zettl, the slide could be replaced with a bimorph, which is a bilayer piezoelectric device which bends upon an applied voltage. This would allow for finer control of the trench width, and also allow for remote operation inside of an SEM. Lastly, adding an insulating layer between the silicon and tubes would allow for controlled transport measurements of the suspended material.

3.4 Joule Heating of Nanotube Films

In another experiment, I looked at Joule heating of nanotube films. In this experiment, I fabricated thicker films which I suspended over tungsten wires, like the filament of a lightbulb. The films were cleaned in solvent and then inserted into a a quartz tube which was evacuated with a turbo pump to about 40 microtorr. An DC voltage between 0 and 20 volts was applied; the tungsten wires were about 1 cm apart, and the film was about 1 cm wide. Typical resistance was around 60 Ω. As more and more current was run through the device, the filament would eventually light up and the temperature could be measured with an optical pyrometer.

Pure carbon films would typically survive up to around 1000 °C, after which they would burn up. The power *vs.* T^4 for a single-walled carbon nanotube film is shown in Figure 3.3. The material follows closely the Stephan-Bolzmann law, with as associated effective area of 0.16 cm^2, assuming an emissivity of 1. The resistance *vs.* temperature of the film is shown in Figure 3.4. Interestingly, the resistance declines roughly linearly with the temperature.

A film was also made with an even mixture of carbon and boron nitride nanotubes. The power *vs.* T^4 is shown in Figure 3.5. The material follows closely the Stephan-Bolzmann law, with as associated effective area of 0.29 cm^2, assuming an emissivity of 1. The resistance vs. temperature is more interesting, showing an exponential-like decline with increasing temperature which appear to approach the value of 35 Ω in the limit of high temperature.

The temperature vs. resistance behavior of the films is suggestive of semiconducting behavior, where carriers are promoted across a band gap *via* thermal excitation. The expected behavior of the resistance is in that case

$$R(T) = R_a e^{E_g/2k_B T} \tag{3.1}$$

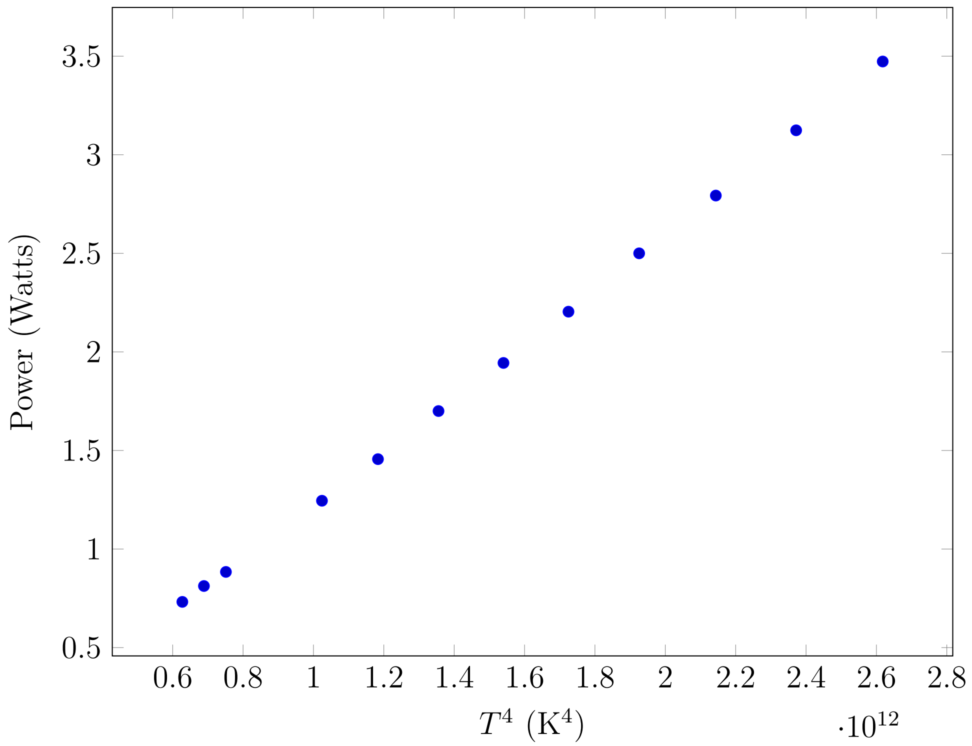

Figure 3.3: Power *vs.* T^4 for a single-walled carbon nanotube film.

where E_g is the band gap. In Figure 3.7 we plot the resistance vs. the inverse temperature on a semilog axis, where the residual resistance of 35 Ω evident in Figure 3.6 has been subtracted off. We see that there are two linear trend lines, one in the lower temperature range which corresponds to a bandgap of 0.52 eV, and another in the higher temperature range corresponding to a gap of 2.07 eV.

One comment we should make is that this data was taken only in one direction, as we film was being heated. It is possible that some effects are due to annealing of the sample, and that repeated sweeps may give different results. More well-defined geometries would also be helpful, as would a clear determination of contact resistance. Further studies of this interesting behavior may help clarify these issues. It is rare that semiconductors are studied in this temperature range.

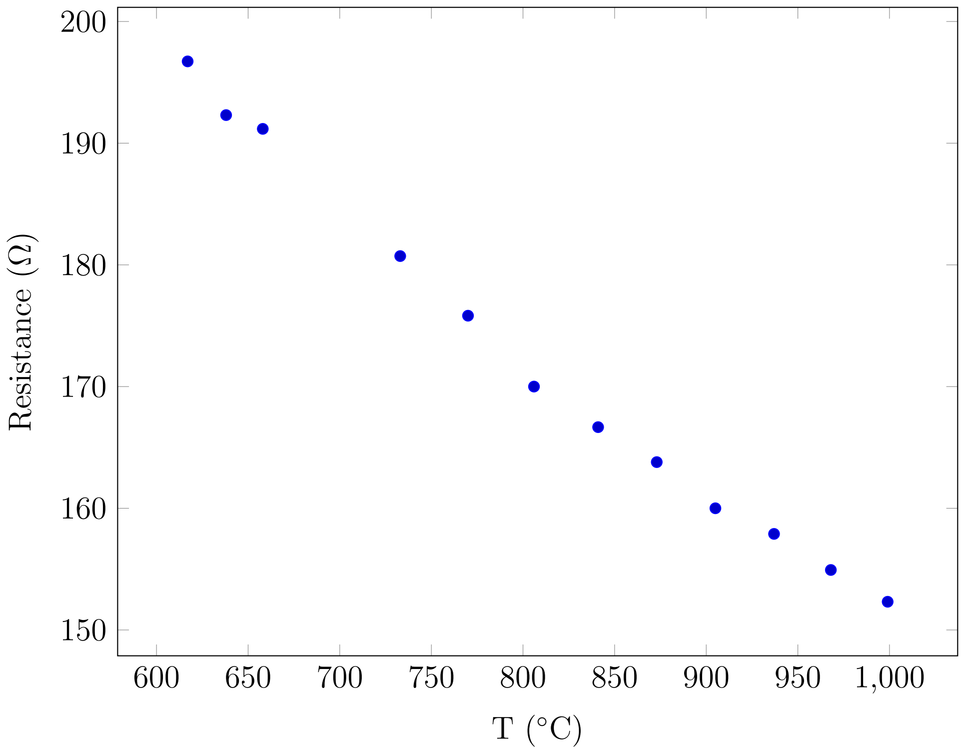

Figure 3.4: Resistance *vs.* temperature for single-walled carbon nanotube film.

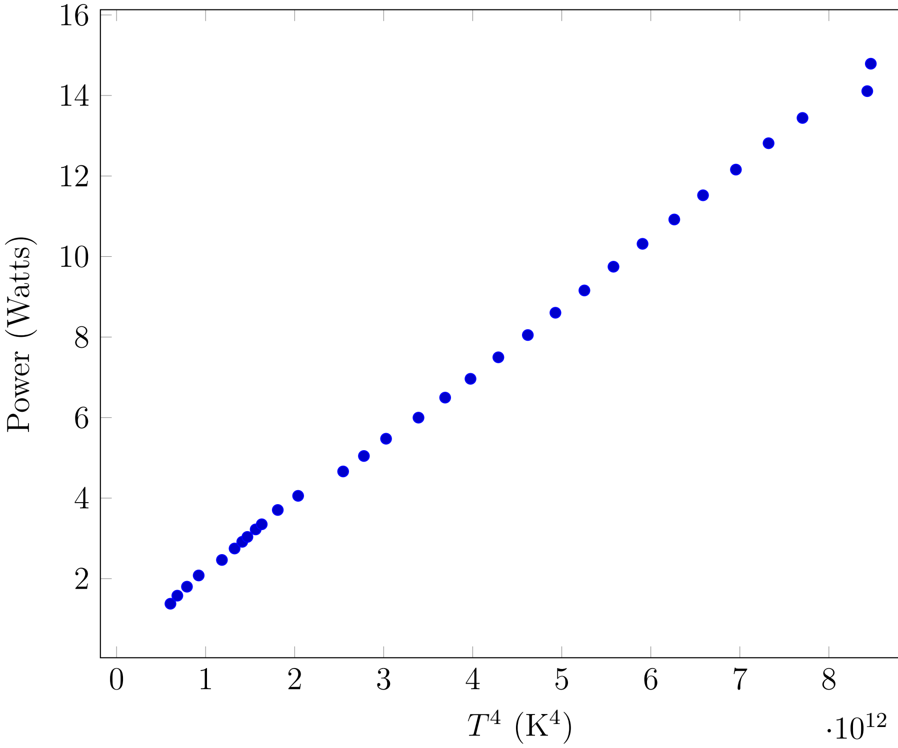

Figure 3.5: Power *vs.* T^4 for a single-walled carbon-BN composite nanotube film.

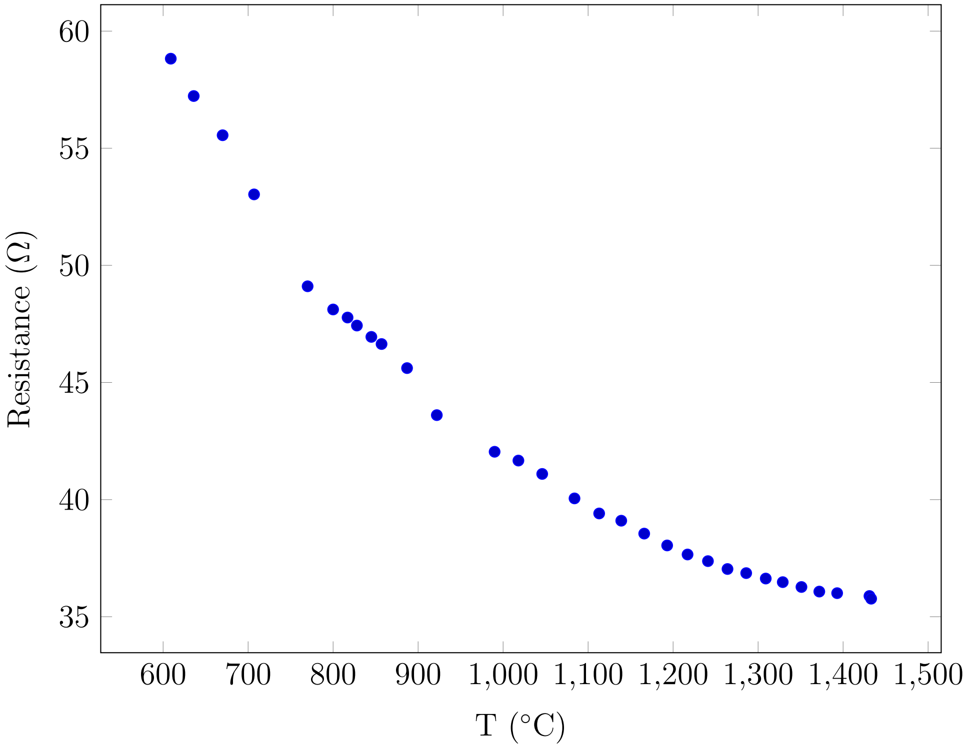

Figure 3.6: Resistance *vs.* temperature for a single-walled carbon-BN composite nanotube film.

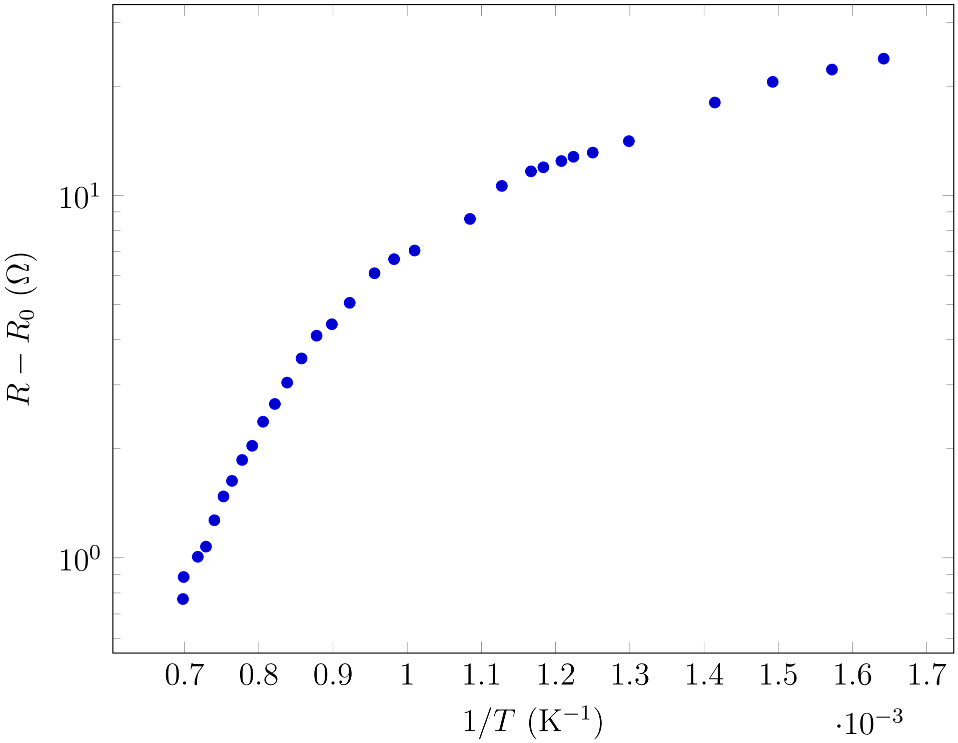

Figure 3.7: Resistance *vs.* inverse temperature for a single-walled carbon-BN composite nanotube film.

Chapter 4

Graphene and Boron Nitride Aerogels

In this chapter, we look at porous 3D macroassemblies of graphene and boron nitride. Macroassembiles of nanoscopic materials can be useful in practical applications; porous carbon-based materials particularly are widely used in industry in applications such as filtration systems and are finding increasing use in products such as supercapacitors and other alternative energy technologies.[24, 25, 26, 27, 28] More recently, BN-based analogs of these materials have been studied; owing to its increased oxidation resistance, BN can be useful in applications such as catalysis and hydrocarbon cleanup, and the polar nature of the BN bond, which changes the surface properties and can lead to enhanced gas adsorption properties.[29, 30, 31]

The general term for a 3-dimensional, cross-linked network of elements is a *gel*. The cross-linking can be through covalent bonds, or through weaker interactions such as hydrogen bonds or van der Waals attraction. The process of creating the cross-links is called *gelation*. The most familiar gels, such as those used to style hair, are made of polymers; they are termed *hydrogels* since the space in between the polymers is filled with water.

Aerogels are gels that have air or some gas in between the elements; typically they contain upwards of 90% gas by volume. For this reason, densities tend to be very low, usually a few mg/cm^3. They are also meso- or nano-porous, with specific surface areas (SSA) typically several hundred m^2/g. Aerogels are commonly made by first forming a hydrogel and subsequently removing the water. Freeze drying or critical point drying in CO_2 is most often necessary in order to avoid collapse of the nano- and meso-pores *via* surface tension forces.

The most common aerogels are made of silica and are often used as insulation on account of their very low thermal conductivity. Carbon-based aerogels are new by comparison, but also fall under the class of porous carbons, which have a long history of application dating back to the Egyptians. Activated charcoal is traditionally used as a filter and an absorbent owing to is high specific surface area (SSA), low cost and high availability. Assuming adsorption of both sides of its basal plane, graphene has a theoretical SSA of 2,600 m^2/g. On the other hand, graphitizing carbon precursors, when used in traditional synthesis processes for porous carbons, almost always result in predominately macroporous materials with very

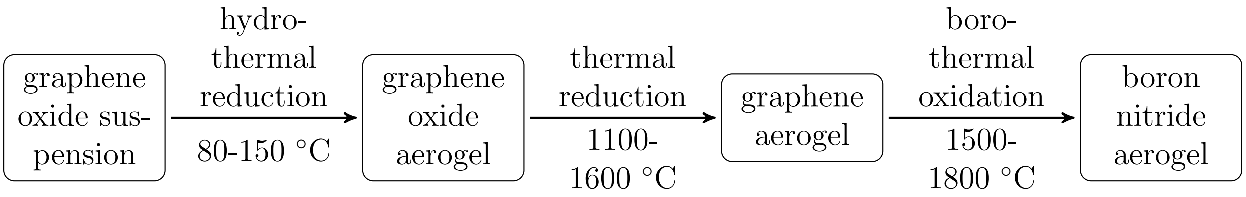

Figure 4.1: Schematic of the relationship between graphene oxide, graphene, and boron nitride aerogels.

low SSA, making them much less useful. By taking a bottom-up approach, aerogels made from carbon nanotubes and graphene may thus offer distinct advantages.

In a parallel vein, porous forms of boron nitride have attracted attention, particularly in the field of hydrogen storage. As discussed in the introduction, the difference in electronegativity between boron and nitrogen confers to the surface of BN electrical dipole fields, which in turn can induce dipoles in adsorbant molecules, leading to an increase in binding energy. While results remain inconclusive, some studies have indicated an improvement in hydrogen storage capability over carbon based materials.[32, 33, 34, 35, 36, 37] Its excellent thermal properties may also make porous BN a good ultra-high temperature thermal and electrical insulator. High chemical inertness coupled with its thermal stability also makes porous BN an excellent candidate for catalyst support.[38]

In the present chapter, I describe and analyze a set of experiments on aerogels composed of atomically thin reduced graphene oxide, graphene, and boron nitride sheets. These differ from typical aerogels in that the basic elements are 2D instead of 1D linear molecules; for this reason, they exhibit unique surface morphologies and cross-linking structures, which we will analyze using transmission electron microscopy (TEM).

The gels are related to one another through chemical processes of reduction and oxidation, shown schematically in Figure 4.1: hydrothermal reduction is used to convert a graphene oxide suspension to a reduced graphene oxide hydrogel, which is then super-critically dried to form an aerogel; high temperature thermal reduction is used to convert the resulting aerogel to a graphene aerogel; and carbothermal reduction of boron oxide – or alternately, boro-thermal oxidation of graphene – followed by nitridation is used to convert the graphene aerogel to boron nitride.

The work in this chapter was done in collaboration with Anna Goldstein and Dr. William Mickelson at UC Berkeley's Center of Intergrated Nanomechanical Systems, and with Drs. Marcus Worsley and Leta Woo at Lawrence Livermore National Laboratory. Dr. Worsley provided many of the original graphene aerogel samples. Dr. Mickelson performed much of initial TEM work, as well as the EELS measurements. Ms. Goldstein worked closely with me throughout the project, providing samples, conducting TEM investigations and porosimetry measurements, and providing much useful insight.

4.1 Graphene oxide and reduced graphene oxide aerogels

Graphene is a relatively inert material owing to its planar structure and tight sp^2 bonds; however, the possibility of sp^3 hybridization of all or part of the graphene surface does allow it to be functionalized. Graphene oxide (GO) refers to a class of materials where graphite has been subjected to strong oxidizers, resulting in hydrophillic, oxygen containing functional groups covalently bound to the surface and edges of graphene's hexagonal lattice . It was first synthesized in 1840 by Schafhaeutl in the process of combining various minerals with acids, in this case Kish graphite flakes with sulfuric and nitric acids.[39] The predominate commercial process used today was first reported by Hummers and Offeman in 1958 and results in a yellowish-brown, foam like substance.[40] Dreyer and Park offer an recent review of graphene oxide chemistry.[41]

Structure of Graphene Oxide

The atomic level structure of GO has been the subject of a number of recent studies and remained controversial for some time. The currently accepted model which has found considerable experimental support was first proposed by Lerf and Klinowski in 1998.[42] On the basis of nuclear magnetic resonance (NMR) studies and other data, they concluded that GO contains separated regions of aromatic carbon and oxidized regions containing a combination of sp^3-bound hydrodyl groups and epoxides, which form a layer of oxygen atoms above and below a 2D honeycomb layer. The structure is essentially nonstoichiometric, with random domains of oxides interspersed throughout a sp^2-bound graphitic backbone. Carboxyl groups are believed to attach primarily to the edges of the graphene oxide flakes, a conclusion which was recently supported in a study by De Jesus [43]. Aberration-corrected TEM studies by Pantelic [44] and Erickson [45] have provided atomic-scale imaging of the segregation of aromatic and oxidized regions. A recent study by S. Zhou suggest a simple kinetic model, wherein the oxygen functionalities diffuse on the surface of the graphene lattice and agglomerate by means of weak attractive potentials. [46]

The introduction of sp^3 bonds into the basal plane of graphene leads to increased wrinkling of the GO sheets. AFM studies of GO on HOPG by Pandey indicate that the surface has a roughness of approximately 1.1 nm and is dotted with 0.2 - 0.4 nm protrusions as well as "meandering wrinkles" that appear as ridges up to 10 nm in height. [47]. In the case of epoxy groups, Li has argued that conformational changes in the graphene sheet lead to large strains which can be relaxed by forming linear oxidized structures. [48] Some evidence for these can be found in both Pantelic and Erickson's studies; the latter also indicated that strain tended to be concentrated at the boundary of the aromatic regions. Upon thermal reduction, these epoxide chains may leave behind defects which "iron in" the wrinkles.

It is interesting to note that in all of the above studies, the GO sheets are tied to a surface, either a flat substrate or holes in a carbon film used in TEM imaging. This inevitably flattens the GO sheet with respect to its free-floating form; hence larger-range curvature is possible in fully suspended sheets. An interesting recent study by Whitby indicates that it is energetically favorable for single-layer GO to bend back on itself, particularly in high pH environments. [49]. Their simulation suggest that the bending rigidity is lower in GO than in pure graphene, owing mostly to the defects and functional groups on its surface. This is the opposite of what occurs in most 3D metals, where increased dislocations and defects tend to lead to increased stiffness. One also sees this is macroscopic 2D system, such a piece of paper, which increases its bending rigidity upon crumpling.

Gelation through hydrothermal reduction

While the structural modifications in GO compromise some of the outstanding features of graphite, such as mechanical strength and electrical conductivity, they confer a great advantage in materials processing as it is trivial to make well-dispersed suspensions of the material. The polar nature of these functional groups means that GO becomes hydrophillic, and when dispersed in water, acquired a negative surface charge. Suspended GO flakes tend to exfoliate into atomically thin sheets when lightly sonicated, leading researchers to consider it early on as a precursor to forming monolayer graphene. The role of water in GO's structure was considered by Lerf and Klinowski, who concluded that it formed an integral part of the GO structure, and were strongly bound to the epoxide and hydroxide groups; it began to decouple from fully hydrated GO at 160 to 220 °C. [42]

The chemical reduction of GO in solution was explored early on by Stankovich *et al.* through the use of hydrazine, usually resulting in a black powder which, upon losing a large fraction of its oxygen functional groups, would precipitate to the bottom of the containing vial. [50] Hydrazine, however, is highly toxic, making this approach problematic. In 2009, Y. Zhou *et al.* reported on a "green", hydrothermal process using only water. In their experiment, aqueous GO solutions of 0.5 mg/mL were placed in a Teflon-lined autoclave and heated to 180 °C for 6 hours. The solution turned visibly black and opaque from light brown, indicating a change in optical conductivity, likely due to increased π-conjugation. XPS spectra indicated an increase in the C/O ratio, from 1.8 to 5.6. A shift in the relative intensity of Raman peaks also indicated an increase in graphene-like, sp^2 bonding.

This technique of hydrothermal reduction was subsequently employed by Xu *et al.* to produce monolithic rGO aerogels. [51] By simply increasing the initial concentration of GO to around 2 mg/mL, they found that the recovery of aromatic structures in the constituent sheets was accompanied by π-stacking between them, leading to cross-linking and hence gelation. The process is illustrated in Figure 4.2. The initial structure is analogous to several crumpled sheets of paper laying next to one another. Initial contact between the sheets occurs at the areas of largest curvature, which correspond to the highly oxidized regions of GO. The long-range interaction between the sheets may be facilitated by hydrogen bonding. [49] As the sheets begin to lose functional groups, short-range van der Waals interactions can cause the sheets to coalesce and fold together, forming a cross-linked 3D structure which precipitates from the solution.

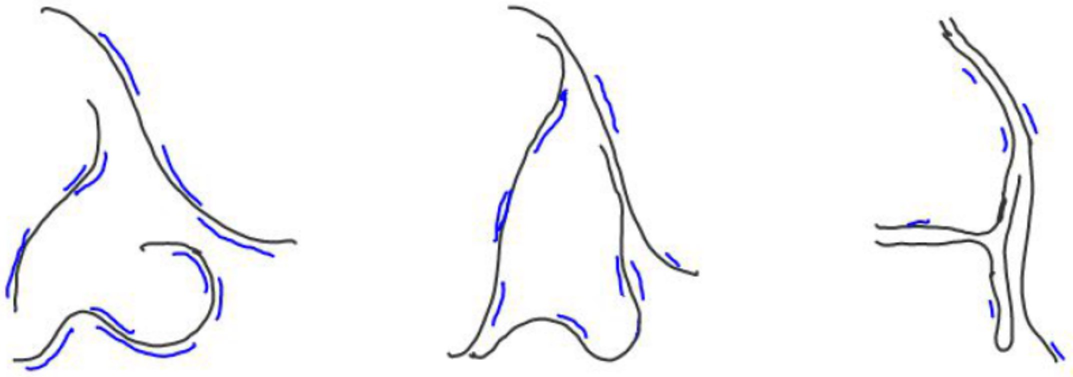

Figure 4.2: Schematic of the gelation process for graphene oxide hydrogels. Initially, the sheets are well separated and mostly covered with oxygen functional groups, indicated by the blue lines. As reduction proceeds, graphitized areas being to π-stack, leading to agglomeration and precipitation from the solvent. The final cross-linked structure retains some oxygen functional groups which retain the gels hydrophilic quality.

Concurrent with Xu's experiments, efforts at synthesizing graphene aerogels from GO suspensions were being pursued by Dr. Worsley *et al.* at Lawrence Livermore National Lab. Initial approaches followed those used for carbon nanotube aeorgels, which involved a solution of ricorcinol and formaldehyde as gelling agents. [52] It was subsequently found, however, that these agents were not absolutely necessary, and that the addition of sodium carbonate allowed for gelation to occur at 85 °C. [53] Alternately, ammonium hydroxide was used as a geling agent. [54]. The reduced temperature allows for facile synthesis of the aerogels by simply punching a hole in a rubber gasket, mounting it onto a microscope slide, and filling it with the GO suspension. A second glass slide is then placed on top and clamped together with binder clips. This results in disk-shaped gels having a high macroscopic surface area to volume ratio, which facilitates gas diffusion and improves handling in subsequent steps described below. Alternately, the gelation can occur in a sealed glass vial, resulting in a cylidrically shaped hydrogel. The gels are then rinsed thoroughly in deionoized water, which was finally exchanged with acetone. They were then supercritically dried until acetone condensation in the exhaust of the drying ceased.

High temperature thermal reduction

Unique to Dr. Worsley's approach was the further reduction of the reduced graphene oxide aerogel *via* high temperature thermal annealing, which resulted in a significant increase in graphitization. The graphene oxide aerogels were typically fired in an Ar or Ar/H_2 atmosphere at 1100 °C or 1600 °C. NMR studies of resulting graphene aerogels showed a near complete conversion of the material to sp^2-bound carbon. We also conducted experiments to study the effects of even higher temperatures, which we describe below.

High temperature annealing of GO in inert or reducing atmospheres has long been known to eliminate oxygen functional groups and increase the aromaticity of the material. However, it is also accompanied by large mass loss, owing to the evolution of carbon monoxide and carbon dioxide; oxygen is not found in the decomposition gases. [42]. It is important to note that pre-reduction of graphene oxide via the hydrothermal process described above is essential in maintaining a gel structure. In a control experiment, I heated graphene oxide foam directly in a nitrogen atmosphere at around 1700 °C; the sample was lost completely, presumably from the development of CO_2 and CO; this is very similar to a technique used in early attempts to exfoliate and simultaneously reduce GO to form graphene. [55] These gases not only carry off the carbon, but cause large pressures to build up between the graphene oxide sheets, leading to their sudden expansion and getting carried off in the flow of nitrogen gas. This direct approach also leads to highly degraded graphene flakes. This also suggests that oxygen-containing groups in the cross-links of the gel have largely been eliminated by the hydrothermal reduction process, since evolution of gas in between the sheets would otherwise cause the graphene sheets to separate upon thermal reduction.

Meso-scale Structures

We conducted a series of SEM and TEM investigations in order to gain further insight into the structure of the graphene aerogels. Samples were provided by Dr. Worsley using the method described above; Ms. Goldsetin also produced samples using an adaptation of Xu's pure-water process. To make the SEM sample, double-sided carbon tape was mounted onto an aluminum SEM mount; the gel was then pressed onto the opposite side of the tape and pulled off, leaving a small amount of gel behind. They were examined in a Sirion SEM operating at 5 keV.

On the meso-scale, the gel appears to be composed of aggregate layers of sheets arranged like wrinkled tissues. In some regions, partial alignment of the sheets leads to slit-shaped pores about 200 nm across. The structure differs significantly from that reported by Xu, where large, circular pores are found between the sheets which have little overlap and appear much smoother.

One explanation for the difference might be a difference in drying, *i.e.* freeze-drying *versus* supercritical drying; similar structures to those of Xu are obtained, for example, in a recent study by Sudeep who also employed freeze-drying. [56] Another difference with those studies is our use of high-temperature annealing, which likely leads to enhanced π-stacking between the sheets, leading to smaller pores. It would be instructive to perform further SEM characterization of the gels as a function of annealing temperature and duration to confirm this and further quantify this effect. The density of initial GO suspension may also play a role.

The role of the exchange of acetone before supercritical drying may also play an important role. An early study by Wen found that the exchange of water by acetone in aqueous

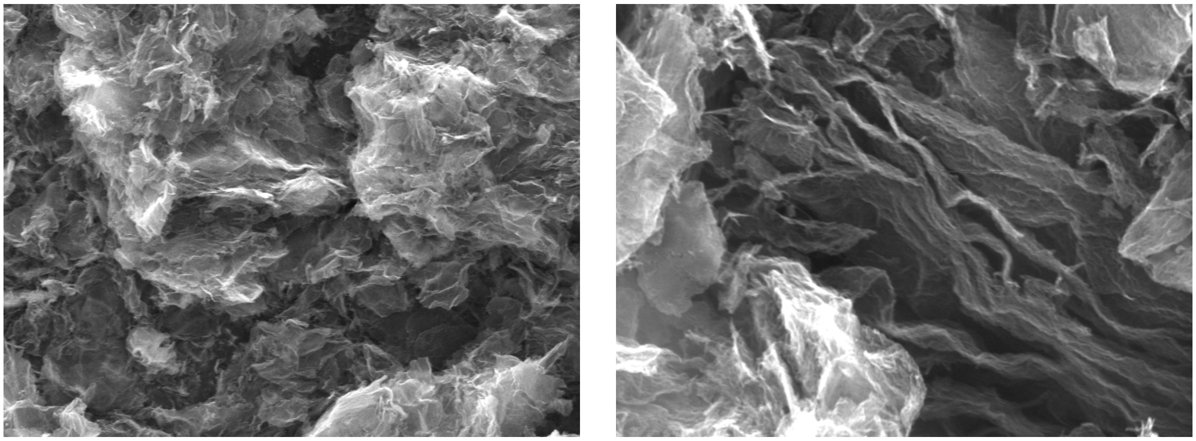

Figure 4.3: SEM images of graphene aerogels.

dispersion of GO caused the sheets to crumple into a three-dimetional configuration, which was attributed to the lowered polarity of the solvent. A follow-up study by Spector also found that GO tends to crumple into compact objects upon dispersion in acteone, although the crumpled phase was not observed for GO in a solution of sodium hydroxide. [57] Although our GO sheets have been largely deoxygenated, some functional groups certainly remain, so that the effects of solvent changing can still be significant.

Low-magnification TEM images were also taken to analyze the overall structure of the wrinkled sheets making up the aerogel. Samples were prepared by simply rubbing the grids against the sample. They were examined in a low-voltage DeLong TEM operating at 5 keV. Representative images are shown in Figure 4.4. In addition to the small wrinkles which texture the surface of the sheets, larger folds with a length scale of several hundred nanometers in length and about 50 nm in width can be seen. In the left image, the wrinkled sheet has folded up into a triangular crease, the wall of which are oriented perpendicular to the electron beam, resulting in much higher contrast. In the image on the right, two sheets can be seen laying atop one another. A small hole, about 100 nm across, is also seen at the edge of the top sheet.

The gels were also examined in high resolution TEM, operating at 80 kEV. Samples were prepared by sonication in isopropanol and drop-casting onto lacey carbon grids. Figure 4.5 shows two representative images taken at 30k and 120k magnification, respectively. On the left, two wrinkled sheets can be seen overlapping on the right side of the image where the contrast undergoes an abrupt change; the addition of a second sheet also blurs the finer structure of the wrinkles. Larger folds seen in the LVTEM can be seen in other images (not shown). In the image on the right the smaller wrinkles, measuring about 2 nm across and between 15 and 30 nm in length, can be made out more clearly. Some larger, wider winkles can also be seen. The spacing between the smaller wrinkles is roughly uniform at around 15 - 20 nm.

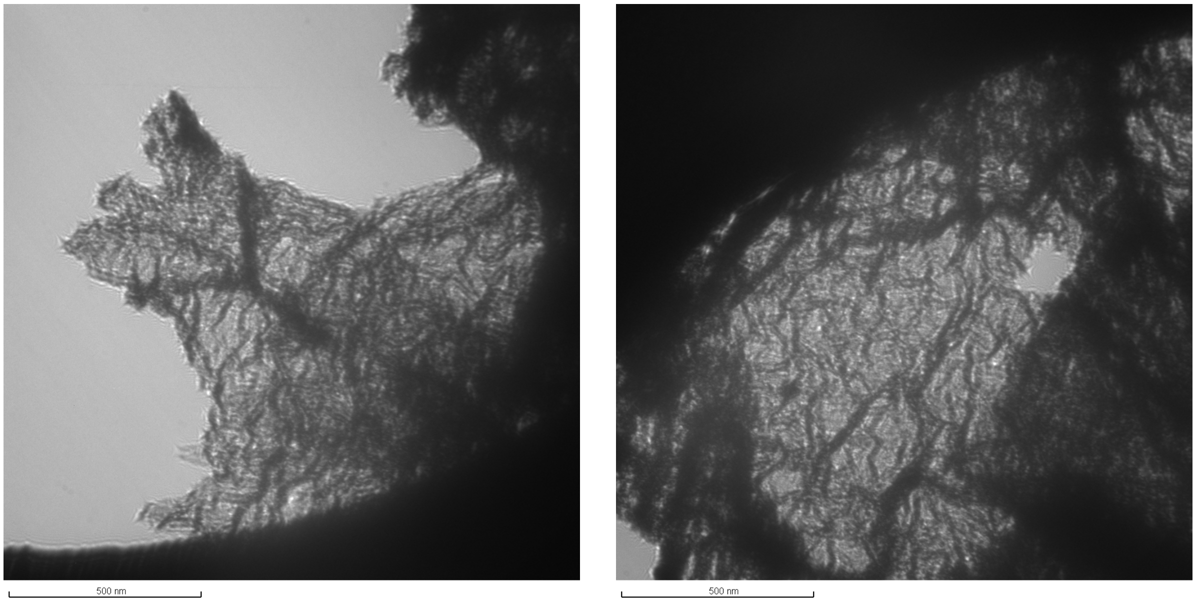

Figure 4.4: Low-voltage TEM images of graphene aerogels.

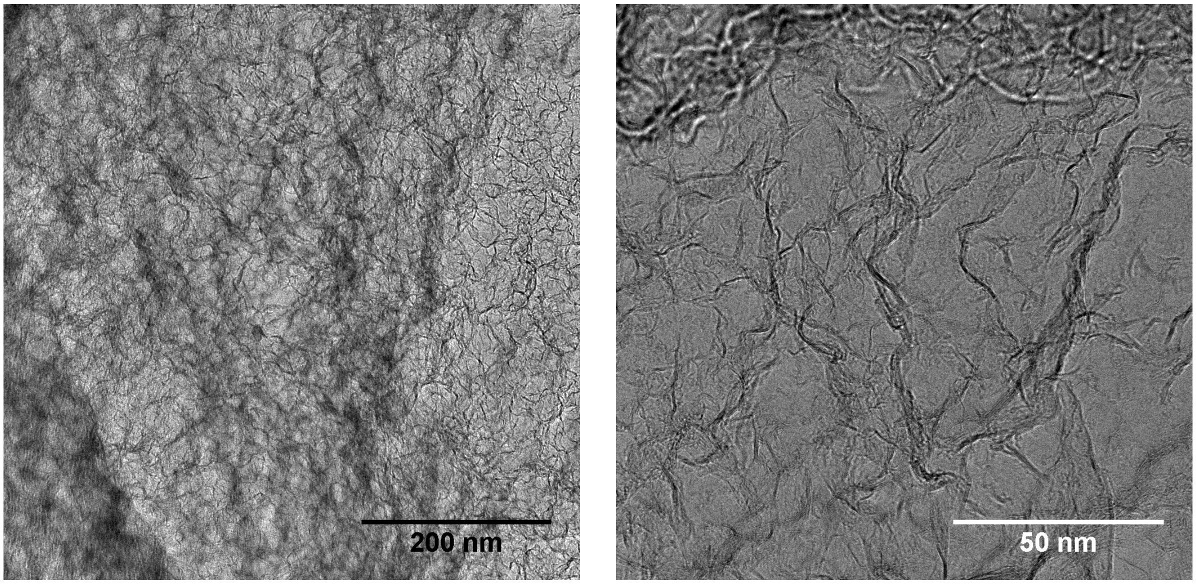

Figure 4.5: TEM images of graphene aerogels showing structure of the wrinkled sheets. Samples were annealed at 1600 °C. Images by William Mickelson.

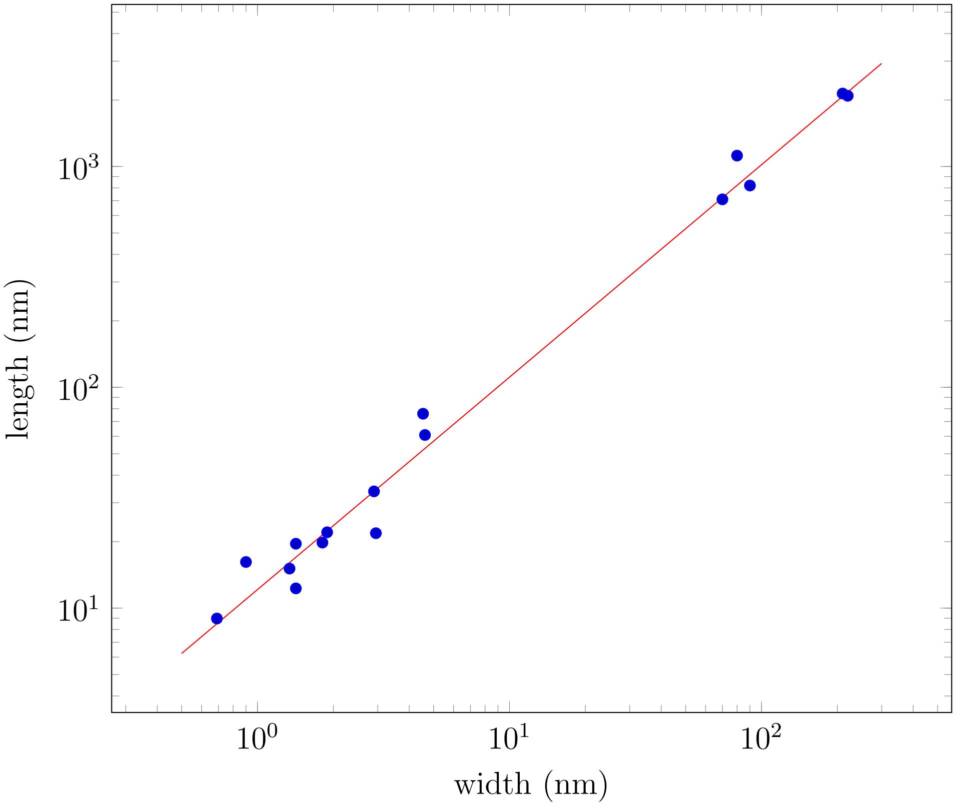

Figure 4.6: Scaling relation between wrinkle width and length for graphene aerogels.

The appearance of wrinkles on multiple scales is interesting, and suggests a fractal-like architecture for the gels. Figure 4.6 shows the scaling relation between the width and length of the wrinkles in the graphene aerogel sheets. It is observed that the relation is roughly linear, with a scaling exponent of approximately 1.04. This is different than what is expected in the crumpling an elastic sheet like paper, where the relation $R \approx h^{1/3}X^{2/3}$ is expected to hold, where R is the width of the wrinkle, h is the sheet thickness, and X is it length.[58]. This may be related to the fact that the bending rigidity of graphene does not follow the relation $\kappa \sim h^3$, from which the above relation is derived; the interlayer van der Waals forces, which make graphene an adhesive elastic sheet, may also play a role.

Fine structure of graphene wrinkles

Figure 4.7 shows two high-magnification TEM images of edges of the sheet which show the fine structure of the wrinkles. Dark fringes laying roughly parallel to one another indicate vertically oriented portions of the atomic layers making up the sheet. Interlayer spacing can be analyzed by taking a contrast profile across the fringes and fitting Gaussians to the respective peaks. It is found to vary widely, ranging from 0.37 to 0.43 nm, and is consistently

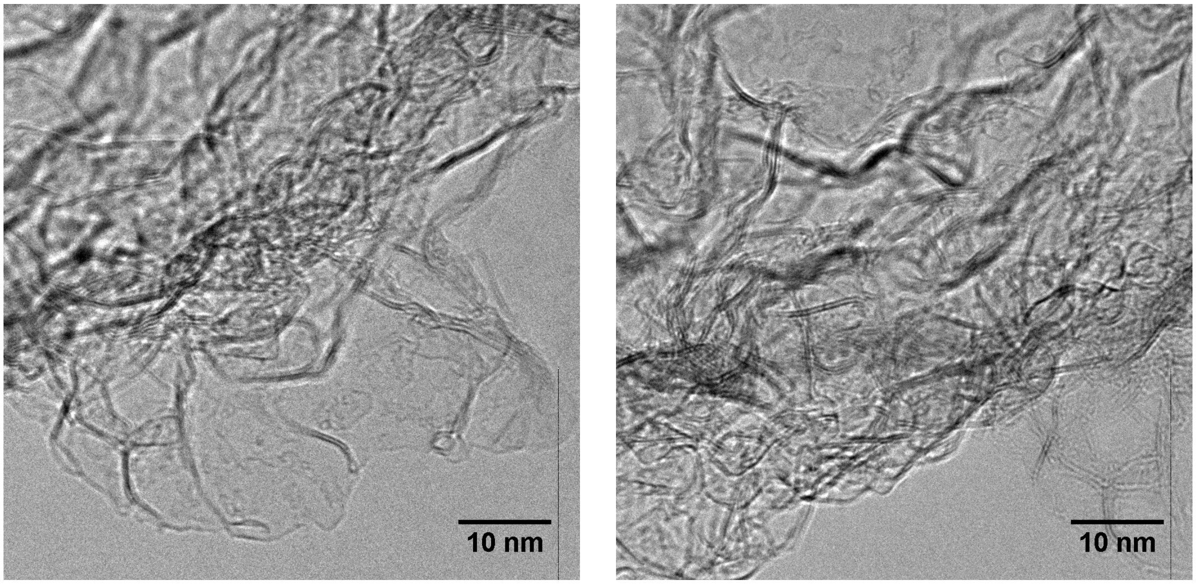

Figure 4.7: High magnification TEM images of graphene aerogels fired at 1600 °C under Ar. Image by William Mickelson.

larger than 0.335 nm, which is that of highly crystalline hexagonal graphite.

In Figure 4.8 we show one region of a graphene aerogel in two different focal planes. Comparison of the two images reveals that there are regions where the ridges and folds cross one another; this indicates that the sheet in this region is at least two layers, with ridges forming on either side. Many of these ridges are composed of three walls, indicating that the wrinkle has folded up into an accordion-like structure. Figure 4.9 shows a sketch of a possible model for the wrinkles observed in the graphene aerogels.

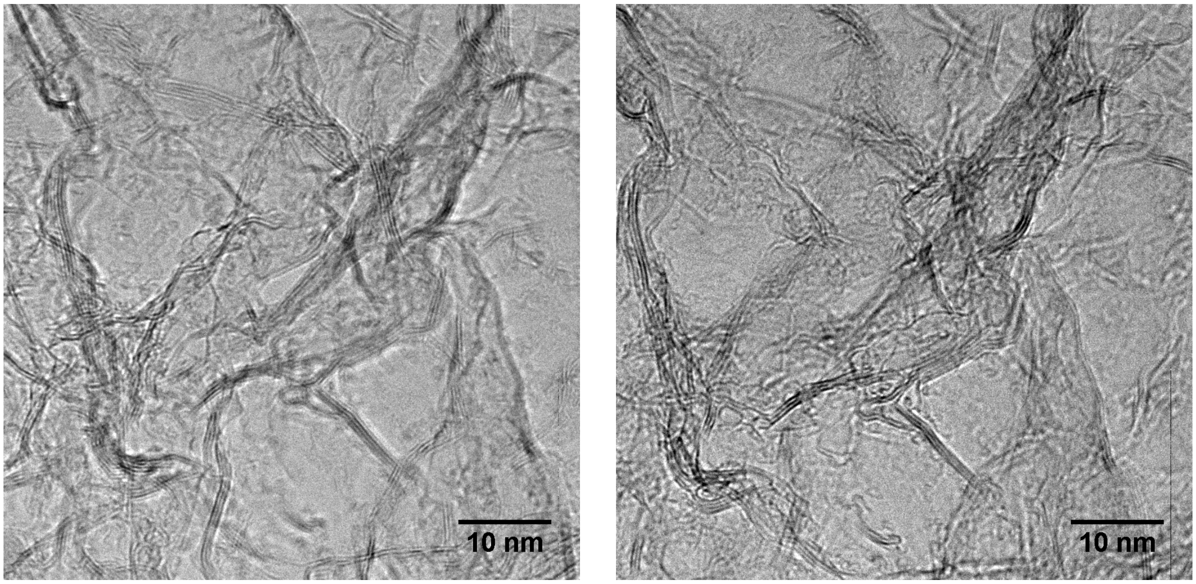

Figure 4.8: High magnification TEM images of graphene aerogels at two focal planes. Image by William Mickelson.

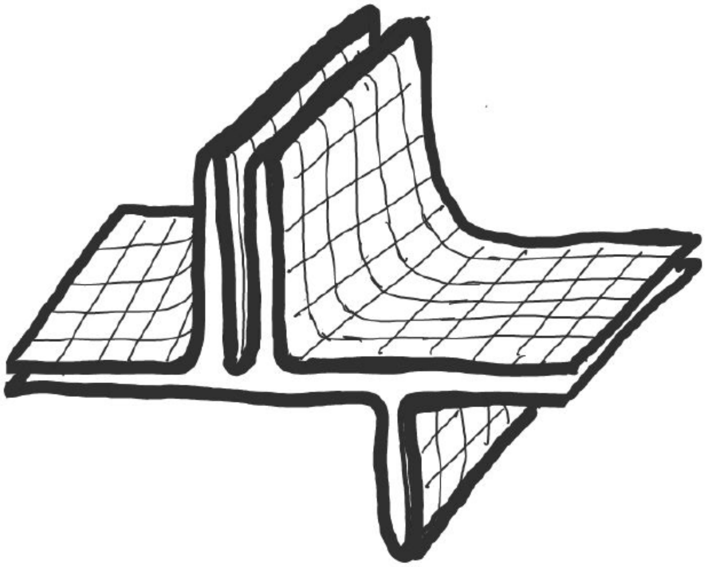

Figure 4.9: Model of a wrinkle in a graphene aerogel.

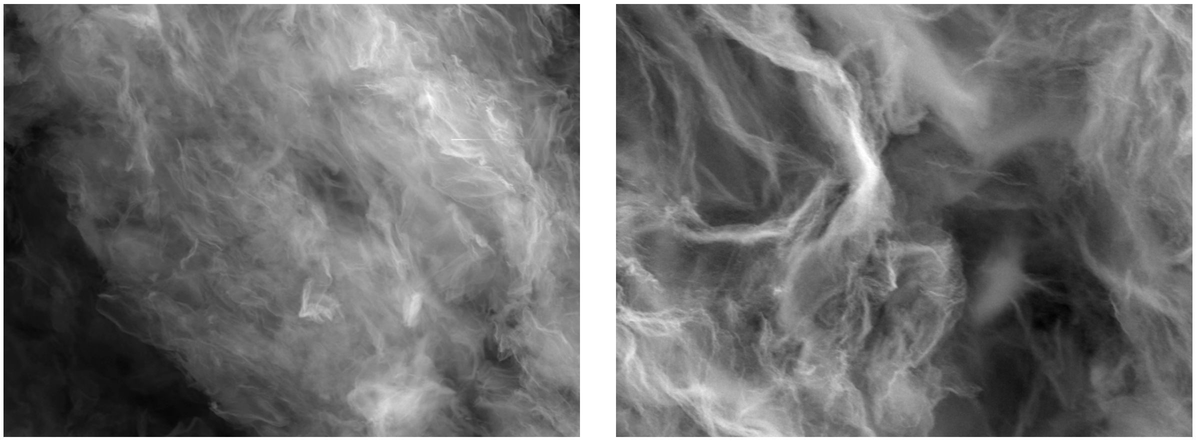

Figure 4.10: SEM images of BN aerogels.

4.2 Boron Nitride Aerogels

As mentioned in the Introduction, boron nitride (BN) shares many of the characteristics of graphene. The difference in electronegativity between boron and nitrogen, however, strongly breaks the symmetry of the graphene lattice, making BN a wide band gap, optically transparent insulator. This difference in electronegativity also accounts for some of BN's most interesting surface features. Of great interest in the research community is its enhanced physisorption properties.

The conversion of graphene aerogels to BN is discussed below in Section 5.3. Here, we look closely at the meso- and micro-level structure of the gels and compare them to the graphene gels above.

Meso-scale structures

We examined the meso-scale architecture of the BN aerogels much as we did the graphene aerogels. Figure 4.10 shows two SEM images of the gels; samples were prepared identically to the graphene gels above. Since BN is an insulator, it tends to charge up in the SEM and so imaging tend to be more problematic and at lower resolution. Similar structures to the graphene aerogels can be seen; the morphology on the micron-level appears much the same, with tissue-like sheets folded into each other forming slit-shaped macropores between them.

Low-voltage TEM images of the BN aerogels are shown in Figure 4.11. Significant differences from the graphene gels can be seen in these samples. In many parts, the gels are fractured, with small holes appearing between the wrinkles. The wrinkles themselves appear much more faceted and strait. Some larger-scale folds can be seen, though there tended to be fewer of these than in the graphene samples. It should be noted, however, that samples were much less consistent than in the case of the graphene aerogles; while the macro-level

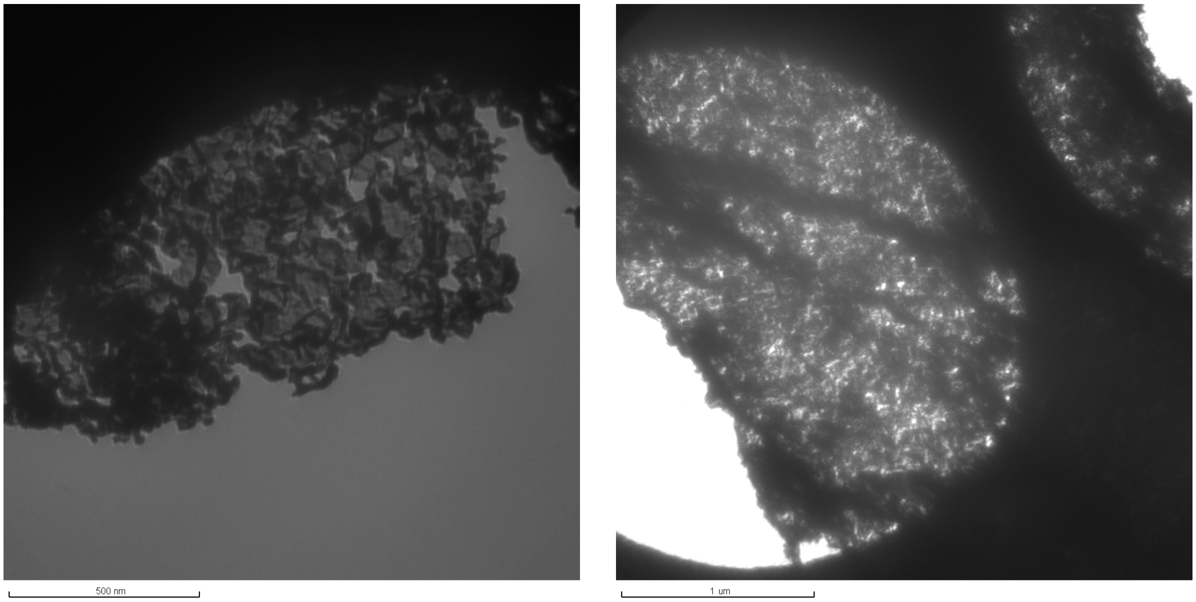

Figure 4.11: Low-voltage TEM images of BN aerogel sheets.

material almost always turned white after the conversion process, microstructure tended to vary significantly; see the discussion in Section 5.3. For example, in samples that tended to have larger specific surface area and were more robust mechanically, the gels tended to resemble the graphene gels more closely.

Figure 4.13 shows the scaling relation between the width and length of the crumples in the BN aerogels. A very different behavior is seen from that of the graphene aerogels. Here, the length of the crumples are nearly independent of the width at around 50 nm; the scaling exponent is only 0.213, whereas in the graphene gel it was nearly unity.

Layering and Cross-linking structure

As with the graphene aerogels discussed above, the layering and cross-linking structure of the BN aerogels were examined using TEM. Samples were prepared similarly to those of the graphene aerogels. A representative image is shown in Figure 4.14. Compared to the graphene aerogel shown in Figure 4.7, it is immediately evident that the facets of the sheet are much straighter. Here, we can see atomically straight planes more than 40 nm in length, as compared to the meandering fringes of the graphene aerogel.

The thickness of the sheets also appears to have increased, from two to three atomic layers in the case of the graphene aerogels, to six to eight in the present case. This increase in thickness is accompanied by an increase in the rigidity of the respective sheets, presumably by a factor of eight, since the rigidity goes at h^3, where h is the thickness of the sheet (see

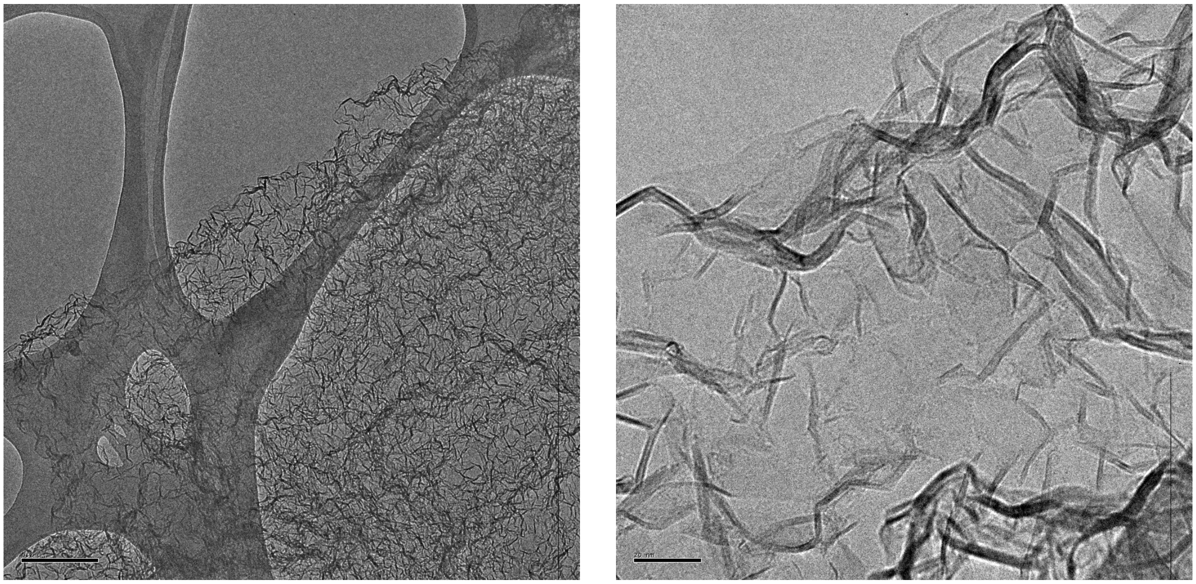

Figure 4.12: Mid-magnification TEM images of BN aerogel sheets. Images by William Mickelson.

earlier discussion). This likely accounts for the straighter walls observed in the BN sample as compared to the graphene. The stronger inter-layer binding of BN may also contribute to an increase in rigidity.

Nominally, if we assume the stoichiometry of carbothermal conversion, there should be a roughly four-thirds increase in the number of unit cells, or layers. If the conversion of the sheets is accompanied by a folding up the layers, we could then account for the observed increase ($3 \times 4/3 \times 2 = 8$). We should note, however, that for graphene aerogels fired under the same conditions but in the absence of boron oxide, wall thickness is indeed similar. The increase in wall thickness may then simply be due to the increase in temperature. Controlled experiments comparing converted gels pre-fired at various temperatures are necessary to distinguish between these two effects.

The interlayer spacing between the BN planes was analyzed by taking contrast profiles across the the wrinkles. The profiles were then analyzed using a Fourier-tranform technique. Upon taking the discrete Fourier transform of the profile, a prominent peak was found superimposed on a $1/f$ background. The $1/f$ background is a result of the stochastic sampling in the TEM. The peak corresponded to an interplanar spacing of 0.331 ± 0.0003 nm (the error is associated with the width of the peak). It was found to be highly consistent throughout the sample, indicating that the crystallinity was quite good. Deviations from this interplanar spacing were found at the intersections and edges of the wrinkles. This improvement of the crystallinity over the carbon percursor is consistent with other studies of carbothermal conversion on carbon structures. [59]

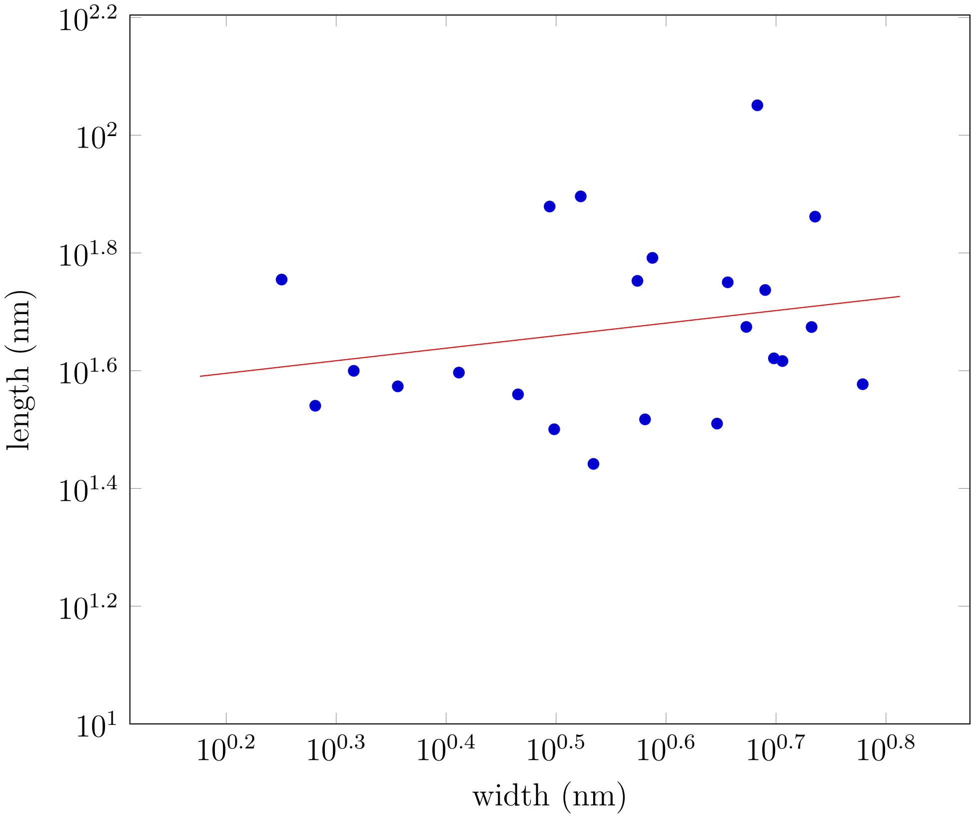

Figure 4.13: Scaling relation between wrinkle width and length for BN aerogels.

Another prominent feature seen in TEM images of the BN aerogels is the presence of rounded termination edges; an example can be seen at the end of the dark linear feature in Figure 4.14. The only possible explanation of such a feature is that it forms the edge of vertically oriented facet of the sheet.

One possible geometry that explains these vertical facets is that of the developable cone, or d-cone. An example of such a structure is shown in Figure 4.15. Such structures are thought to arise in the wrinkling of elastic sheets as a result of the coupling between the stretching and bending modes of the material.[60]

Finally, we found that, especially in areas where two sheets overlap, junctions between wrinkles could be found. A couple of examples are shown in Figure 4.16. We see that the facets of the gel split in parts, with some walls following one facet or another. The gel therefore appears to a type of interlaminated structure, where atomic planes are shared between the various sheets.

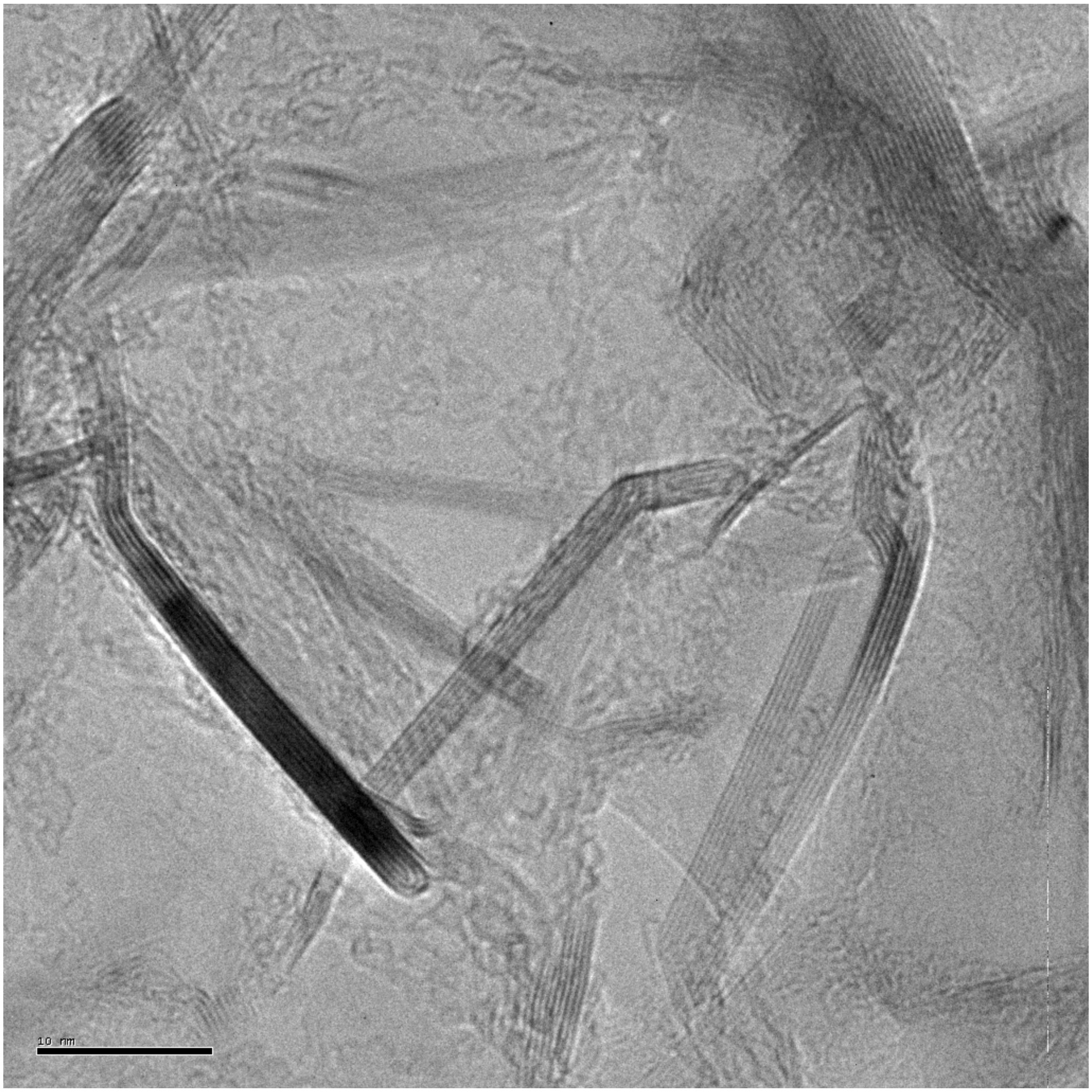

Figure 4.14: High magnification TEM image of a BN aerogel. Image by William Mickelson.

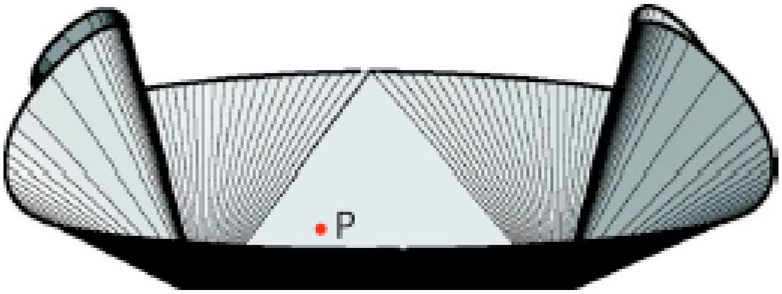

Figure 4.15: A developable cone. Adapted from Reference [60]

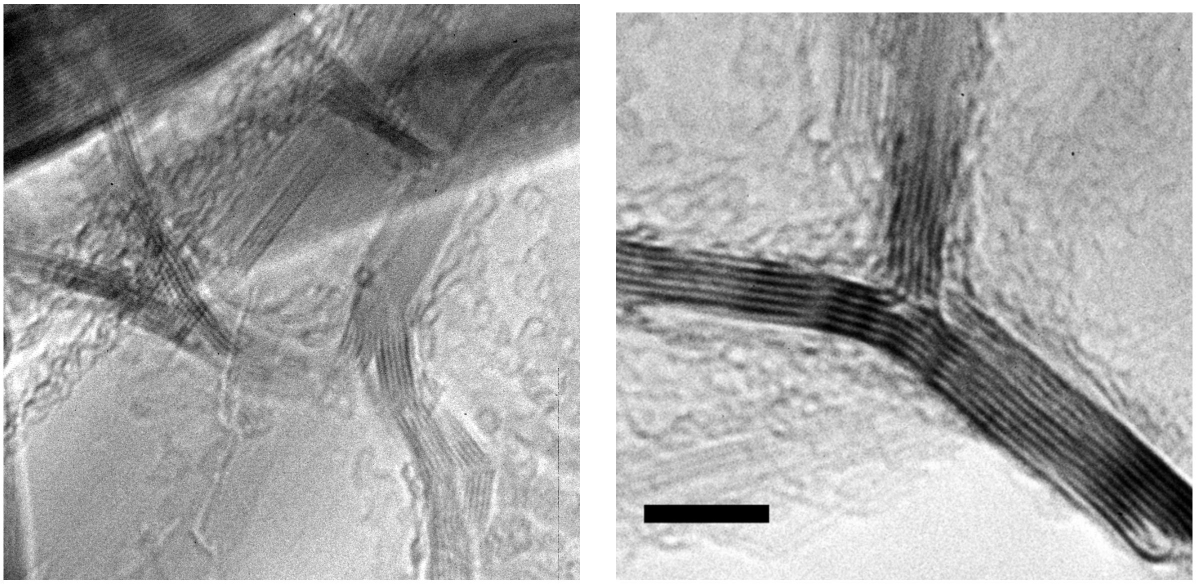

Figure 4.16: Examples of cross-linking structures in BN aerogels.

Part II

Synthesis of Boron Nitride Nanostructures

Chapter 5

Conversion of Carbon to Boron Nitride

5.1 Carbothermal reduction and simultaneous nitridation

Perhaps one of the oldest high temperature chemical processes known to man, carbothermal reduction refers to the general class of reactions wherein carbon is combined with an oxide to recover the pure element; the most ubiquitous example is the reaction of ore with coke in a blast furnace to produce pig iron. In the case of boron, the oxide is usually reduced with magnesium instead; this is because the reaction is more thermodynamically favorable at lower temperature and the byproducts are easier to remove. The direct reduction of boron oxide with carbon in an atmosphere of noble gas leads instead to boron carbides.

On the other hand, the carbothermal reduction of boron oxide can be immediately followed by nitridation when performed in an atmosphere of diatomic nitrogen. The overall reaction is given by

$$\mathrm{B_2O_3} + \mathrm{N_2} + 3\,\mathrm{C} \longrightarrow 2\,\mathrm{BN} + 3\,\mathrm{CO} \tag{5.1}$$

This reaction was first reported by Wöhler and Sainte-Clare Deville in 1857; a commercial process was subsequently developed by Lindblad in 1919.[61] According to the classical Elligham diagram, the primary reduction of the boron oxide becomes thermodynamically favorable at around 1500 °C; at lower temperatures, the product tends to contain larger fractions of boron oxide and boron carbide.[62] This continues to be one of the predominate processes used today in the production of BN powder, where graphite or similar carbon sources are fired through a hot zone of a furnace together with boron oxide in a flow of nitrogen; excess boron oxide can be easily washed away with water, and the resulting powder is also burned in air at temperatures above 600 °C to oxidize any remaining carbon.[63]

Owing to the commercial usefulness of this chemistry, much development has been done in private corporations and little information is available in the open literature. There are however some limited studies available. An interesting study by Bartnitskaya *et al.*, which looked at the conversion process on fine-grained graphite particles under varying amounts of boron oxide, revealed that the reduction of boron oxide occurs on the surface of the carbon structure, with the result that the rough morphology of the original carbon structure is maintained.[64]. Another useful study by Aydoğdu concluded that the conversion likely occurs in the vapor phase, and is again surface-limited.[62]

Crucible design for vapor-phase conversion

One of the conclusions of both Aydogdu and Bartnitskaya in their studies of carbothermal reduction of boron oxide was that the reaction most likely occurred in the vapor phase. In many previous reports on the conversion of nanostructured carbons to BN (see below), the starting material would be placed on top of the boron oxide and heated together. Boron oxide melts at relatively low temperatures (around 450 °C) and easily wets both graphite and BN; the carbon material to be converted thus gets suspended in them melt, and is not exposed to the nitrogen gas.

Additionally, if not all the boron oxide was evaporated in a given run, the carbon/BN sample would remain embedded in a hard, brittle boron oxide glass, making retrieval very problematic. To avoid these problems, as well as any damage to the sample due to surface tension forces from liquid boron oxide, I designed a crucible assembly for use in a radio-frequency induction furnace which would keep the carbon material to be converted separate from the boron oxide melt. A schematic and CAD drawing of the crucible is shown in Figure 5.1. All parts are machined from high-density molded graphite. The central stem delivers nitrogen gas to the bottom of the crucible, where a melt of boron oxide is heated and slowly vaporized.

The design ensures that the boron oxide vapor mixes well with the nitrogen, and is carried upward through the perforated cup which holds the carbon sample to be converted. Owing to the nature of induction heating, it is also likely (though hard to measure directly) that the sample cup is at a slightly higher temperature than the surrounding crucible. This ensures that boron oxide vapor does not condense on the sample, possibly damaging the pore structure of the material.

Under normal operation, the crucible was held in the center of the induction coil of the furnace by means of graphitized carbon fiber insulation. Typically, a section of 1/8”-thick insulation was cut into a section 18” wide by 3’ long and rolled tightly around around a 2” diameter cylinder, such that the outside diameter of the resulting tube was slightly less than 4”. This was then slipped inside the quartz tube forming the chamber of the induction furnace. A smaller piece of insulation was then rolled up to make a 2” diamter by 4” tall cylinder, which was wedged into the bottom of the larger tube of insulation; when mounted into the furnace, this formed a cavity into which the crucible was placed.

The sample was then added to the cup in the central stem, and lowered into the crucible using long tweezers. Finally, a second roll of insulation, 2” in diameter with a 1/2” hole in the center was slipped over the top, such that the central stem protruded through the hole about 1”. This top piece of insulation was essential to maintain adequate temperatures in the furnace. The lid of the furnace was then put in place, and an alumina tube was lowered and fit into the top of the protruding stem. In some designs the top of the stem was flared and the central hole slightly widened with a size ”F” drill to facilitate insertion of the alumina tube. It was important, however, to not widen the hole too much, as the thermal expansion of the alumina at operating temperatures was used to ensure an air-tight fit.

Conversion of crucible and standard operation

To prepare the crucible for use, it was found to be advantageous to first use the conversion process to line the interior with BN. This would ensure uniformity of conversion for small-mass samples from run to run. To this end, about 10 grams of coarse boron oxide power was added to the crucible before insertion into the furnace, and the central stem was loaded without a sample. The chamber was evacuated to around 1 inHg and flushed with nitrogen three times.

It was often found necessary to dry out the insulation in the furnace, as well as dehydrate the boron oxide. To this end, the pressure was then lowered to about 15 inHg under a flow of around 1500 sccm nitrogen. The crucible was first heated at 10% power (about 1.25 kW), resulting in a temperature of approximately 600 °C. Temperature measurements *via* optical pyrometry were difficult owing to limited optical access to the crucible, and the fact that any small holes proving such access would quickly become occluded with boron oxide condensate.

After about 10 minutes, the system is dry, and the conversion process can take place. Power is usually raised to around 35%, or about 4.3 kW. The crucible rapidly heats up to a bright red; estimated temperatures for the center of the crucible are 1600 - 1800 °C. A wisp of white smoke usually emerges around the central stem, and the cold walls of the quartz begin to cloud with boron oxide. This progresses for approximately five to ten minutes, or until all the boron oxide has evaporated. The power is then turned off and the crucible allowed to cool, which usually takes about two hours. The result is that the interior lining of the crucible is converted to BN.

5.2 Conversion of activated carbon

The conversion process had been studied in 2004 on activated charcoal by Han *et al.* in the Zettl group using a horizontal high-temperature furnace. [65]. This usually resulted in a an intermediate boron nitride/carbon product which was subsequently purified by burning off the carbon in air at 600 °C. The experiments on activated carbon were reproduced by myself and Dr. Brian Kessler in 2010. These experiments were also useful as calibration and test runs for the induction furnace before attempts were made with more scarce samples such as graphene aerogels (see below). They also allow one to gauge the effectiveness of new crucible designs.

In a typical run, about 1 g of activated charcoal (Calgon brand) with a grain size of about 1 mm was placed in the sample cup. About 10 g of boron oxide was loaded into the

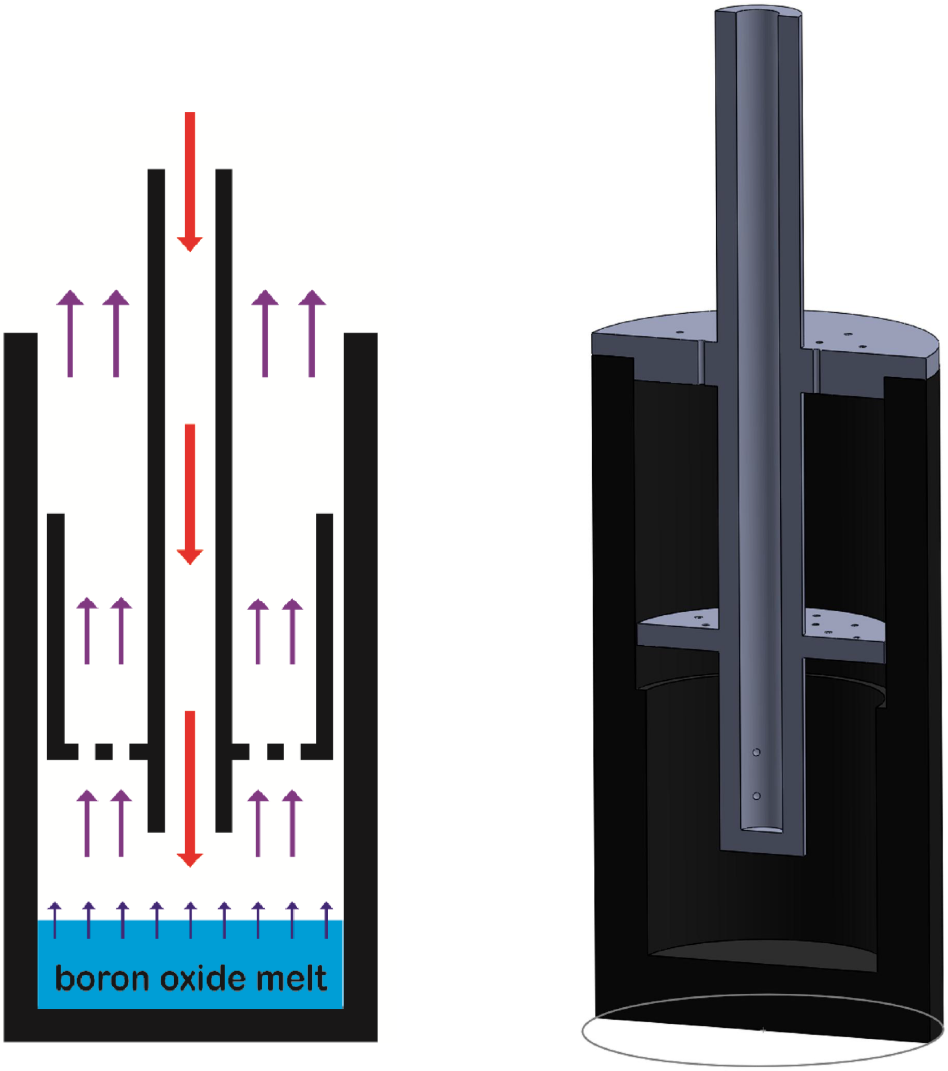

Figure 5.1: (left) Schematic of conversion crucible used to convert carbon nanostructures; red arrows indicate flow of nitrogen, blue arrows are boron oxide vapor, and purple arrows are a mixture of the two; black represents graphite. The carbon sample to be converted is placed in the central perforated cup.(right) CAD drawing of a similar crucible, where the cup has been replaced by a disk. Both grey and black represent graphite; the grey parts are one unit which can be loaded separately into the furnace. Drawing is to scale. The crucible is 2” outer diameter with 1/4” thick walls. The central stem in 1/2” outer diameter, 1/4” inner diameter and is composed of three parts: the central section, about one inch long, is tapped with 1/2” – 18 threads into which the top and bottom sections are screwed in; the cup and cap are held in place between the top and bottom parts of the stem, respectively.

bottom of the crucible, and the process described in the above section was run. Typically, products had a "salt and pepper" look, with some grain converting completely, while others remained largely greyish. To obtain purer BN samples, it was easy (though time-consuming) to simply pick out the white grains from the rest.

5.3 Conversion of graphene aerogels

The conversion of the graphene aerogels to BN was far more sensitive to the experimental conditions than for activated carbon. General discussion and detailed microanalysis of the graphene and BN aerogels is presented above in Section 4.2. Here we give details of the conversion process itself, and also analyze the crystalline and chemical composition of the material using X-ray diffractrometry (XRD), resonant Raman spectrosopy, and electron energy loss specrometry (EELS).

Details of Conversion Process

We used the crucible described above for the conversion process. We note from the outset that the conversion of graphene aerogels was far more sensitive to experimental conditions that for activated carbon, particularly if a high-quality, high surface area gel was desired. First, it was important to pre-melt the boron oxide powder into a solid mass. Separate observations of the heating of the boron oxide powder in a box furnace at 500 °C indicated that, upon melting, the powder mass would often froth up to many times its initial volume. This was presumably due to gas which was caught underneath a skin of viscous boron oxide, which would subsequently bubble out. This large volume increase would inevitably lead to the boron oxide touching the sample; in the case of the aerogels, this could be rather destructive owing to their fragile pores, which would collapse upon evaporation of a highly viscous fluid such as boron oxide.

Secondly, the positioning of the crucible was found to be important. It needed to be placed directly in the center of the coil. Otherwise, conversion would often result in very low surface area gels that did not at all resemble the initial graphene aerogel under microscopic analysis; for example, they would often be composed of plate-like particles, and would be extremely fragile. This may be because of unfavorable temperature gradients that would be established under these conditions.

The amount of boron oxide used also seemed to play a role. In a set of control experiments, I used one, three and ten grams of boron oxide, respectively. The first two cases resulted in gels that were slightly grey; the last was completely white. The grey is presumably due to residual, unconverted carbon.

Figure 5.2 shows a photograph of a starting graphene aerogel next to a converted BN aerogel. The complete change of color for converted aerogels, when appropriate amounts of boron oxide was used, was quite striking. If the gel is broken open, it is found that the interior is also completely white. The complete conversion of the gel is likely owing to the

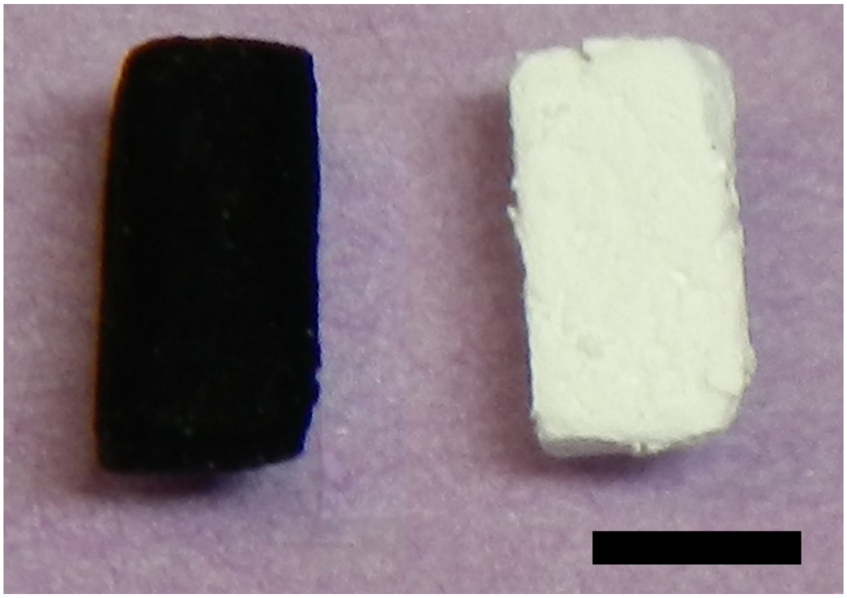

Figure 5.2: Photograph of a graphene aerogel and a converted BN aerogel. Scale bar is 5 mm. Photograph by Anna Goldstein.

extremely high surface area of the starting materia. As discussed above, the conversion process is surface-passivated, so using a carbon material which is composed of only one to two layers of graphene exposes all the carbon to the reactive gases.

X-ray Diffractometry

XRD analysis of the sample was conducted by Anna Goldstein using a diffractometer in the lab of Dr. Peidong Yang in the Department of Chemistry. Figure 5.3 shows the resulting spectrum. The peaks in the XRD spectrum corresponding to spacing of the dominant lattice planes in the sample according to the Bragg formula

$$2d \sin\theta = n\lambda \tag{5.2}$$

where d is the interplanar spacing, n is an integer, and λ is the wavelength of the incident radiation; here we use Cu-K_α radiation with a wavelength $\lambda = 0.154$ nm. The wide peak centered at $2\theta \approx 27^\circ$thus corresponding to an interplanar spacing of approximately 0.330 ± 0.006 nm, which is consistent with the interplanar spacing of sp^2-bonded BN sheets of rhomohedral or hexagonal BN. The breadth of the peak can be due to several effects. [66]

- Instrumentation broadening. It was found that the spectrum depended sensitively on the height of the sample in the diffractometer.
- Non-uniform strain in the sample. As we saw in Section 4.2, the planes of BN are bent into folds, which can causes a variation in the interplanar spacing.

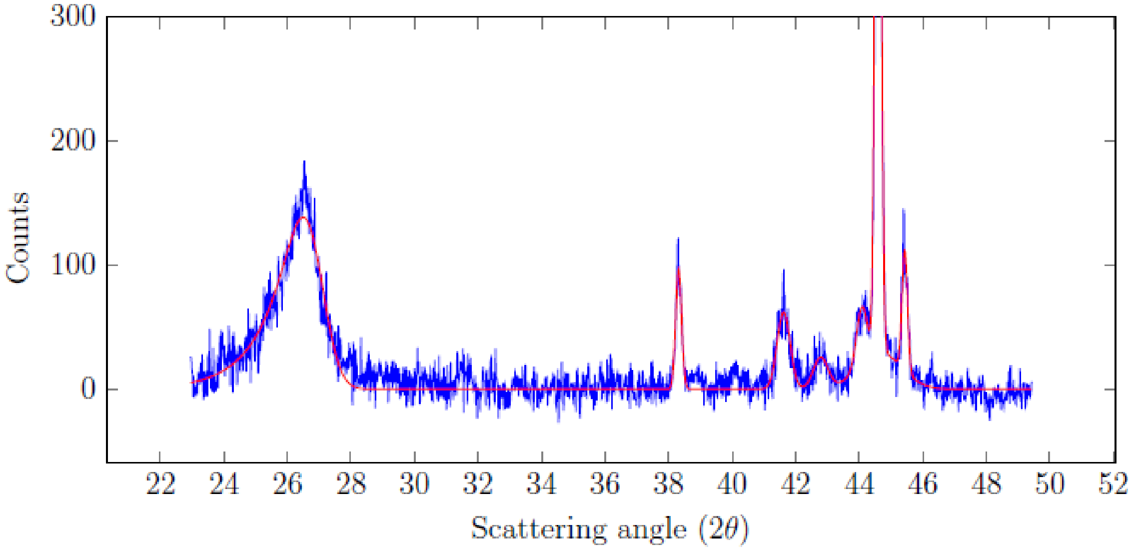

Peak Center	Peak Width	Assignment
26.982	0.722	rBN, hBN
38.299	0.066	Al (substrate)
41.623	0.126	hBN
42.861	0.114	rBN
43.980	0.136	hBN
44.595	0.123	Al (substrate)
45.406	0.074	rBN

Figure 5.3: X-ray diffraction spectrum of a BN aerogel. Blue line shows data, red line shows a Levenberg-Marquardt fit using a Gaussian basis. Peak assignments are listed in the corresponding table. Data collected by Anna Goldstein.

- Finite crystallite size. Again, as seen in Section 4.2, the sheets of the aerogel are five to eight atomic layers thick. The Sherrer equation relates the broadening of peaks to finite crystallite size,

  $$\beta = \frac{K\lambda}{\tau \cos\theta} \tag{5.3}$$

  where β is the FWHM of the diffraction peak, $K \approx 0.9$ is a shape factor, and τ is the crystallite size.

For our observed sheet thickness, the Sherrer equation gives $\beta \approx 0.08$, so does not account for most of the broadening of the interlayer peak; we are left to conclude that it is due either to instrumental broadening, or asymmetric strain in the sample due to bending of the BN sheets.

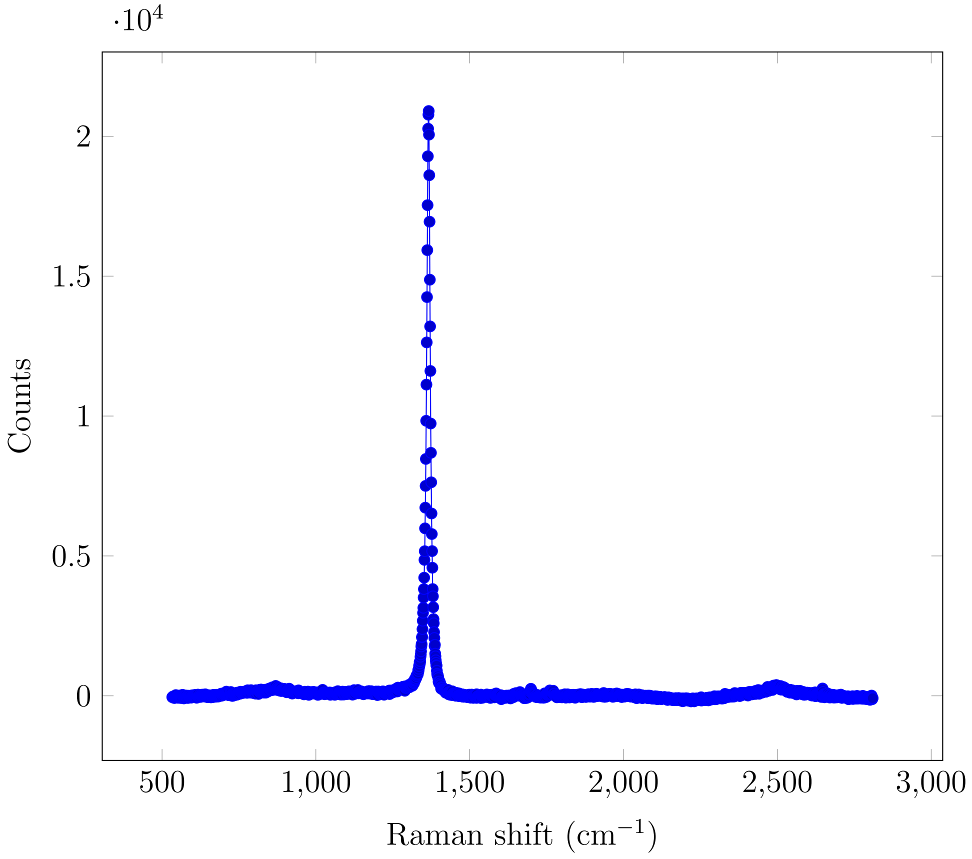

Figure 5.4: Resonant Raman spectrum of a BN aerogel. Peak center is at 1365.8 cm^{-1} with a FWHM of 13.23 cm^{-1}

Resonant Raman spectroscopy

As in the case of graphene aerogels above, Raman spectroscopy can be used to analyze the cyrstalline structure of our BN aerogels. The Raman active modes of BN were first measured and analyzed by Geick *et al.* in 1966, who found that BN has one bright, active Raman active phonon mode, E_{2g}, at 1370 cm^{-1}. This is the same anti-symmetric, in-plane mode that is responsible for the G band in graphene. Later studies on pyrolytic BN established this peak at 1366.2 cm^{-1} with a natural linewidth of 9.1 cm^{-1}.

Figure 5.4 shows a resonant Raman spectrum of a BN aerogel, taken with a 514 nm excitation laser. A background of about 1000 counts has been subtracted from the signal. A sharp peak centered at 1365.8 cm^{-1} is clearly evident. A Lorentzian fit using a Levenberg-Marquardt algorithm gives a FWHM of 13.23 cm^{-1}.

The slight broadening of the Raman peak is worth considering in detail. The very close fit of the spectrum to Lorentian suggests that this broadening is not due to disorder. It may instead be due to finite phonon lifetimes, as is often found in the Raman spectrum of nanoparticles.

A study by Nemanich *et al.* studied the effects of finite cystalline size on the Raman spectrum of graphite and BN.[67] They found that the peak in BN exhibited both a shift in peak position and a broadening as the size of the cystallites decreased. Empirically, the FWHM of the E_{2g} peak was found to be $\Gamma_{1/2} = (141.7/L_a + 8.70)$ cm^{-1}, where L_a is the crystallite size in nm. For our measured FWHM, this corresponds to $L_a = 31.3$ nm. This is roughly the size of the wrinkles that we see in our TEM images. It is plausible that the folds in the BN sheets effectively divide the crystal into small crystallites, hence shortening the lifetimes of the in-plane phonons, and giving rise to the observed broadening of the Raman peak. Interestingly, we do not observe a corresponding shift in the peak position.

Electron Energy Loss Spectroscopy

The high quality of the Raman spectrum shown above is a strong indication of sp^2 bonding in the atomic layers of the BN aerogel. Further support, as well as a quantitative measure of the chemical purity of the sample, can be found using electron energy loss spectroscopy (EELS).

As electrons in the TEM pass through the sample, they can scatter inelastically with the electrons occupying the orbitals of the constituent atoms, losing a characteristic amount of energy in the process. The electrons emerging for the sample are then passed through a magnetic prism and continue onto the detection apparatus, in our case, the CCD camera used for imaging. The microscope used in our experiment is also equipped with a Gatan imaging filter, which contains a series of electromagnets which compensate for geometrical distortions due to projection onto the flat surface of the CCD and enhance the energy resolution of the instrument. The image formed on the CCD is a series of bands; the brightness of the bands is measured along a contour and plotted, showing the spectrum of the collected electrons.

This spectrum always has a characteristic zero-loss peak due to non-interacting electrons and elastic scattering, followed by a series of peaks indicative of the types of atoms in the sample. The signal-to-noise of an EELS spectrum is thus proportional to the ratio of inelastic to elastic scattering, which is roughly C/Z, where C is a constant dependent on the incident electron energy (about 20 for the 80 keV electrons we use in our experiment), and Z is the atomic number of the atom. Hence, scattering is most effective for low-Z elements such as boron, carbon and nitrogen, making EELS a particularly effective tool for our samples.

For low-Z elements, inelastic scattering is dominated by excitation of the core K-shell electrons, resulting in sharp edges. Past the ionization threshold E_a, the scattering cross section for inner shell electrons can be approximated by a simple power law,

$$\frac{d\sigma_a}{dE} \sim \begin{cases} 0 & \text{if } E < E_a \\ E^{-s} & \text{if } E \geq E_a \end{cases} \tag{5.4}$$

where typically $2 < s < 6$, giving rise to saw-tooth like spectral features. The differential scattering cross-section of course has a strong angular dependence, meaning that the direction

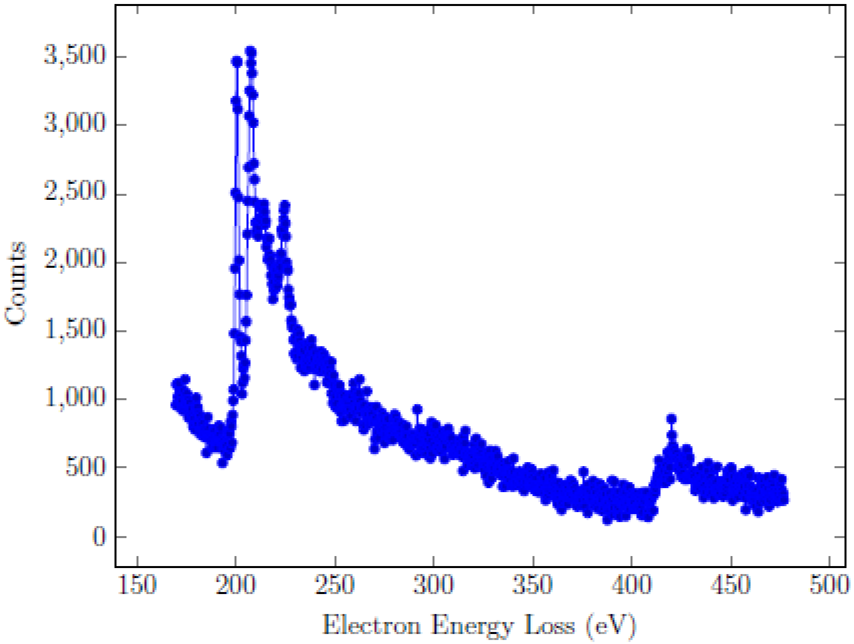

Figure 5.5: Electron energy loss spectrum of a BN aerogel. The features evident near 188 eV are due to K-shell excitation of boron; the sharp triple-peak is indicative of sp^2 bonding. The peak near 400 eV is due to K-shell excitation of nitrogen. Spectrum taken by William Mickelson at the National Center for Electron Microscopy, Lawrence Berkeley National Laboratory.

of the incident electrons, collection angle, *etc.* are important in a full analysis. We will ignore these detail here for simplicity. Reference [68], *Electron Energy-Loss Spectroscopy in the Electron Microscope* by Egerton, from which this discussion is adopted, provides and excellent and detailed overview of the subject.

Figure 5.5 shows an EELS spectrum of a BN aerogel taken over a probe radius of about 50 nm. The distinct features near 200 eV are due to K-shell excitation of boron. The peak near 400 eV is likewise due to K-shell excitation of nitrogen. Notably absent is any appreciable peak due to carbon, which would normally appear around 284 eV. This is further proof that the aerogel has been completely converted to BN.

Since the thickness of our aerogels sheets are less than the mean free path of the incident electrons, they only scatter once as they pass through the sample. This greatly simplifies the quantitative analysis of our EELS spectrum, since we need not deconvolve separate scattering events. For single-event scattering, the differential scattering intensity from from an element is given by

$$J_a(E) = N_a I_0 \frac{d\sigma_a}{dE} \tag{5.5}$$

where N_a is the is number of atoms of element a per unit area and I_0 is the incident electron flux. By resolving the measured scattering intensity into components based Equation 5.4, the atomic ratios of the elements making up the sample can be measured with some degree of accuracy. For our spectrum, the B/N ratio was determined to be 0.97 ± 0.14, while the carbon content was less than 5%.

Energy Loss Near Edge Structure

Beyond atomic ratios, the EELS spectrum can reveal details of the bonding structure of an element through the exact shape of the ionization edge, known in the literature as the energy loss near edge structure (ELNES). This is particularly evident in our sample in the case of the boron edge, which is enlarged in Figure 5.6 to show the details of the ELNES. As is well known from quantum mechanics, the scattering cross-section is dependent on the availability of final states in a particular energy (i.e. Fermi's Golden Rule),

$$\frac{d\sigma_a}{dE} \sim |M_{ab}|^2 \varrho(E) \tag{5.6}$$

where M_{ab} is the matrix element connecting the two states (which may depend on direction as well as energy), and $\varrho(E)$ is the density of final states per unit energy. For sp^2-bonded BN, the bottom of the conduction band is made up of π^* anti-bonding orbitals, and lies at or around the vacuum level, meaning that electrons ionized from the core K (i.e. $1s$) shell may transition to these states, giving rise to the sharp peak at the left end of the boron edge. The σ^* band is relatively flat and lies a few eV above the π^* band; transitions to this band account for the second prominent peak in the ELENS spectrum. The exact calculation of the ELNES spectrum is somewhat more involved, but this gives the general idea. This particular edge structure differs significantly from that of sp^3-bonded boron, as is found in cubic BN, which would exhibit more widely separated primary peaks.

5.4 Surface conversion of carbon fibers

In the present section, we describe the conversion process as applied to carbon fibers. Carbon filaments derived from organic material such as cellulose were first used in incandescent lamps in the late 19th century. Modern carbon fibers were developed by the Union Carbide Corporation during World War II, with further development and commercial availability the late 1950s and early 1960s.[69, 70] Worldwide production of carbon fibers was nearly 100,000 metric tons in 2011, and continues to grow rapidly.[71] Most commercial carbon fibers are derived from polyacylonitrile (PAN) precursors and subsequently graphitized at high temperatures. These fibers find applications in structural parts ranging from bicycle frames to airliners. Less common are pitch-based fibers, which usually have a lower tensile strength but a higher elastic modulus. Carbon fibers and filaments can also be made from the pyrolysis of hydrocarbons in the presence of a metal catalyst, though these are rare, expensive and of limited application.[70]

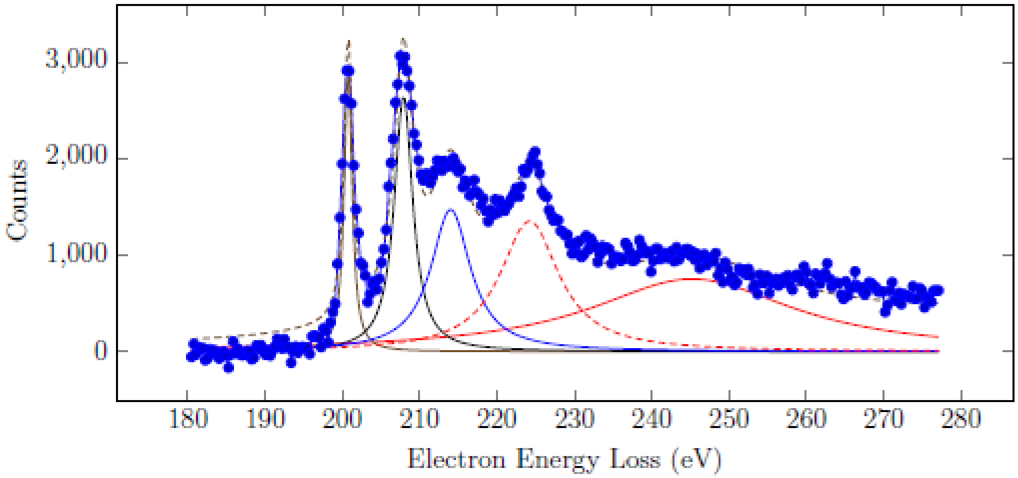

Figure 5.6: Near-edge fine structure of the boron peaks from Figure 5.5. The first peak to the left is referred to as π^* since it is due to excitations away from the the π orbitals. The second large peak is likewise termed σ^*.

PAN based fibers can contain up to 10% nitrogen by weight, with the carbon taking a forms from graphitic to amorphous. However, the exterior skin of both pitch and PAN based fibers does tend to be graphitic. The orientation of the layers on the skin can vary from radial to spiral to circumferential depending of the method of production.[70]

BN fibers, though far less common and much more expensive, have also been developed. They are usually made via preceramic precursors, either through the reaction of boron oxide fibers with ammonia,[72] or spun directly from polyborylborazine [73] or poly-borazinylamine precursors.[74] The corrosion resistance of BN fibers makes them attractive in many applications, as well as their white color, which broadens their applicability in textiles and consumer products. However, these fibers tend to have lower tensile strengths and modulus than carbon fibers. BN coatings on carbon and ceramic fibers have also been reported.[75] Below we detail a new method using the BN conversion process for creating such coatings which is complete, scaleable, and low cost compared to previous methods.

Pitch-based fibers

The conversion was first tried on pitch-based fibers. These were in fact begin used already as insulation for the furnace. After a conversion attempt of carbon nanotubes (see below), I noticed that some of the fibers appeared purple. I attributed this to a transparent coating on their surface. I surmised that this must be BN, and decided to examine the phenomenon in more detail under more controlled conditions.

Pitch-based carbon fibers are typically less expensive than PAN fibers (see below), being commonly used in insulation for furnaces and in carbon-carbon composites such as airline

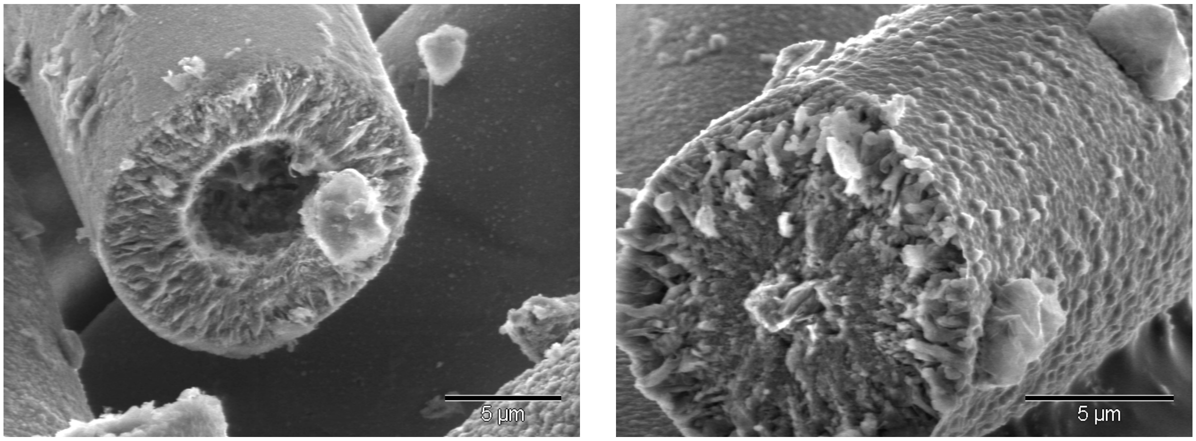

Figure 5.7: SEM images of partially converted (left) fully converted (right) pitch-based carbon fibers after heating at 1 hr at 750 °C in air.

brakes where high modulus is preferred over high tensile strength. The fibers we used are Kreca C from the Kureha Corp. in Japan. In a typical run, about 1 g of fibers was drawn from a mat and arranged in the conversion cup. About 10 g of boron oxide was used, and typically about 3 kW of power applied for 1 hour.

Most runs resulted in a combination of purely white fibers – which were very fragile – interspersed with black fibers, many of which attained a purple sheen. They were both tested for oxidation resistance; neither sample displayed any appreciable change or mass loss after being heated for 1 hour at 750 °C in air.

The samples were then examined in the SEM; two representative micrographs are shown in Figure 5.7. The partially converted fiber on the left shows two distinct phases in its cross section. The brighter contrast of the exterior shell indicates an insulating material. EDS measurements shown in the left panel of Figure 5.8 indicate that the shell was largely composed of stoichiometric amounts of boron and nitrogen, with low carbon and no oxygen signal. The grains of the shell appear to be radially oriented, and the conversion has penetrated about 2 microns towards the center. The total radius of the tubes is unchanged from the starting material. On the exterior, knob-like particles can been seen protruding from the body of the fiber. The central five microns of the fiber remain unconverted, with an EDS signal, shown in the right panel of Figure 5.8, indicating increasing amounts of carbon and diminished boron and nitrogen signals as one moves inwards toward the fiber axis. The oxidation treatment in air appears to have slightly hollowed out the end of the carbon core.

The fully converted fiber on the right displays a distinct morphology from that on the left. Here, the grains on the outside appear much more coarse, and larger knobs as protrude from the fiber surface as well as small ones. EDS measurements show a roughly uniform BN stoichiometry throughout the cross section of the fiber, with no measurable carbon or oxygen content. Overall fiber diameter is roughly the same as the partially converted and

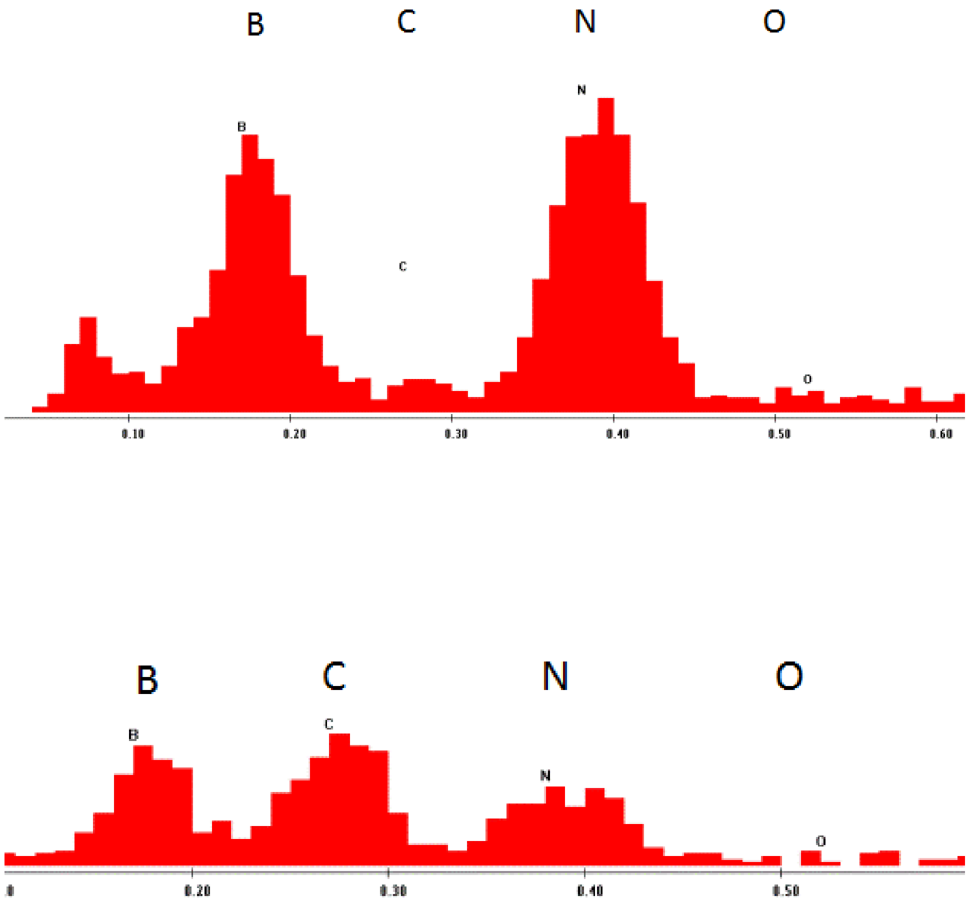

Figure 5.8: EDS spectra of converted pitch-based carbon fibers. (left) Spectrum taken from the exterior shell of the fibers showing a pure BN signal. (right) Spectrum from the center of the fibers, showing a residual carbon signal.

unconverted fibers.

Hollow Boron Nitride Microtubules

Inspired by the small amount of burning found in the fibers treated at 750 °C in air for 1 hour, it seemed plausible that it would be possible to continue the process longer and hollow out the BN-converted fibers completely. A sample of converted pitch-based fibers was chopped up finely with a razor blade into short segments about 1 mm long. They were then baked at 750 °C in air for 12 hours, after which time they acquired a glass fiber-like appearance, with little remaining black carbon material.

Figure 5.9 shows two SEM images of the hollowed out BN microtubules. This hollowing

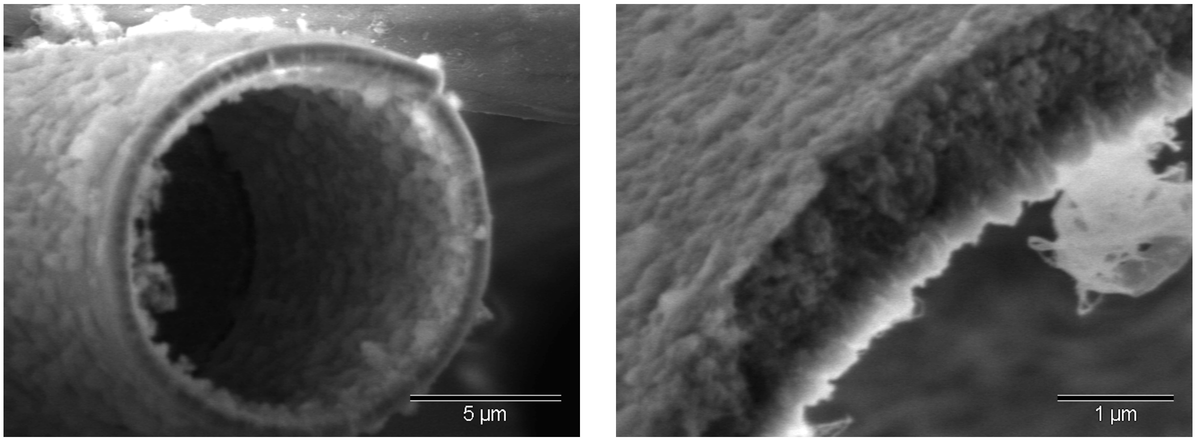

Figure 5.9: SEM images of hollowed out BN-converted pitch fibers, forming hollow BN microtubules.

out exhibits the uniformity of the surface conversion, showing a fairly uniform shell about 600 - 800 nm thick in most cases. The grains appear to be mostly radially oriented, forming a stable structure much like a Roman arch. Both interior and exterior of the shells are dotted with protrusions, which show pure BN stoichiometry under EDS analysis. Various shapes are also possible, depending on the cross-section of the original carbon fiber.

Graphitized ex-PAN fibers

In another set of experiments, the conversion was attempted on the graphitized ex-PAN fibers which formed the other type of insulation used in the induction furnace. These were generally very short, on the order of a few millimeters, and pressed into a mat, which was easy to break apart manually. About 1 g of fibers was typically loaded into the conversion cup along with 10 g of boron oxide and run at high power, or about 3.75 kW for approximately 30 minutes. Macroscopically, the material would turn a light to medium grey and was fairly homogeneous. In all other respects is looked identical to the starting material.

Figure 5.10 shows SEM micrographs of the fibers before and after conversion. The starting fibers have a wrinkled skin, and are about 20 microns in diameter. Cross sections were fairly uniform; graphitic planes were somewhat visible but appear to have no particular orientation.

After conversion, the skin of the fiber lit up under the electron beam, likely due to the insulating layer of BN now covering its surface. The wrinkled appearance of the skin appears to have been preserved. Judging from the images, the skin layer was about 300 - 500 nm thick. The cross-section of a typical fiber was also highly non-uniform, with some sides experiencing far more conversion than others. This appears to be due to the lack of a specific initial orientation of the graphitic planes; the areas where the conversion penetrated

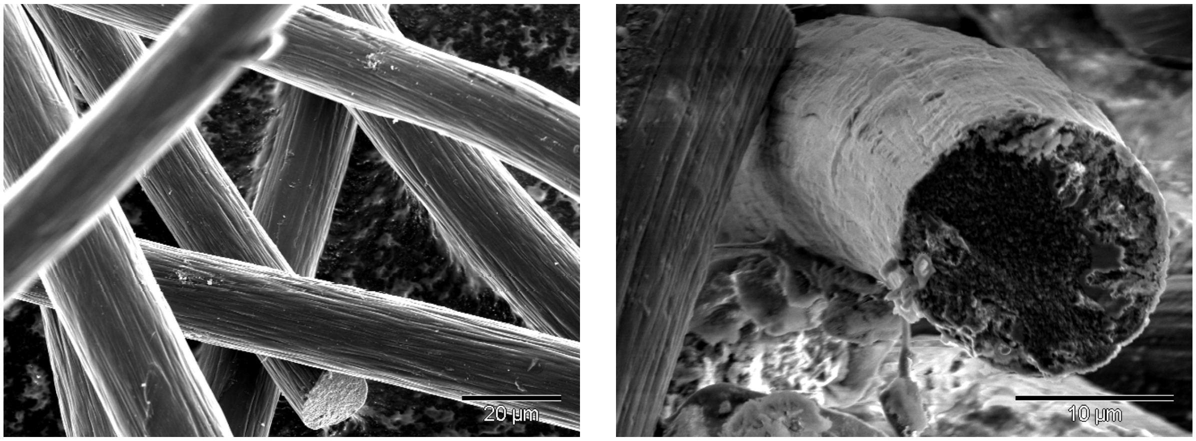

Figure 5.10: SEM images of ex-PAN graphitzied carbon fibers. (left) untreated fiber (right) fiber after high temperature conversion.

the fiber more completely tended to correspond with more axially-oriented graphitic planes.

Woven PAN fiber mats

The most successful and spectacular conversion was achieved by using mats and tows of commercial PAN fibers. These type of fibers are by far the most common in manufacturing and product development. The fibers themselves are spun from their polymer precursor and chemically stabilized at moderate temperatures, at around 180 to 300 °C. Usually the fiber is stretched at this stage, which helps align the aromatic regions along the fiber axis. Afterwards, they are carbonized at high temperature in an inert environment; high temperature treatment in nitrogen up to around 1500 °C is used for relatively inexpensive fibers, while treatment up to 3000 °C in argon is used for more expensive, high-performance applications.

Surface treatment of the fibers is essential for handling and incorporation into composites. Oxidative treatment is often used to functionalize the surface of the fibers so as to improve adhesion to matrix polymers. The fibers are then usually coated in a resin, termed *sizing* in the industry, to keep them from breaking. While these fibers possess incredibly high tensile strength and modulus, the are indeed very brittle, and can be easily cut with a pair of scissors. The are then grouped into a bundle of several thousand called a *tow* and either spun onto spindles or woven into mats. The latter form is the most common in the manufacture of parts such as bicycle frames and airline wings.

We acquired a few yards of woven PAN fiber from Applied Polyeramic in Benicia, California, as part of an informal collaborative effort to develop BN-based materials. To perform conversion on these mats, a new crucible was designed with slight modifications to the one described above. A schematic of the crucible is shown in Figure 5.11. The sample cup was removed, and the stem went directly towards the bottom. The upper portion of the crucible was bored to a slightly larger radius, forming a 3 mm ”shelf” near the bottom. The fiber

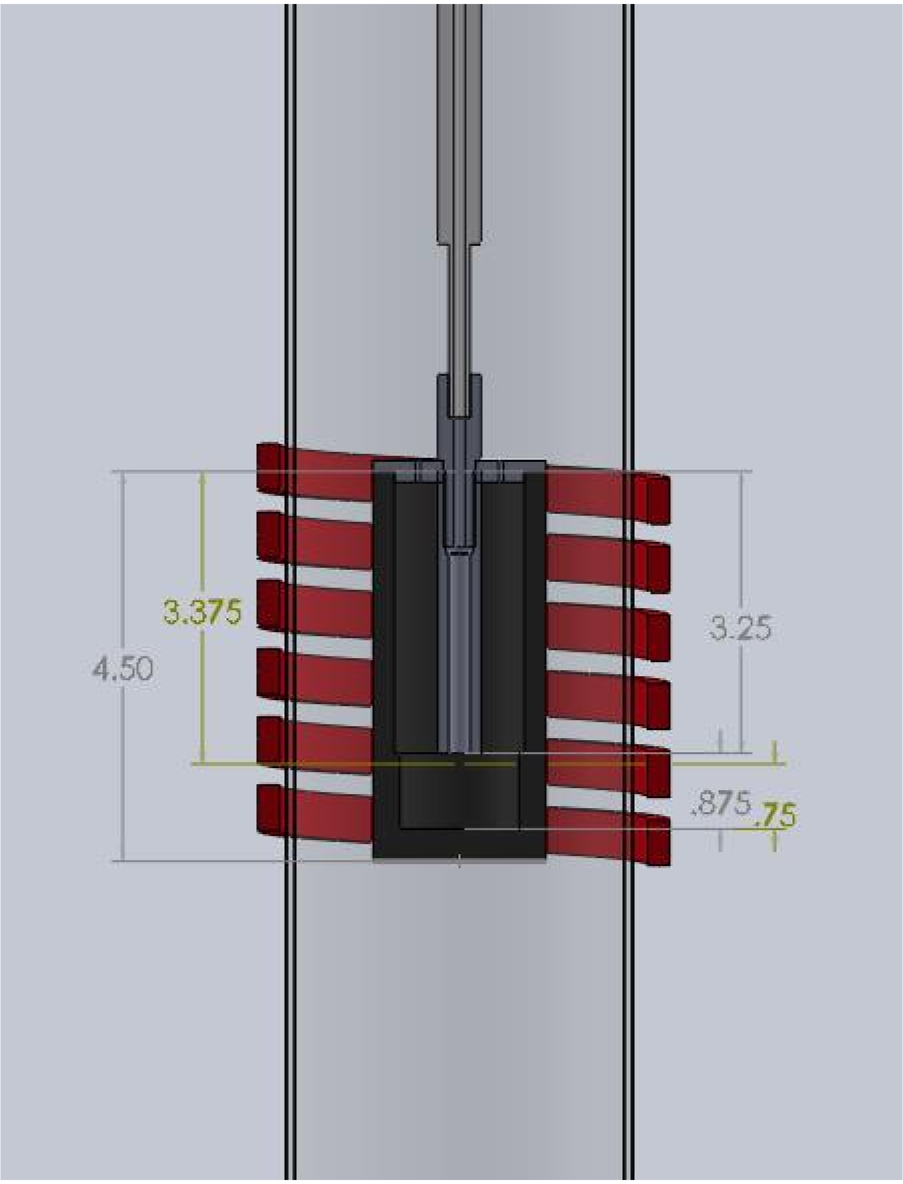

Figure 5.11: CAD drawing of the crucible used for PAN fiber conversion. Measurements are in inches.

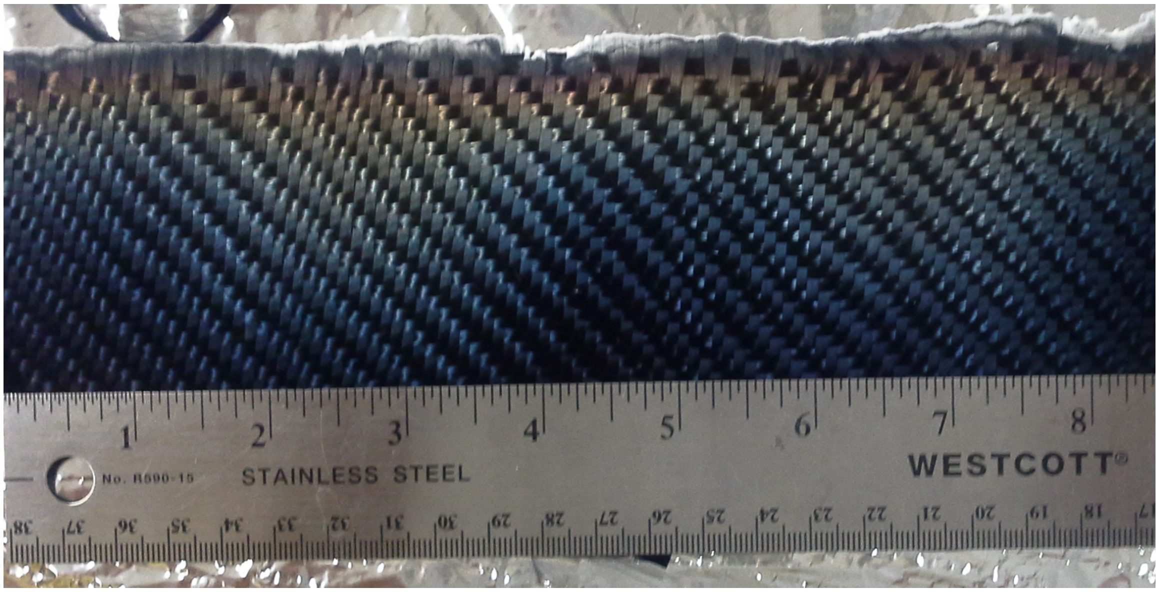

Figure 5.12: Photograph of a section of BN-converted PAN fiber mat, showing the change in color.

mats were then cut into 4" wide strips and about 3' long. These were rolled up and set directly into the crucible; the mat was arranged loosely and the crucible inserted into the furnace; the stem was then added as normal.

In a typical run, 10 g of boron oxide was used, with nitrogen flows between 1000 and 1500 sccm. Power was usually high, at around 3 kW. As the crucible heated up, a greenish-yellow vapor would rise and condense on the cold parts of the quartz; this was presumably the resin sizing burning off the surface. The process was typically run for about 1 hour.

Figure 5.12 shows a photograph of a mat after conversion. In the photo, the top of the mat has a thin white section which was closest to the boron oxide melt during the process; this white material is extremely brittle and composed of highly degraded fibers which have been completely converted to BN. As we move across the strip, there is an obvious color gradient, going from red for the fibers nearer to the boron oxide melt to purple/black for fibers furthest away. This color is most likely due to a thin-film interference effect: light reflecting of the surface of fiber interferes with light passing through the transparent BN coating and off of the carbon interior. For light at normal incidence, and given that multiple rainbow patterns are not observed, the thickness is then simply $t = \lambda/2n$, where λ is the dominant wavelength of the reflected light and $n = 1.8$ is the optical index of refraction of BN; this gives a thickness of between 100 and 200 nm.

This estimation of the thickness of the coating is corroborated by SEM images of the converted fibers. Figure 5.13 shows converted PAN fibers (left) and several converted fibers (right). As in the case of pitch fibers and highly graphitzied ex-PAN fibers, the conversion

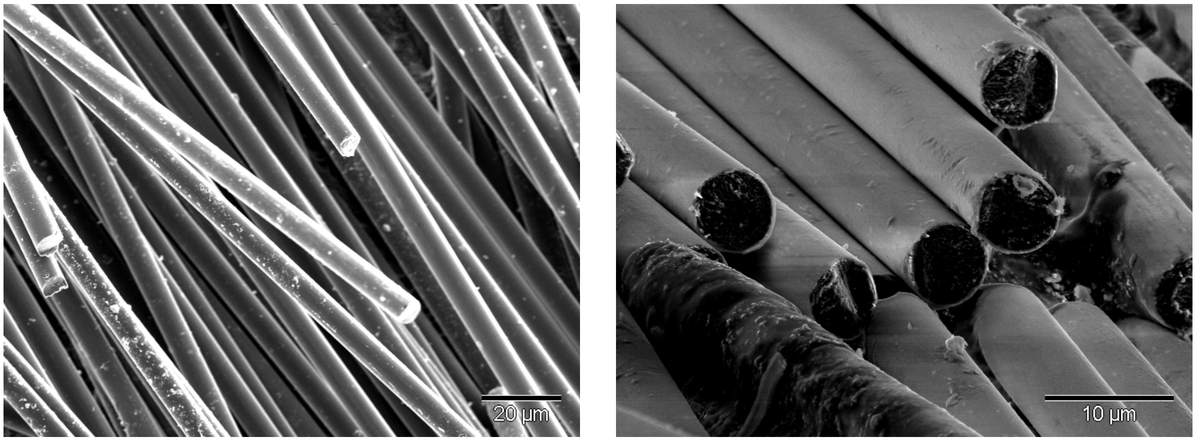

Figure 5.13: SEM images of original PAN-derived carbon fibers (left) and BN-converted PAN-derived fibers (right).

results in an insulating skin layer which appears brighter in the SEM. In this case, however, the skin layer is remarkably uniform, a there are very few instances of the conversion penetrating deep into the fiber interior. This may confer greater mechanical strength to the resulting material, making it more useful in the composite applications. The complete coating may also be useful in composite applications, particularly when increased oxidation resistance is needed. Further tests on the strength and modulus of the fibers is needed to evaluate their usefulness.

5.5 Conversion of carbon nanotubes

The conversion process was first applied to multi-walled carbon nanotubes by Han *et al.* in the Bando group at the National Institute of Materials Science in Tsukuba, Japan.[59] Because the reaction occurs on the surface, however, it becomes quickly passivated, with the result that the conversion to BN occurs mostly on the exposed surfaces of the tubes. The result is a phase-separated BN/C nanotube, which resembles is some ways a nanowire with a sheath of insulation.

I reproduced much of Han's work using the new crucible design, with some significant improvements. Various types of tubes were used, including

- HiPCO single walled tubes
- Nanotech labs multiwalled tubes (ferrocene derived)
- CNI double-walled tubes

with varying results. Owing to the gas flows associated with loading and unloading the crucible, many of these materials can pose problems as they become airborne and thus hazardous or get lost altogether. It is important to implement and follow proper safety procedures, handling these materials inside of a fume hood if necessary.

Even if loose tubes were successful loaded, they would often become lost in the synthesis gas flows. It was found very advantageous to aggregate the tubes somehow. In one approach, tubes were compressed into small chips about 5 mm across, by either compressing them between two plates in a small vice, or by simply pressing them against their container with a metal spatula. Samples tended to be somewhat inhomogeneous, with some chips partly converting and others completely or not at all. Additionally, the interior of thicker chips tended not to convert.

In another approach, I mixed the tubes vigorously in IPA to created a semi-homogeneous suspension of tube bundles about 100 microns across. Sonication was avoided to prevent tube breakage. This suspension was then pulled through an vacuum-filtration setup using an alumina filter, resulting in a thick, wet cake of nanotubes about 5 mm thick. The cake was allowed to dry in air for several minutes, and then placed in a vacuum furnace at around 100 °for half an hour. The resulting material held together decently well, while providing large macropores for exchange of synthesis gases. This tended to result in fairly homogeneous samples.

Parameters

In a typical run, between 1 and 10 mg of tubes are loaded into the central perforated cup. Flow rates of nitrogen range between 750 and 1500 sccm. Power ranges are between 3 and 5 kW. Between 1 and 10 grams of boron oxide were used. Under these conditions, the evaporation rate of boron oxide can vary widely, between 50 mg and 2 grams per minute, indicating that the internal temperature, which is not possible to measure accurately in our setup, also varies by several hundred degrees. Running time ranged from 20 minutes to 2 hours, depending on the applied power.

It was found that the resulting samples depended strongly on the amount of power applied, and less so on the reaction time and amount of precursors used. At lower power (1 to 2 kW), there was no obvious change in the CNTs; at medium power (2 to 3 kW), the product was grey, or a mixture of white and grey; at higher powers (above 3 kW), the conversion was often complete.

Single and Double-Walled Tubes

The conversion of single-walled carbon nanotubes (SWCNTs) is of particular interest, as the corresponding single-walled boron nitride nanotubes are rare and could serve as interesting samples for fundamental investigations. Little success was had, however, in these attempts. Both Alpha Alesar and HiPCO tubes were used, and in no cases did any retrievable sample remain. This may be been due to the sample getting swept away in the furnace gases. It may

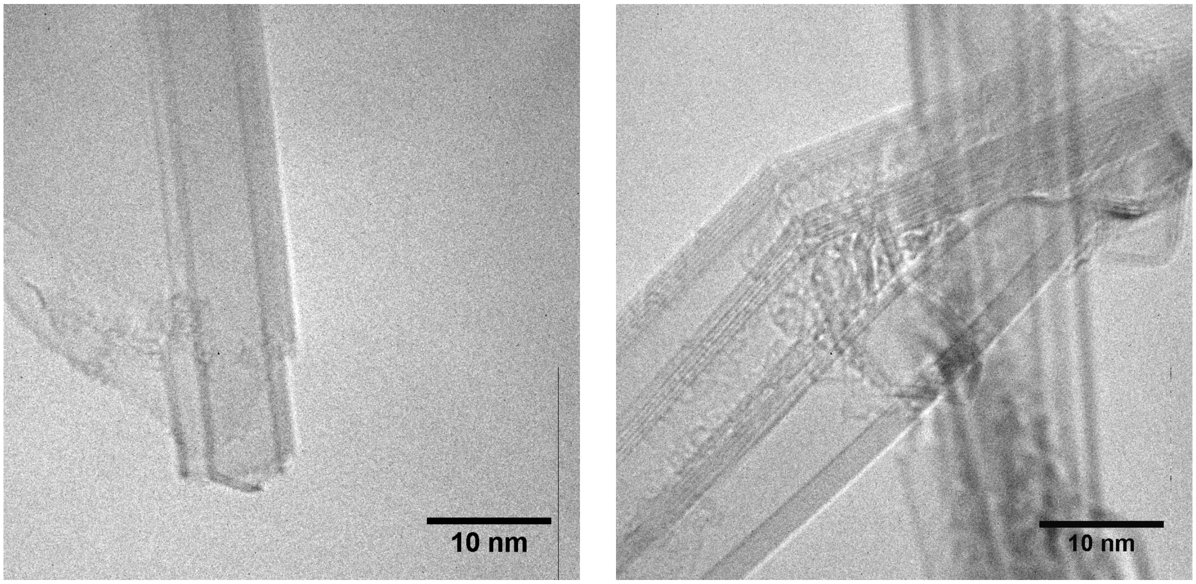

Figure 5.14: TEM images of converted double-walled carbon nanotubes.

be advantageous to attempt the conversion on buckypaper made from SWCNTs to prevent this. On other hand, previous reports of SWCNT conversion by the Golberg group seemed to confirm that SWCNTs rarely survive.[76] It may be, therefore, that the conversion process requires more than one layer to proceed.

Much more success was had in the conversion of double-walled carbon nanotubes (DWCNTs), even when the samples were placed loosely in the conversion cup. The macroscopic product was generally pure white and had the same fluffy consistency of the starting material.

Figure 5.14 shows two TEM images of converted double-walled nantobues. Wall thickness appears to have increased to around 5 or 6 layers in some cases. The overall crystallinity of the tubes was preserved. In some cases, however, an unraveling of the tubes could be seen, as in the left panel of Figure 5.14. This effect was particularly pronounced when the conversion ran at higher temperatures.

Multiwalled Tubes

Most attempts at conversion were on multi-walled carbon nanotubes (MWCNTs) sourced from CheapTubes, Inc (20-50 nm diameter). These tubes initially have a great deal of disorder, fractured walls, and are often segmented. They are however an inexpensive alternative to higher quality tubes, and are particularly useful for testing out ranges of synthesis parameter. Usually about 10 mg of tubes could be converted at once using about 10 g of boron oxide. Power could be kept moderately low, at around 20%, and still get appreciable results. Material would often convert completely around the holes in the cup, while turning a light grey away from the holes. Pure white material could be easily collected and anlayzed.

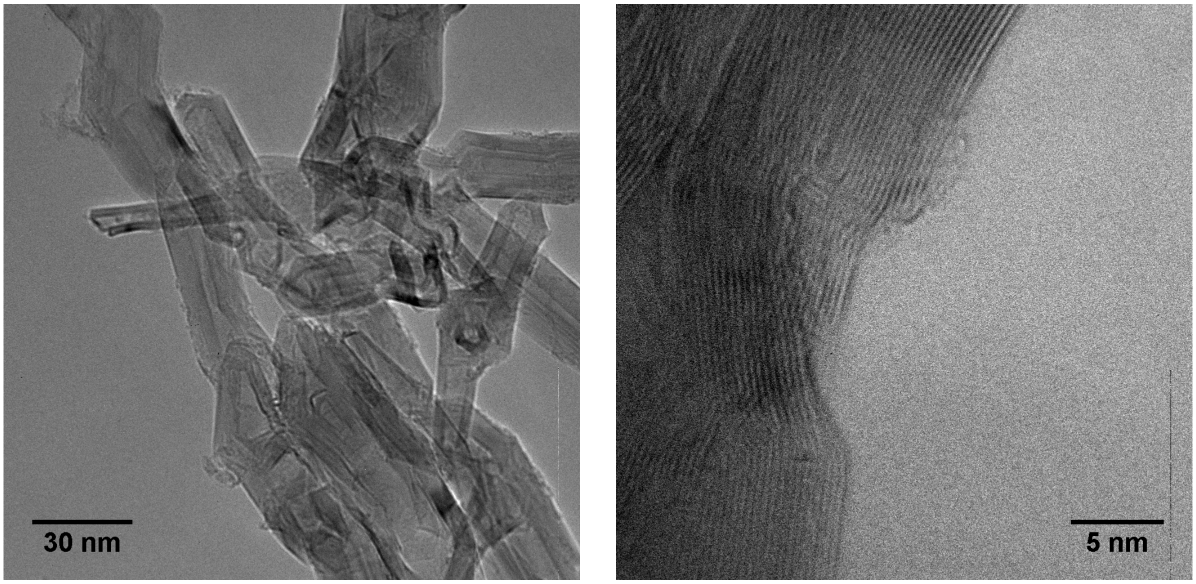

Figure 5.15: TEM images of converted multi-walled carbon nanotubes.

Figure 5.15 shows TEM images of the converted material. As with many BNNTs, end terminations tended to be angular. Compared to the starting material, the converted tubes also appear more "cleaned up", as is found with many other examples of conversion, where the degree of cyrstallinity tends to improve. No appreciable increase in the average thickness of the tubes could be found. While overall crystallinity improved, the tubes are still relatively disordered. Interestingly, rounded edge terminations, where two or more walls have coupled to form an end cap, are common in these samples, as is seen in the center of the right panel of Figure 5.15.

When higher power (3.5 kW and above) was used, the product, while turning completely white, also exhibited a larger degree of morphological changes. Figure 5.16 shows two TEM images from such a sample. While some tubes with well-defined wall structure remain, many of them have unraveled into nanoribbons and nanocyrstallites. Also evident was the formation of large, micron-scale crystallites that appear from their degree of contrast to be much thicker.

Higher temperature treatments also tended to result in onion-like BN particles, which can be seen in right panel of Figure 5.16. Figure 5.17 shows high magnification TEM images of one such structure, measuring about 50 nm across. The walls of the onion are composed of about 25 atomic layers. Similar structures have been reported in previous studies of MWCNT conversion [64], and were also observed in the conversion of graphene aerogels, particularly when excess boron oxide was used.

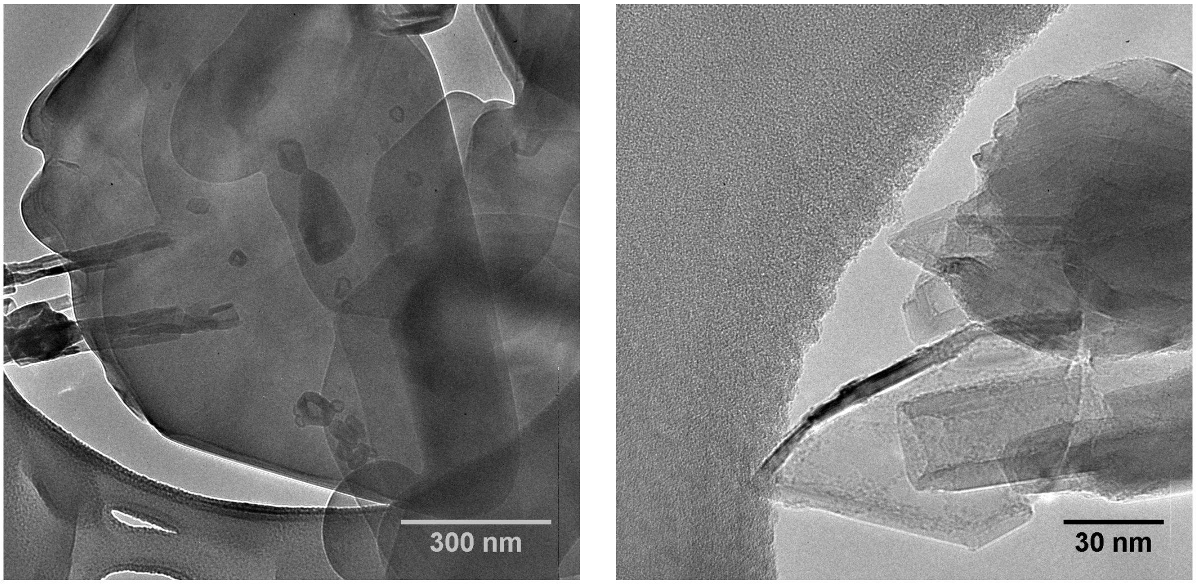

Figure 5.16: TEM images of multi-walled carbon nanotubes converted at high temperature. Tubes tend to unravel and also form larger plate-like structures, as well as onions.

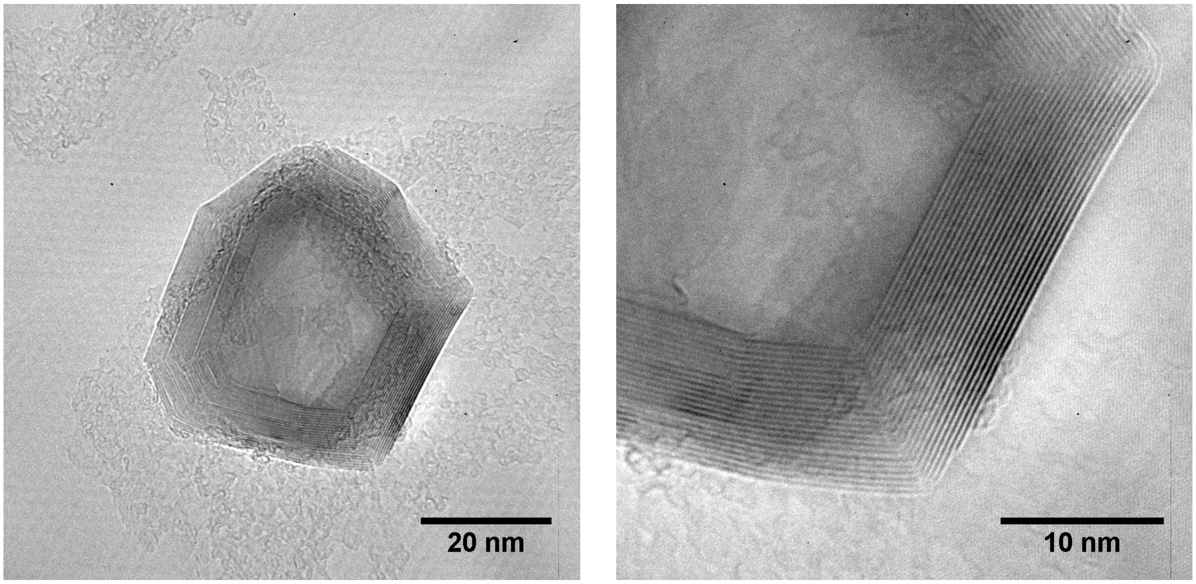

Figure 5.17: TEM images of onion particles formed in the high temperature conversion of multi-walled carbon nanotubes to boron nitride.

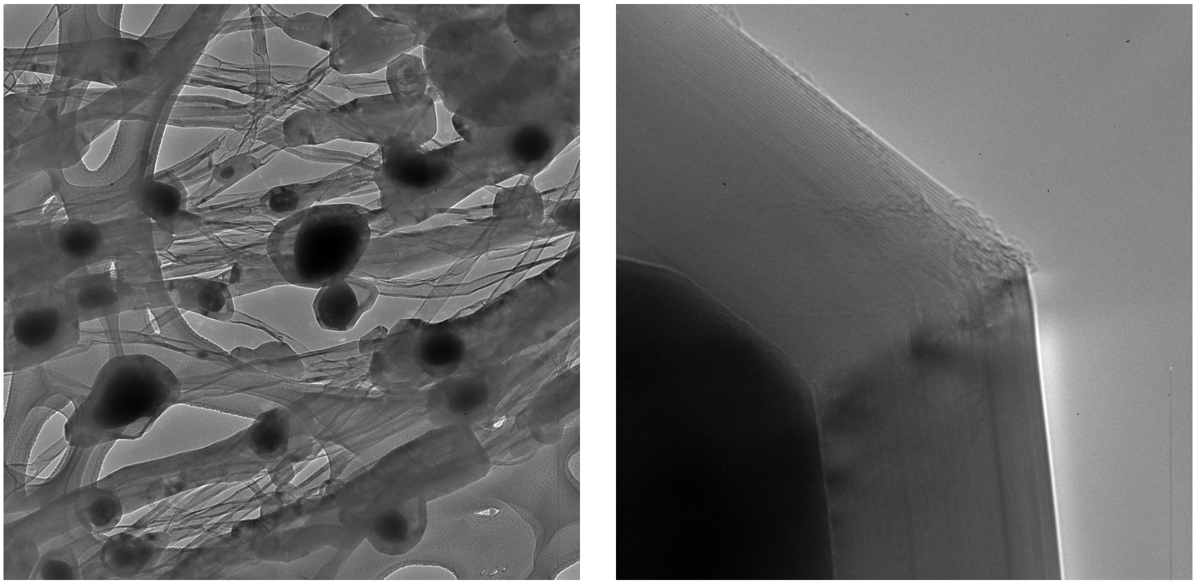

Figure 5.18: TEM images of converted ferrocene-derived multi-walled carbon nanotubes.

Ferrocene-Derived Multiwalled Tubes

Conversion was also attempted on ferrocene-derived MWCNTs. Such tubes are characterized by inclusion of iron nanoparticles in their interiors. Similar tubes derived from nickelocene or cobaltecene contain nickel and cobalt particles, respectively. Some interesting work was done in our group in the past by K. Jensen, who shows that by running a current through the tubes, the iron can be made mobile; in the process, carbon is dissolved in the particle and can precipitate out as a newly-formed nanotube, often improving the crystallinity of the starting material.[59]

Conversion of such tubes effectively encapsulates the iron particles in an inert, insulating sheath of BN. It was found that, in order to preserve tube morphology, lower temperatures were advantageous, and tended to result in well-defined wall structures. Microscopically, the resulting material was greyish. Interestingly, the grey color remained after baking out in air at 750 °C for one hour, while a control sample of completely unconverted tubes burned completely in that time. The sample did acquire a slightly reddish tint, presumably from the oxidation of some of the iron.

Figure 5.18 shows TEM images of the converted material after bake-out. By all appearances, it resembles closely the untreated nanotubes. The outer walls are in remarkably good shape despite the high temperature oxidation treatment. In some small details it differs from the untreated nanotubes, such as the increased presence of angular edges detailed in the right panel, which as discussed above, are more common in BN-based as compared to carbon-based nano-materials.

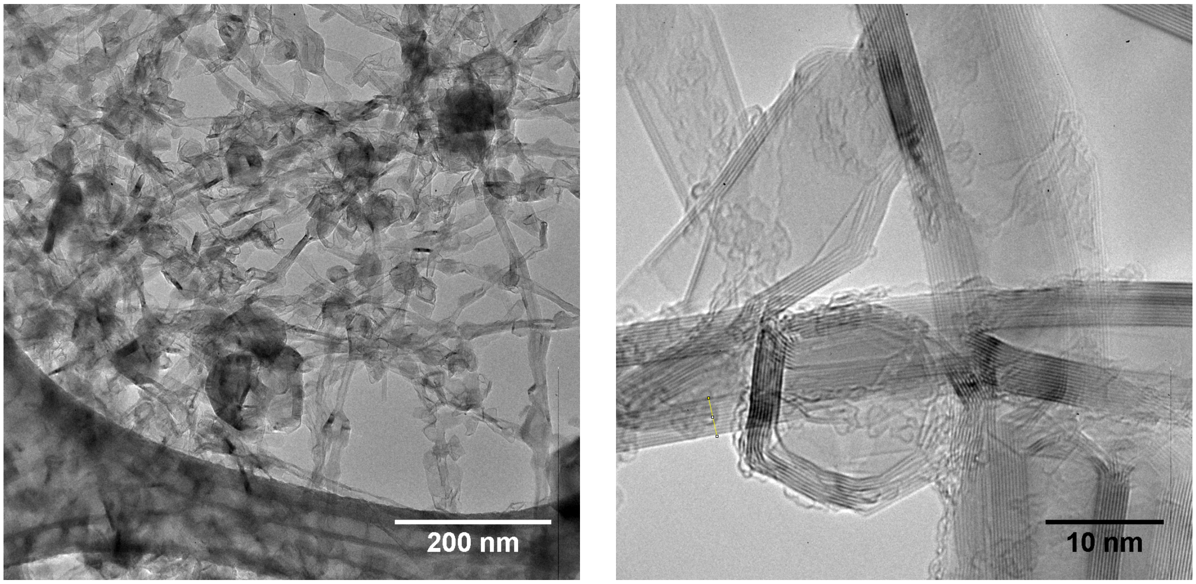

Figure 5.19: TEM images of a BN nanotube aerogel synthesized by conversion of a carbon nanotube aerogel.

5.6 Conversion of carbon nanotube aerogels

The success with converting graphene aerogels and the observation that sample homogeneity and arrangement tended to facilitate carbon nanotube conversion suggested that conversion of carbon nanotube aerogels would prove fruitful.

Carbon nanotube aerogels were provided by Dr. Worsley from Lawrence Livermore National Laboratory in the form of a large, monolithic cylinder, about 2 cm in diameter by approximately 5 cm tall. They were synthesized from highly purified carboxylated tubes using formaldehyde and resorcinol as gelling agents; sodium carbonate was used as a catalyst. [77] After gellation in water, they were super-critically dried and pyrolized in nitrogen at 1050 °C, resulting in a conductive carbon “glue” which coated the nanotubes and reinforces inter-tube cross-links. Microscopically, the material was ”squishy”: highly elastic and robust against large deformations.

A small section was cut from this cylinder, and together with Thang Pham, the conversion was run on the sample. 5 g of boron oxide was used under a flow of 1500 sccm nitrogen; induction power was high, at around 4 kW. The process was run for 30 minutes. The resulting gel converted completely and uniformly, to an off-white color. Mechanical properties were robust. Quantitative assessment was not undertaken, however on a qualitative basis, the original texture and elasticity of the carbon aerogel was preserved, as well as the overall morphology of the individual pieces.

Figure 5.19 shows two TEM images of the resulting aerogel. Sample were prepared by briefly sonicating the converted aerogel in isopropanol and dropping it onto a copper mesh TEM grid coated in lacey carbon. As with the many other examples of converted carbons in this chapter, the BN aerogels have a "cleaned up" morphology in comparison to the carbon nanotube aerogel precursors; compare for example to Figures 1c and 1d in Reference [77]. Tubes were around 10 nm in diameter and of fairly good crystallinity. Whereas before the conversion, individual tube wall could not be made out owing to the carbon "glue" coating, the walls and atomic layers of the BN converted gel were easily resolved. It appears that much of the original amorphous carbon was crystallized in the process of conversion; similar effects have been reported in conversion of multiwalled carbon nanotube powders as well as other forms of nanostructured carbon. Also, round particles, about 15 - 20 nm in diameter, which were visible in the precursor gel, also appear to have reformed, sometimes into large, hexagonally faceted nano-crystallites.

5.7 Surface conversion of Highly Oriented Pyrolytic Graphite

Highly-oriented pyrolytic graphite, or HOPG, is a fascinating material which is used extensively in research and industry as a calibration standard, owing to its high degree of crystalline order and neutral electronic surface. It can be easily cleaved with a piece of Scotch tape to reveal clean, flat planes of graphite. The orientation of the graphitic planes of high quality HOPG vary by less than 0.5 °.

Converting the surface of HOPG to BN would confer interesting advantages. BN forms, for example, an ideal surface of graphene-based electronics.[78] The mobility of electrons of in graphene resting on atomically flat BN substrates have been shown to rival those of suspended devices. The slight lattice mismatching between graphene and BN also introduces a superlattice structure; if orientation angle is controlled carefully, this could lead to interesting electronic effects.[79]

Growth of BN thin films on substrates was extensively pursued in the 1980's.[38] These processes generally involved dangerous precursors such as diborane or boron halides, making these approaches difficult in our lab. Recently, a new chemical vapor deposition (CVD) technique has been developed where thin layers of BN are grown on copper using borazine or ammonia borane as a precursor gas.[80] Here, I explore another approach, where the top layers of HOPG are converted to BN *via* carbothermal reduction.

The basic procedure is similar to those outlined above. HOPG in the form or small disks (3 mm diameter, SPI 425HP-CA) or 5 mm x 5mm x 1 mm squares (SPI 479HP-AB) were loaded into the induction furnace along with boron oxide using a custom-built stage, where the conversion cup was replaced with a graphite disk with some holes in it to hold the sample. The power to the induction furnace was varied from run to run, between 2 kW and 5 kW.

Figure 5.20 shows two low-magnification optical images of the HOPG disks. The image

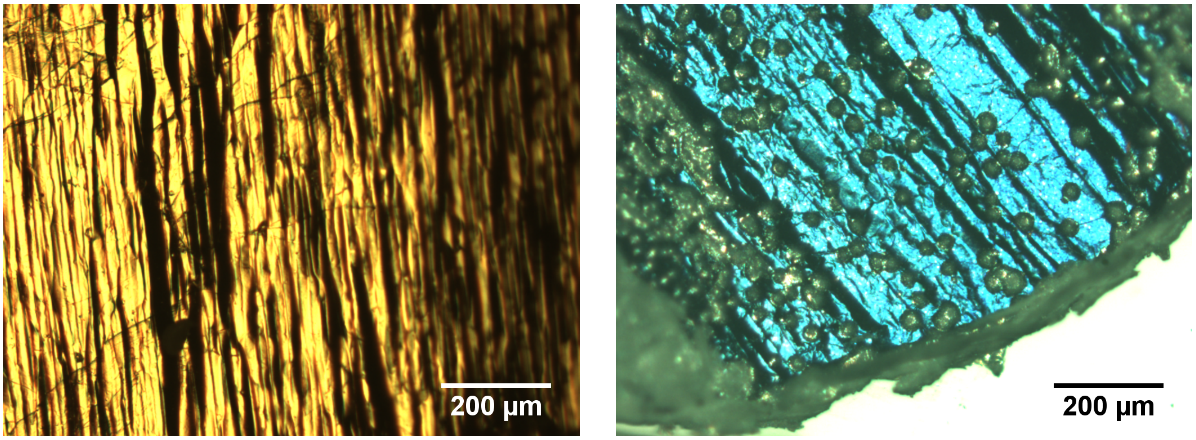

Figure 5.20: Optical micrographs of an untreated HOPG 3 mm disk (left) and one subjected to high temperature BN conversion (right).

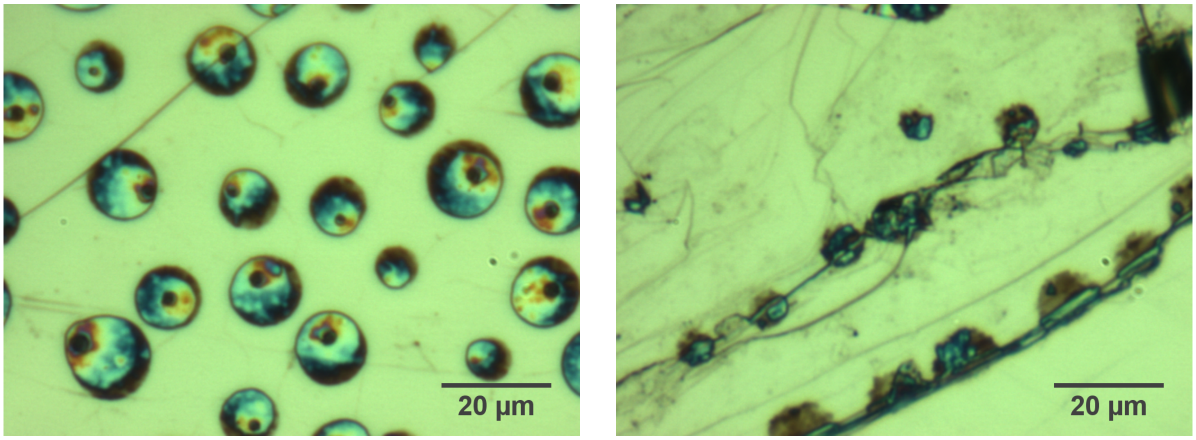

Figure 5.21: High magnification optical micrographs of HOPG 3 mm disks subjected to lower temperature BN conversion.

on the left is the original disk, and that on right has been converted at around 5 kW. A dramatic change int he surface properties is evident. The blue sheen on the surface was confirmed to be BN *via* EDS. Parts of the disk also turned a flaky white color. Pock-marks were also evident.

This experiment demonstrated that surface conversion on HOPG was possible. However, the sample was badly damaged, and it was desirable to see if a thinner layer of BN could be synthesized *via* this method. Figure 5.21 shows two high-magnification optical images of similar disks subjected to lower power conversion, at around 3 kW. The bluish areas are not concentrated in small pock-marks, as shown on the image on the left. The varying colors seem to indicate a varying depth of BN conversion; if due to a simple thin-film interference effect, the thickness of the layer would be around 100 - 200 nm. It is unknown if the flat surface was also converted; EDS did not indicate a strong BN signal, but would not be expected to for few-layer samples. In the image on the right, some step edges in the HOPG are seen where the conversion takes hold more readily.

Figure 5.22 shows two SEM images of a 5 mm square HOPG sample which has been subjected to low power conversion (about 3 kW). The sample was partly cleaved prior to insertion into the microscope to expose fresh graphite planes; an image of the edge of the cleft is shown in the top image. The difference in contrast in indicative of a chemical change on the surface of the HOPG, with the more insulating surface lighting up brighter due to charging effects. Again, EDS measurements did not clearly indicate the presence of BN, but this may be due to the fact that the layer is exceptionally thin.

In the bottom image shows close-up of the (supposed) BN region. The crystalline grains on the surface of the HOPG appear in high contrast; similar grains can be seen on freshly cleaved HOPG, though the contrast between the grains is considerably less. Streaks and cracks also appear on the grains which are not generally present on freshly cleaved HOPG samples.

Suggestions for Further Research

Refining this process was somewhat difficult, as the high and uncontrolled temperatures in the induction furnace make turning of the synthesis parameters difficult. Moving forward, it would be advantageous to attempt this conversion in the more controlled environment of a horizontal resistance furnace. HOPG itself can also be joule-heated, so it may be possible to simply put boron oxide on its surface and heat it in a controlled nitrogen environment. Making clean samples of thin BN on HOPG might offer an exciting and useful platform for further studies of the electronic properties of BN/graphene electronics and heterostructures.

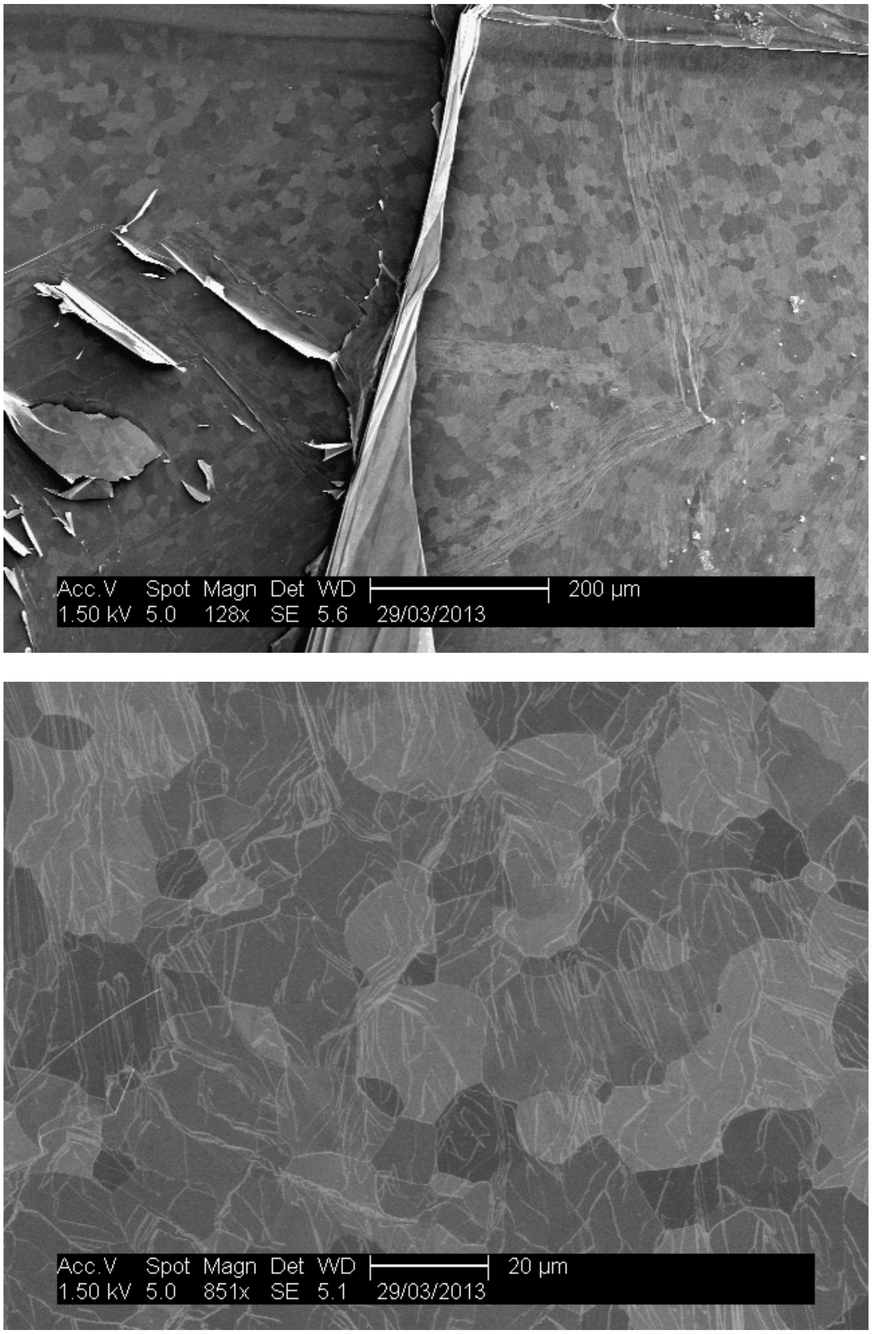

Figure 5.22: Scanning electron micrographs of BN converted HOPG. (left) border between a freshly cleaved port on the left hand side, and a converted section on the right. (right) converted section, showing granular patches about 20 microns in diameter.

Chapter 6

Boron Nitride Nanotubes *via* Nitridation of Boron Droplets

The simplest imaginable approach to BN synthesis is through the direct combination of boron with nitrogen. In the presence of nitrogen, the reaction proceeds nominally according to

$$2\,\mathrm{B} + \mathrm{N}_2 \longrightarrow 2\,\mathrm{BN} \tag{6.1}$$

This synthesis path was first reported by Moissan in 1892.[61] This reaction can proceed even when boron is in its solid phase, at temperatures exceeding 1200 °C. This chemistry is often employed in the high-temperature synthesis of boron nitride nanotubes (see discussion below). Even before this discovery it was found by Wöhler and Sainte-Clare Deville in 1857 that ammonia may be used as the nitrogen source.[61]

$$2\,\mathrm{B} + 2\,\mathrm{NH}_3 \longrightarrow 2\,\mathrm{BN} + 3\,\mathrm{H}_2 \tag{6.2}$$

Liquid boron is one of the most reactive substances known; for example, there is no known container for liquid boron and studies of this material must be conducted by levitating a droplet in a stream of noble gas while heating it with a laser.[81] I conducted some exploratory experiments using a high temperature induction furnace to melt boron in a graphite crucible, and found that the boron would actually melt *through* the graphite, forming a saturated boron carbide and continuing through the bottom of the crucible. Therefore, in order to form boron vapor and hence droplets, it is necessary to either ablate a stationary target, or to shoot powder through a hot zone.

We begin this chapter by discussing some previous methods for the synthesis of BNNTs via the boron droplet method; these involved the ablation of BN or boron targets with either an electrical arc or a laser. We then describe some attempts at synthesizing BNNTs by feeding boron powder through an electrical arc; these were unfortunately not successful. Finally, we describe a novel technique which was successful, which involved shooting boron powder through the hot zone of an induction furnace.

6.1 Previous Studies

Arc Ablation

Carbon nanotubes were first discovered in the residue of arc ablation experiments involving graphite electrodes, intended for the synthesis of fullerenes.[82] In the search for synthetic routes to BN nanotubes, the insulating nature of BN made this route problematic. As early as 1994, composite BCN nanotubes and sheets were synthesized by Stephan by filling carbon electrodes with amorphous boron;[83] we reproduce that experiment below in Section 6.2.

However, pure BN tubes remained elusive. The solution was to embed BN inside of a hollow tungsten electrode; this resulted in the first synthesis of pure BN nanotubes by Chopra.[84] This technique was further developed by Cumings using metal-doped boron electrodes, resulting in predominately double-walled BN nanotubes arranged in an intriguing web-like macrostructure.[85] The metal doping was necessary to increase the conductivity of the boron so that an arc could be established. Ablation in these experiments occurs at temperatures around 5000 °C, and it is believed that nanotubes condense from the resulting atomized vapors in various stages; droplet condensation is thought to play an important role.

A variation in this technique is to use a DC plama torch, and to shoot the reactant powders into the superheated gas.[86] This allows for continuous production and a much larger choice of solid precursors. The quality of the results, however, was not very good. I made some attempts at reproducing and modifying this method, which I describe below.

Laser Ablation

Laser ablation was initially used in the production of BN nanotubes by Golberg and Lee.[87, 88] The technique involves aiming a high-powered laser onto a BN target in an argon atmosphere, or a boron target in a nitrogen atmosphere. Recently, a group at NASA modified this technique by placing the target in a hyperbaric chamber operating at several atmospheres of nitrogen.[89] This resulted in relatively high yields of long, tangled BN nanotubes. Essential to this process was the condensation of boron droplets around a tungsten wire, which subsequently react with the nitrogen to form nanotubes. The high pressures not only increase the concentration of nitrogen and favors the precipitation of solids, but also provides a large buoyant force for the droplets.

The mechanism proposed by Arenal et al. in their study of BNNT synthesis via laser ablation is reproduced in Figure 6.1. The BN is thought to form on the surface of a boron droplet, and condense out as a tube as the droplet moves through the reactive nitrogen atmosphere in a root-growth mechanism. [90]

6.2 DC Arc Ablation of Boron

The DC arc chamber is a simple apparatus used for achieving very high temperatures in a controlled atmosphere. Figure 6.2 shows a schematic of the chamber and electrodes. It

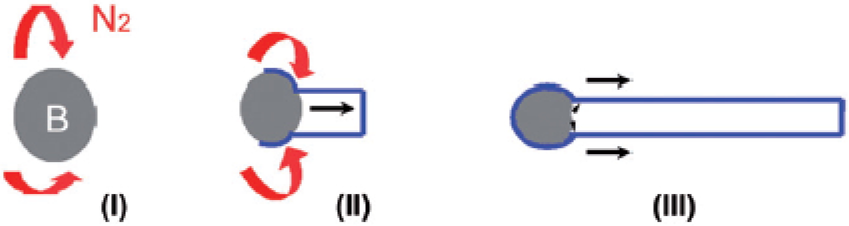

Figure 6.1: Proposed BNNT formation mechanism. Reproduced from Reference [90].

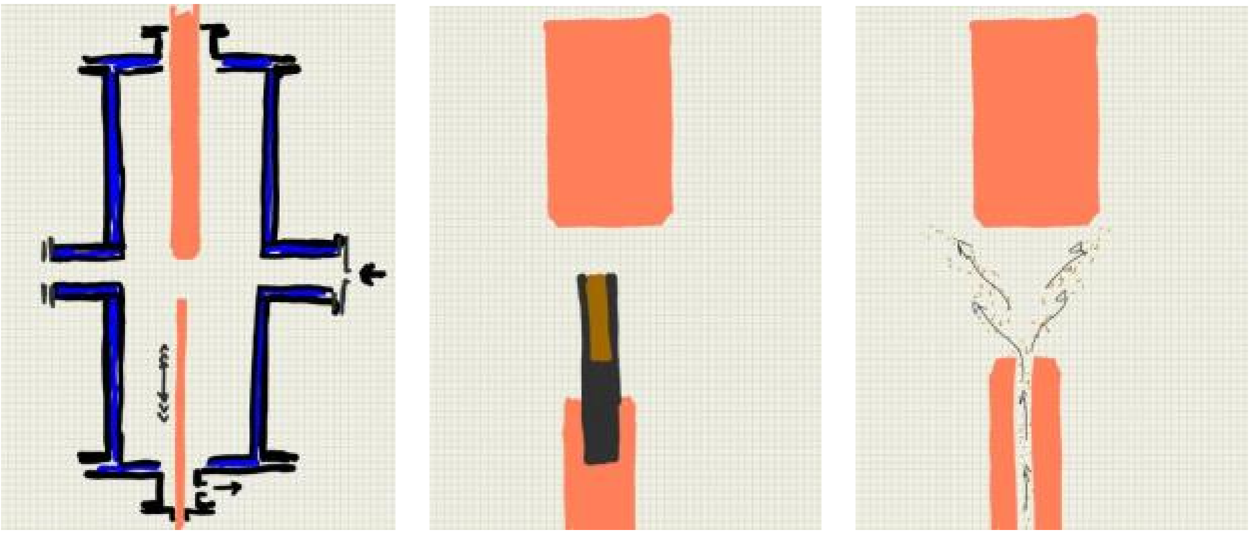

Figure 6.2: Schematics of DC arc apparati. (left) Schematic of arc chamber; black parts are steel, blue is water jacked, orange is copper electrodes, arrows indicate direction of motion of bottom electrode, both top and bottom electrodes are water-cooled. (center) Detail of boron-packed graphite electrode, dark grey is graphite, brown is amorphous boron powder, both electrodes are water-cooled. (right) Detail of powder-feeding electrode, arrows indicated flow of carrier gas, brown dots represent boron powder, both electrodes are water-cooled.

is composed of a water-cooled, 6” inner diameter by 24” tall cylindrical vessel with several “arms” jutting out in various directions. These arms provide ports for insertion of electrodes, viewing glasses and other peripherals.

Connections include both O-rings and copper flanges. Electrodes are introduced from the top and bottom of the chamber. The bottom electrode is attached to a stepper motor with a feed screw that allows it to be moved up and down at a controlled rate. Both electrodes are water cooled. Gas was introduced through one of the side ports, and let out through the bottom; a vacuum system was attached to the outlet as well, which had a throttle valve to control the pressure inside the chamber. The chamber was typically operated at around one-third of an atmosphere of nitrogen or helium.

Two designs were used for the bottom electrode. In the first case, for the attempted synthesis of BCN nanotubes, a 0.250” diameter graphite tip was drilled with a 0.187” hole and packed with amorphous boron powder. This was attached to the bottom electrode via a small notch at the top, as shown in the center of Figure 6.2. This design proved stable and reliable; results are presented below.

In the right panel of Figure 6.2 we show an alternate design, where amorphous powder was fed continuously through a specially built electrode which consisted of three concentric copper tubes: an exterior jacket (0.250” outer diameter), a water return tube (not shown), and a powder bore (0.125” inner diameter) through which the powder was injected. The large bore was selected to keep the powder from clogging inside the electrode. The electrode was hard-soldered together. This design proved very problematic, as the solder often leaked. Furthermore, it was very difficult to sustain a stable arc. Even when an arc was maintained, the cold gas flowing through the center bore tended to repel the hot plasma, meaning that none of the injected powder would actually run through the superheated parts and melt. For this reason, no results were obtained using this device.

In both cases, the power to the electrodes was supplied through a commercial welding powder supply operating at around 150 amps. For the powder feeding setups, the powder was fed using a commercial Mark XV powder feeder; more information is available at http://powderfeed.net/MARKXVspecs.html.

Procedure

The chamber was evacuated and flushed three times with nitrogen; it was stabilized at about 10 bar. Next, the power supply was struck and the electrodes touched and separated slightly. It was very difficult to maintain a stable arc. The boron filling at the end of the electrode quickly melted and formed a liquid ball which usually hung to the side of the electrode. It is likely that it contained a significant fraction of carbon as well. The arcing continued for about one minute, after which the ball of liquid boron/carbon was gone, having been used up or fallen off to the side of the electrodes.

After the system was allowed to cool somewhat, the chamber was opened. A large amount over very low-density material coated the water-cooled walls of the chamber. Care had to be taken to prevent this material from becoming airborne. It was collected with a spatula into

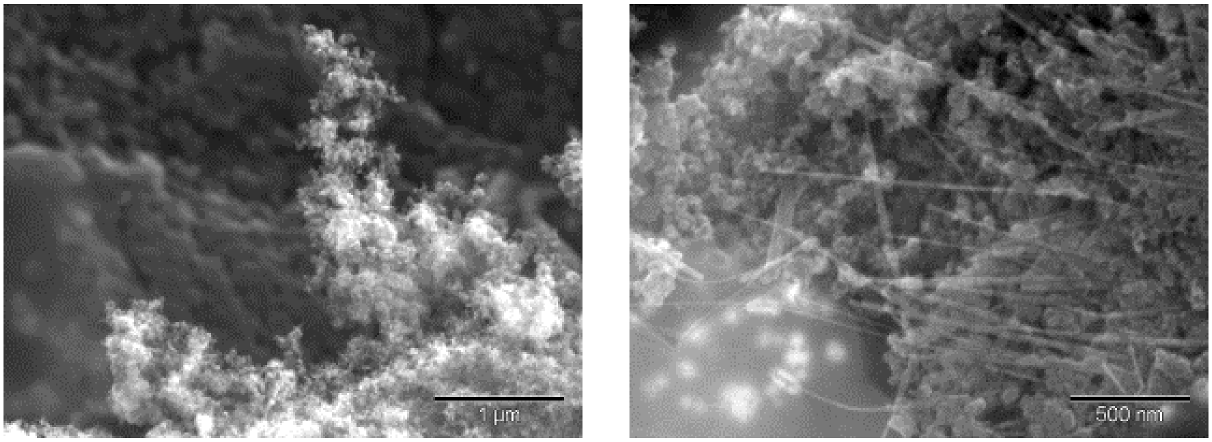

Figure 6.3: SEM images of boron arc material.

glass vials. It had a brownish-black appearance, and tended to form in needle-like, dendritic structures.

Results

Figure 6.3 shows two SEM images of the resulting material. The low density of the material can be understood from the fractal-like microstructure. The material consists mostly of rounded particles that are likely composed of boron carbide. Linear features several microns long and several tens of nanometers wide can be seen in the image on the right.

TEM images of the same material are shown in Figure 6.4. The low magnification image on the left shows both the ball-like material and a pair of tubes that are mixed in. The material has been sonicated in IPA for 1 min in order to prepare the TEM sample. Small round balls about 50 nm in diameter show up in high contrast; these may be composed of copper which has ablated off of the counter-electrode. The smaller, lower contrast balls are likely some form of boron or boron-carbide. The two linear feature are fond to be multiwalled nanotubes, about 20 – 30 nm in diameter, and consisting of about 15 – 20 walls; a detail is shown on the right.

Suggestions for Research

This line of research is worth pursing, as the arc ablation approach is the only known way to make consistently high quality double-walled BNNTs. Our electrode makeup, however, was rather difficult to work with, and hard to make consistent. Moreover, carefully tuning the carbon composition through the electrodes may offer an approach to BCN stoichiometry.

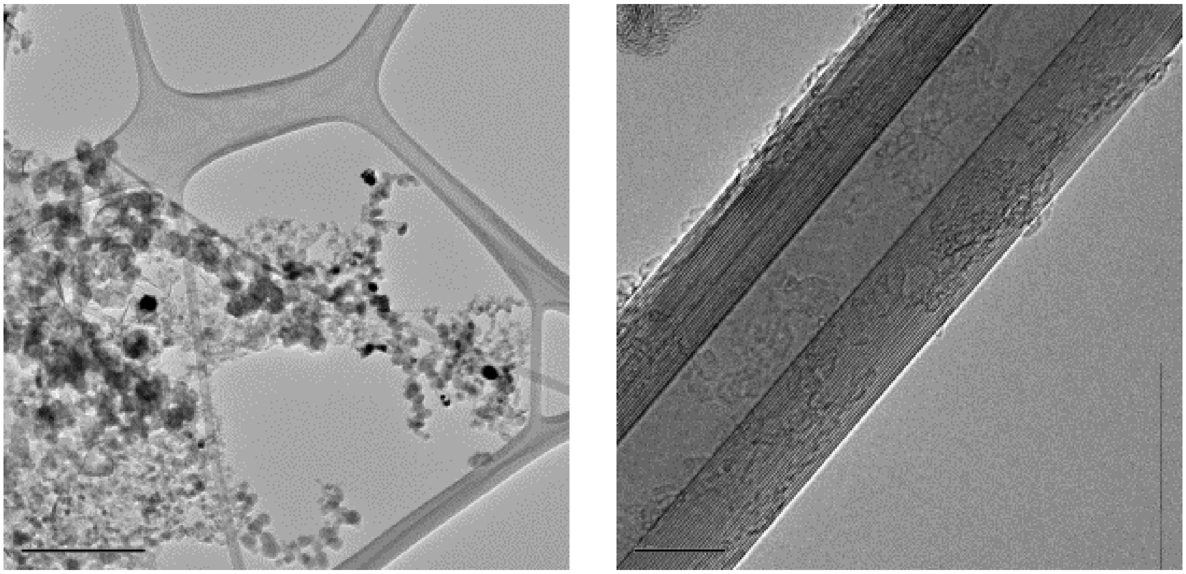

Figure 6.4: TEM images of boron arc material. Scale bars are 500 nm (left) and 10 nm (right). Images by W. Mickelson.

Pure Boron, Heated Electrodes

One way to improve these results might be to use heated, pure boron electrodes. The work of Cumings[85] was very similar to this approach where the boron electrodes were doped with metals to increase their conductivity. The drawback of this approach was that the ingots were hard and expensive to make, and were irregularly shaped and impossible to machine, meaning that the voltages required to sustain the arc varied greatly. On the other hand, the electrical conductivity of pure boron is highly dependent of temperature. Instead of metal doping, the electrodes could instead be pre-heated, allowing them to sustain an arc. This would also allow for use of commercially available boron sources, greatly reducing the cost.

Hyperbaric Chamber

Another approach for improvement may be to allow for hyperbaric operation. As mentioned above, increased pressure has been shown to be advantageous in the laser ablation approach and may also benefit the arc-ablation approach. Such chambers would be easy to build and operate safety, and would be much cheaper to use and maintain than laser ablation systems. Additionally, increased pressures would lead to improved arc stability, and possibly allow for a wider range of current and voltage settings.

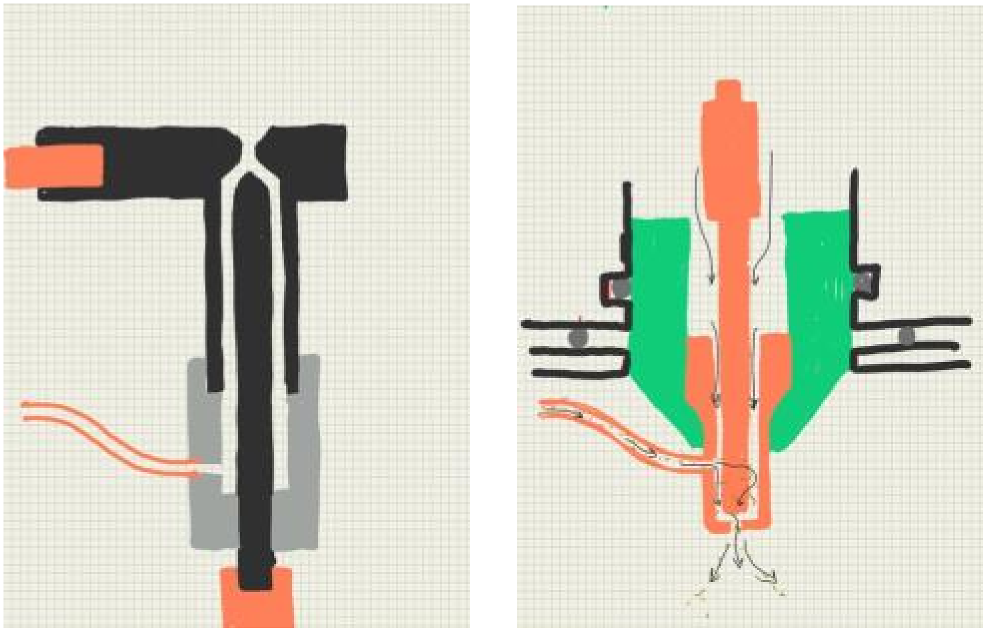

Figure 6.5: Schematics of DC plasma torches. (left) custom-built torch, dark grey is graphite, light grey is BN, orange is copper, electrodes are water-cooled (right) adapated commercial plasma cutter, light green is plastic, light grey circles are O-rings, black outline is connector and top of arc chamber

6.3 Powder Injection into a DC Plasma Torch

Owing to the difficulties in getting boron powder to melt in an open arc, an alternate design was developed using a DC arc torch. These are used commonly in plasma spray systems, where oxide powders are heated in a stream of superheated gas and sprayed onto various substrates, forming protective coatings. The reactivity of liquid boron, however, may render such systems unsuitable for synthesis. To get around these problems, I custom-designed and built two DC arc torches, described below. A similar approach has been reported in literature.[86]

In the first instance, I built the torch myself from scratch by machining graphite and boron nitride parts, shown schematically in the left panel of Figure 6.5. The assembly was mounted inside of the arc chamber described above using one side port and one bottom port for the electrodes. The bottom electrode (anode) was mounted with a 0.250” diameter graphite rod, and the cathode had a 0.375 inch inner diameter. A 0.125 inch copper tube was intended to inject powder through the assembly.

There were several issues with this design, namely that ignition was difficult to attain and thermal stresses often caused the parts to crack. The plasma plume was also rather unstable. Typically, about 150 amps were run through the device using a commercial welding power supply. The device would heat up to a bright white glow relatively quickly. This prevented

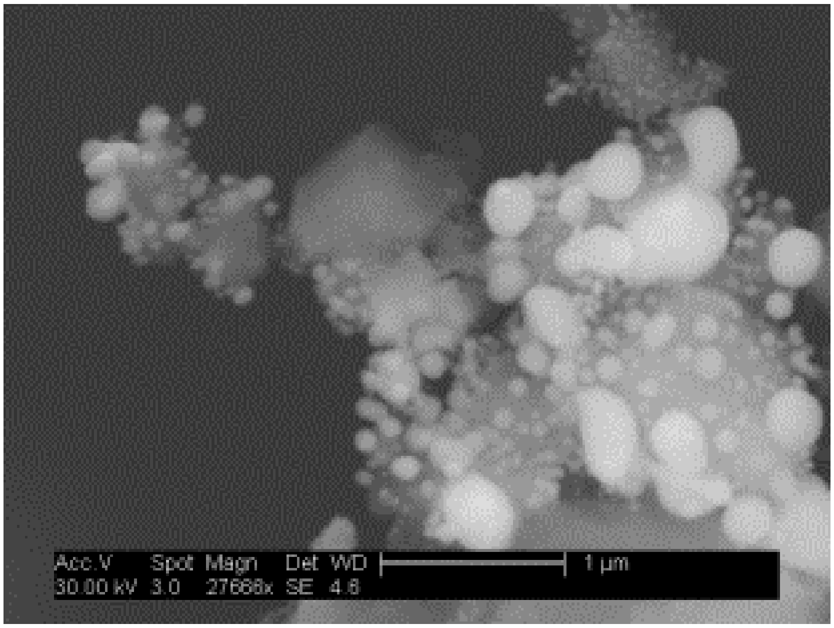

Figure 6.6: Product from adaptation of commercial plasma cutter.

me from conducting many experiments feeding powder with this design.

To deal with some of these problems, I decided to try modifying a commercial 20 amp plasma cutter system. A schematic of the design is shown in the right panel of Figure 6.5. A small hole was drilled into the side of the counter-electrode in order to allow for powder feeding. The plastic housing of the torch was set into to a vacuum fitting and mounted to the top port of the arc chamber. This tended to disturb the plume significantly, particularly when carrier gas flow rates through this hole were high, but the plume was still stable enough to conduct experiments.

Results

Despite considerable effort and time spent, these experiments unfortunately did not result in synthesis of any BN nanotubes. I was however able to melt some powder using the adaptation of the commercial plasma cutter. An SEM image of the product is shown in Figure 6.6. The elemental composition is uncertain, and it may be that the particles come from ablation of the electrodes.

6.4 Powder Injection into an Induction Furnace

By far the most successful synthesis of BNNTs was obtained via the direct injection of boron powder into an inductively heated graphite cylinder. The induction heating was performed in the furnace described in the previous chapter using the same basic quartz and flange system.

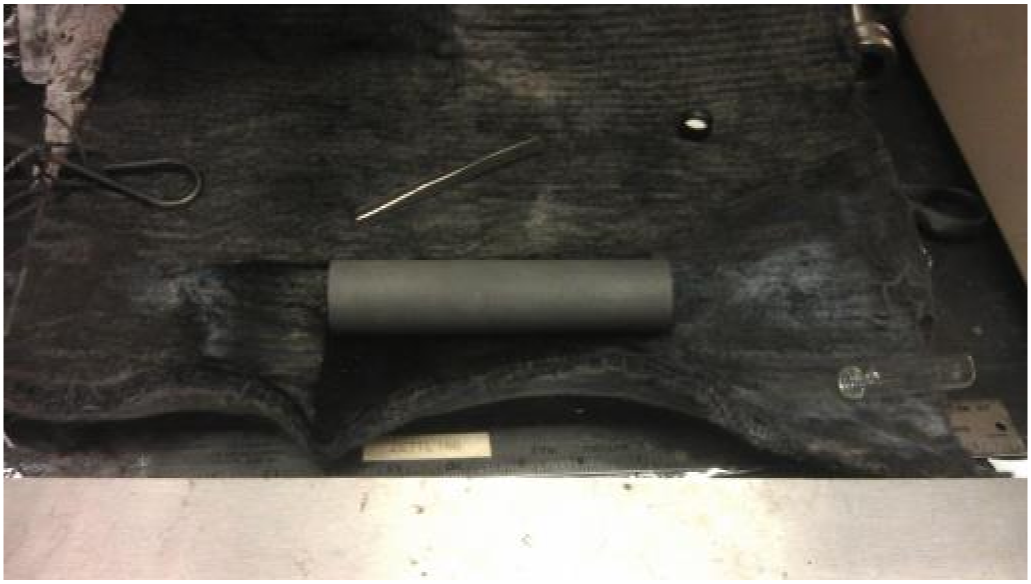

Figure 6.7: Photograph of graphite cylinder with insulation used for BNNT synthesis.

I describe below the adaptations of the setup specific to this experiment. The suggestion to shoot powder through the induction furnace was given to me by Dr. William Mickelson.

Apparatus

The arrangement of the graphite cylinder and the insulation is shown in Figure 6.7. A 1" diameter by 7" long graphite cylinder is simply wrapped in a blanket of insulation, and inserted snugly into the quartz tube of the induction furnace. A schematic of the arrangement is shown in Figure 6.8. In this setup, I used Kreca pitch-based carbon fiber insulation. In some runs, carbon yarn was used to tie the insulation snugly around the cylinder. In some runs, a BN tube was used to guide powder from the alumina injection tube up towards the graphite cylinder; however, this tended to result in lower temperatures, as the BN tube would also act as a heat conductor.

Powder was fed *via* an alumina tube coming in through the bottom flange of the induction furnace; the exhaust came out the top. I also attempted an inversion of the setup according to a suggestion by Prof. Zettl, where the powder was fed from the top and the exhaust came out the bottom. Similar results were obtained using both configurations.

Procedure

If the setup had not been used for a while, an argon flow would be introduced and the chamber pumped down to about 10 kPa while being heated at around 1 kW; this would cause adsorbed water to boil off and eventually evaporate. After all the water was dried

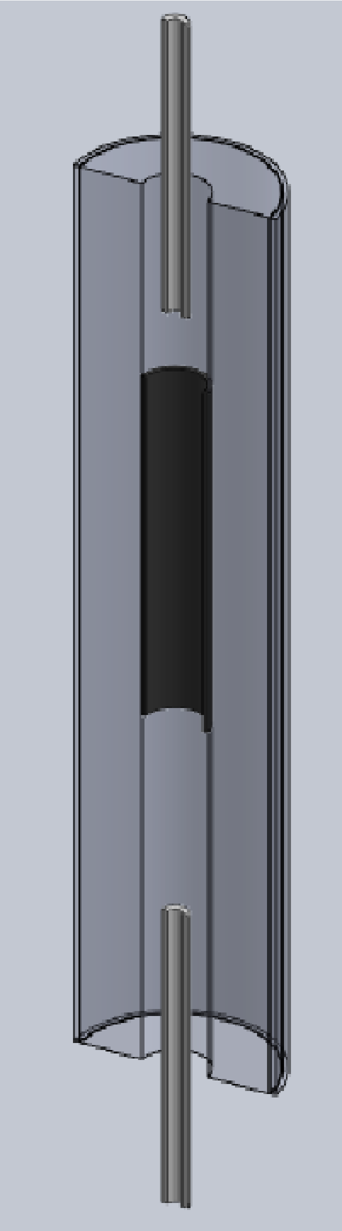

Figure 6.8: Schematic of graphite cylinder with quartz tube and inlets used for BNNT synthesis.

(about 20 minutes), the setup is then heated rapidly at the maximum available power given our load, about 7 kW. The estimated temperature at the center of the graphite cylinder is in excess of 2000 °C. Again, temperatures in the induction furnace are hard to determine accurately; in this case, it was important that all parts be covered in insulation, so that even optical pyrometry was not possible. The estimated temperature is deduced from the fact that the boron became liquid, and that even alumina parts far from the center of the hot zone would occasionally melt.

Powder is injected from the bottom at a rate of about 100 mg/min, with a carrier gas flow of argon at around 2000 sccm, and ammonia is injected from the top at around 1500 sccm. In principle, it should be possible to use diatomic nitrogen as the reactive source; however, we found that yields tended to be very low in this case. This may be different if higher pressures or temperatures could be achieved.

Results

After a run of about one minute, the cylinder was allowed to cool under nitrogen flow and was removed along with the insulation and unwrapped. In successful runs, a white substance would coat the insulation on the downstream end of the graphite cylinder. Figure 6.9 shows two photographs of the setup after it has been removed and unwrapped. Depending on the flow of carrier gas, the white substance formed either directly above the cylinder or further downstream which was found to contain a large concentration of BNNTs (see below). Higher quality material tended to be collected when the material would condense about 3 cm from the end of the cylinder. It was also possible to stuff additional insulation into the setup downstream from the cylinder to provide more places for the nanotubes to condense.

The tubes were invariably deposited on the carbon fibers of the insulation. The fibers were examined in an optical microscope; a typical result is shown in Figure 6.10. An iridescent, crystal-like material covers the carbon fibers, and has small black dots, from 0.5 to 2 microns in diameter, embedded in it.

Figure 6.11 shows a series of SEM images of the white product collected from the insulation. In the upper left, we see an insulation fiber which has been covered completely in fibers, which appear to grow like fur on its surface. It is likely that the fiber acts as a condensation point for the boron vapor that passes by it; the low temperature wake of the fiber causes small boron droplets to form, which in turn react with the ammonia atmosphere to form BN nanotubes. Another detail of the mat of tubes is shown in the upper right panel.

The lower panels show higher magnification images of the tube mats. Round particles, presumably of boron, are found at the tips of tubes which jut out from the central fiber from which they appear to condense. Larger boron particles are also present, indicating that perhaps these simply get caught up in the tube mats; they may also play a role in the tube formation process. It is evident in these images that the tubes are approximately 50 microns long.

Figure 6.12 shows additional high-magnification SEM images of the BN product. The presence of small, round particles is ubiquitous. In many cases, they are seen decorating the

Figure 6.9: Photographs of BNNTs deposited the downstream end of the graphite tube.

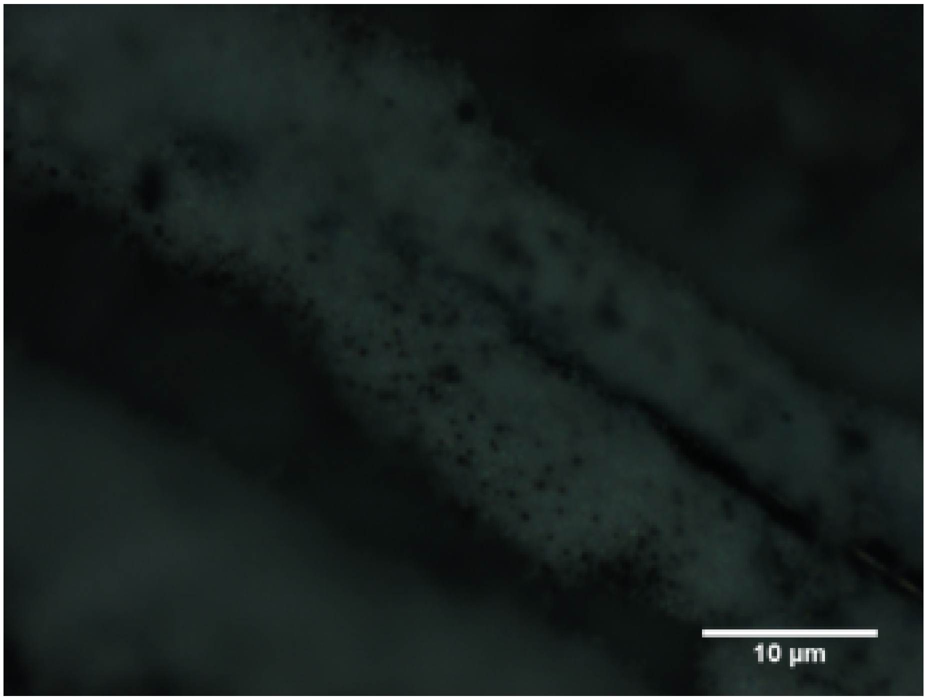

Figure 6.10: Optical microscope image of carbon fiber covered with BNNTs.

sides of the tubes, indicating that they adhered after tube formation. In other cases (lower right) they can be attached to the ends of the tubes, indicating that they may be the particle from which the tube formed.

The synthesis products were also examined in TEM. In order to avoid breaking the tubes, samples were prepared by rubbing a TEM grid covered in lacey carbon across the carbon fibers coated in BN nanotubes. Figure 6.13 shows low-magnification TEM images of the BN nanotubes. On the left, the first 20 microns of a 50 micron tube is shown. The tubes in this sample tended to have a tapered structure, starting with a thickness of about 100 nm and thinning out considerably as they went along. The start of one such tube is shown in the right panel. Contrast was much higher at this end, and there appeared to be a filling inside the tube, likely boron.

These images suggest the condensation mechanism proposed in a number of previous studies [91, 85] namely, that as the boron particle moves through the reactive environment (nitrogen or ammonia), it leaves behind a “tail” that forms a BN nanotube. The rate of formation may depend on the speed and size of the boron particle, but it appears in this case that a narrow tube may emanated from a larger particle, since the particle would presumably shrink as it moved along and gave off more and more boron. On the other hand, it may be the reduction in speed and/or temperature of the particle plays an important role in halting tube growth. The ambient vapor pressure of boron may also play an important role, in which case the particle could possibly grow rather than shrink as it moved further away from the

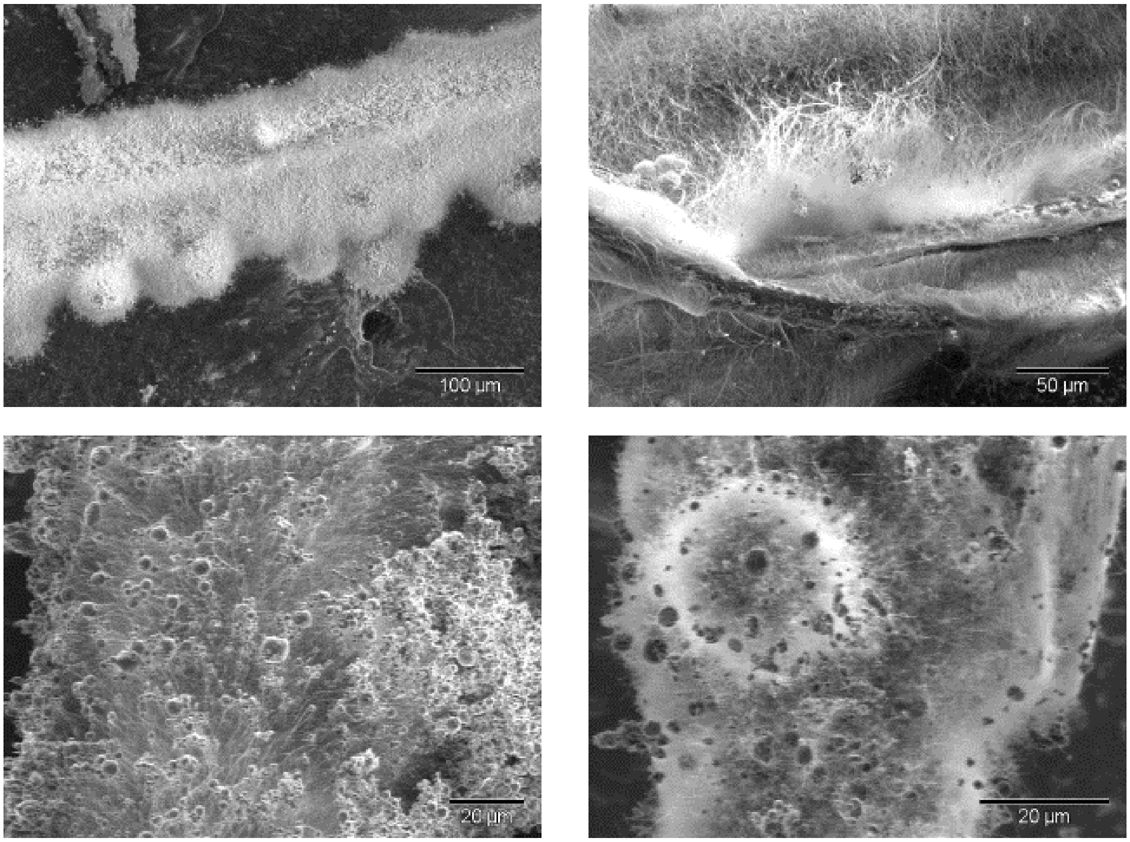

Figure 6.11: Low magnification SEM images of carbon fiber covered with BNNTs.

hot zone. Further studies and modeling are necessary to elucidate this process.

Figure 6.14 shows a series of high-magnification TEM images of the same nanotubes. The crystallinity of the tubes is good; the walls are composed of roughly 6 to 12 well-ordered concentric BN layers. In the upper panels, smaller boron particles of about 5 nm diameter are evident. In some cases, there are also hollow, presumably BN spheres, that may have formed through the nitridation of small boron particles.

The lower panels show two “clean” BN tubes. The dark fringes are typical of highly crystalline BN nanotubes, and may indicate a degree of internal stress and/or facets on the surface of the tube. The tubes are about 15 nm in diameter, and sometimes have a layer of amorphous material on their outsides.

Hyperbaric Operation

By attaching nuts to the threaded rods which support to top flange of the induction setup, it was possible to run the system at slightly elevated pressures. Safety concerns, however, limited our operation to around 2 atm. The tubes in this case tended to be slightly longer, and the sizes of the round particles slightly smaller. The elevated pressures also were advan-

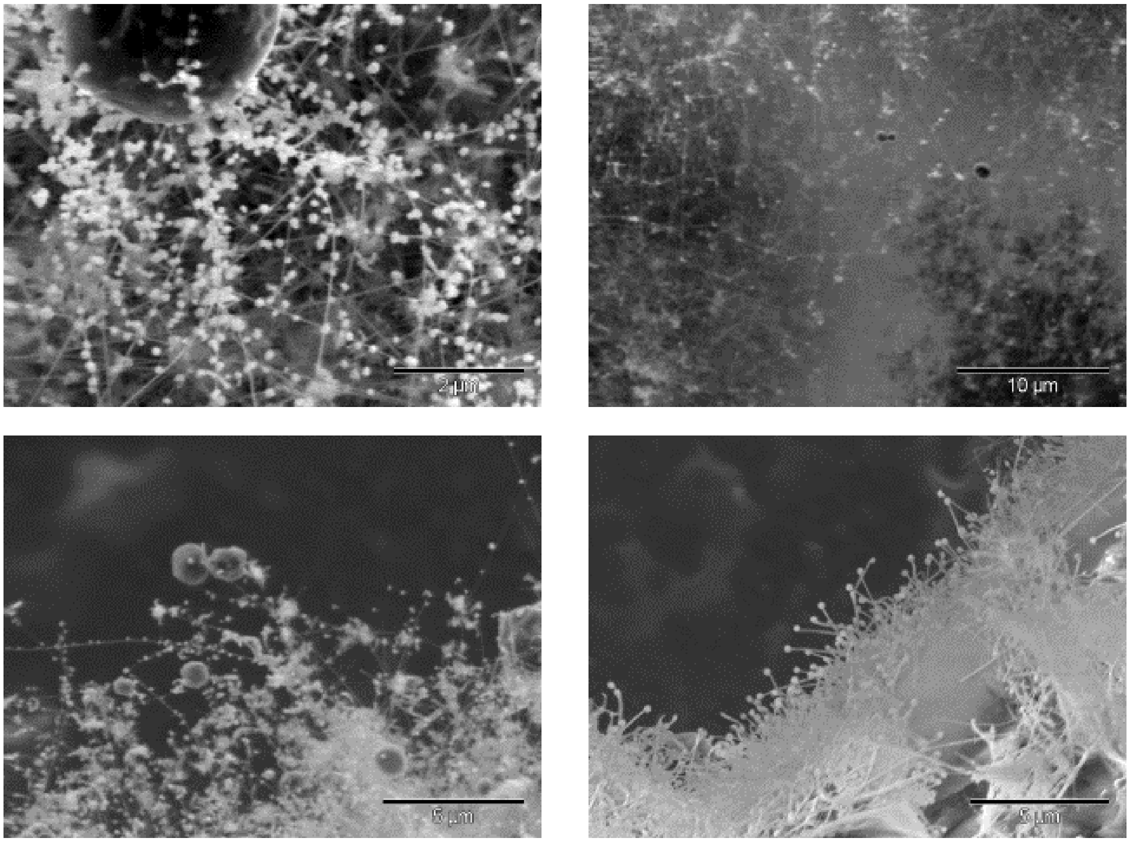

Figure 6.12: High magnification SEM images of BNNTs synthesized *via* powder injection into an induction furnace.

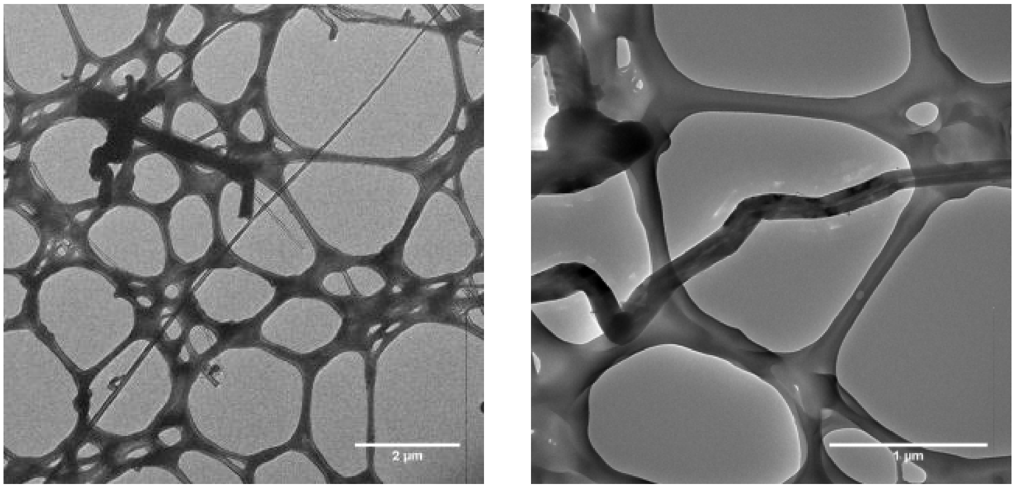

Figure 6.13: TEM images of BNNTs synthesized *via* powder injection into an induction furnace.

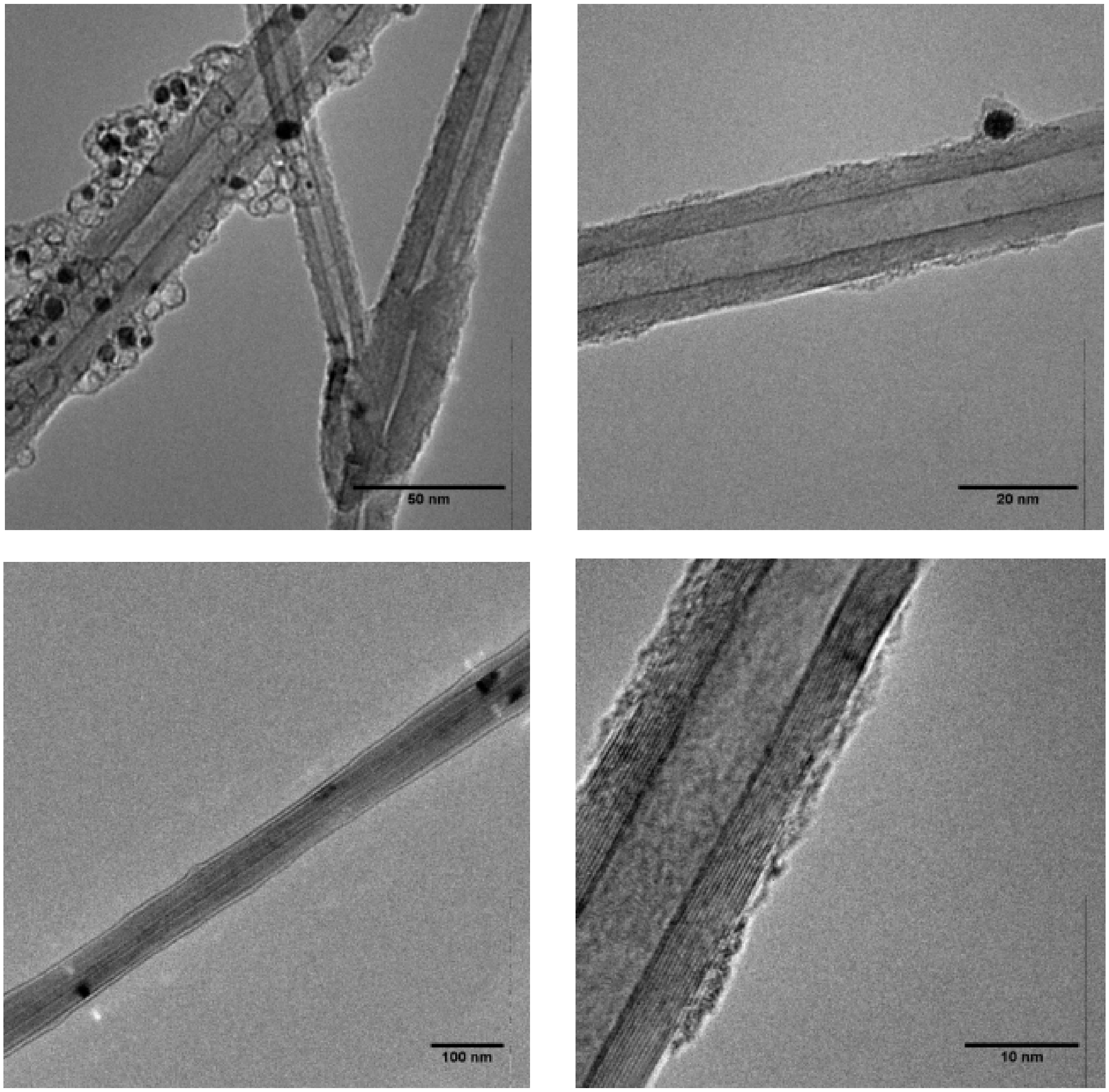

Figure 6.14: High magnification TEM images of BNNTs synthesized *via* powder injection into an induction furnace.

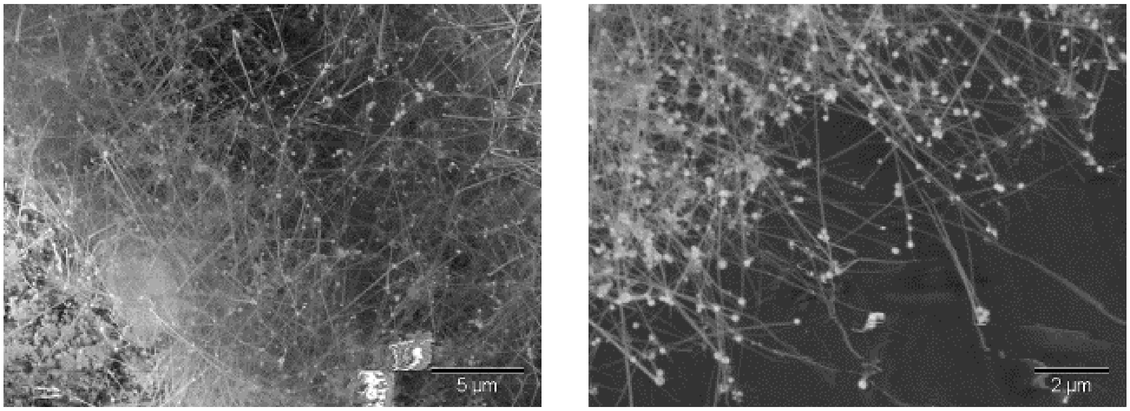

Figure 6.15: SEM images of BNNTs synthesized *via* powder injection into an induction furnace under hyperbaric pressures.

tageous for powder feeding, as the powder feeder tends not to clog up as much under these conditions. SEM image of some typical results are shown in Figure 6.15.

Suggestions for Improvement

As indicated above, elevated pressures tended to improve the quality and quantity of tubes. However, the quartz reaction chamber we use in our induction furnace limits the amount of pressure that can be applied safely. An alternative might be to enclose the system inside of a metal chamber with the induction coil inside; similar systems have been used in the past for attaining a combination of high temperatures and pressures in synthesis systems.

Additionally, the fibers on which the tubes form appear to be important in the tube formation process. It would be worthwhile to model the flow dynamics carefully, and consider the design of a condenser system which would facilitate tube growth. Such a system would also be useful if production were to scale up, making product collection more efficient.

Lastly, the length of the hot zone in the furnace likely plays an important role in the synthesis process. I believe that a longer zone might benefit tube formation by keeping the boron droplets hotter for longer. The hot zone could be tailored by use of longer, custom-designed susceptors, insulation, and a careful understanding of the convective flows inside of the chamber.

Chapter 7

Boron Nitride Nanotubes *via* Metal Oxides and Metal Borides

In this final chapter, we will look at another interesting route to the synthesis of boron nitride nanotubes, involving the nitrdation of boron synthesized *in situ via* the reduction of metal oxides or decomposition of metal borides. In the former case we will concentrate on the reaction of magnesium oxide with boron, which subsequently reacts with ammonia to form BN.

7.1 Metal Oxide Reduction by Boron

In this approach, a metal oxide undergoes a solid-solid reaction with boron at high temperatures. The approach was first reported by Tang and Bando [92] which they term the *BOCVD method*. In their experiment, boron powder and magnesium oxide in equal soichiometric amounts is mixed together in a mortar, and heated in a BN crucible under a stream of argon; the stream of reactive gas lets out into another BN crucible which is saturated with ammonia; upon mixing, BNNTs about 60 nm in diameter and several microns long can be collected by scarping a small amount of material off the side of the BN crucible in which the reaction takes place.

The chemistry of the reaction proposed by Tang and Bando is that the oxide forms a diboron-dioxide molecule, which subsequently reacts with the ammonia for form BN according to the reactions

$$2\,\mathrm{MgO} + 2\,\mathrm{B} \longrightarrow 2\,\mathrm{B_2O_2} + 2\,\mathrm{M} \tag{7.1}$$

$$\mathrm{B_2O_2} + 2\,\mathrm{NH_3} \longrightarrow 2\,\mathrm{BN} + 2\,\mathrm{H_2O} + \mathrm{H_2} \tag{7.2}$$

A good recent review of the BOCVD method can be found in Reference [93].

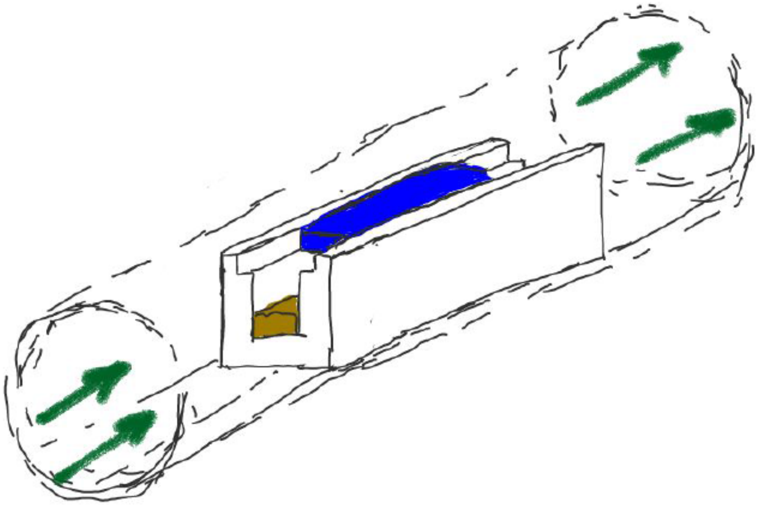

Figure 7.1: Schematic of silicon chip method for synthesis of BNNTs via BOCVD. White solid is BN; brownish material is MgO/B precursor powder; blue is silicon; green arrows indicate ammonia flow.

Silicon Chip Method

The method described by Tang and Bando uses an induction furnace. It is rather complicated setup, and not very reliable; many attempts were made at making a reliable crucible, but consistency was very hard to achieve. Drs. David Okawa and Shaul Aloni developed a very facile alternative setup for synthesis of BNNTs based on the BOCVD method. A schematic of the setup in shown in Figure 7.1. A open-faced boat is machined from 15 mm square stock of pyrolitc BN. The Mg/O powder is packed into the bottom of the boat, and a strip of silicon is cleaved to fit in a groove at the top of the boat. The assembly is placed in a 25 mm OD quartz tube, which is heated in a horizontal tube furnace to 1200 °C under a flow of argon. When the synthesis temperature is reached, the gas is switched to ammonia. The powders react and diffuse upward towards the chip. Gas flowing past the boat reacts in the region between the precursor powder and the silicon, and BNNTs grow on the surface of the chip. The reaction is run for about 15 minutes, after which the furnace is allowed to cool.

Upon removal, the chip is coated with a hard white substance which tends to be thicker along the upstream edge.Figure 7.2 shows an SEM image of the resulting chip. The white substance is composed of a hard layer of disordered magnesium oxide from the top of which BNNTs protrude. The tubes are about 10 - 50 microns long and approximately 50 -60 nm wide. TEM images (not shown) show good crystallinity, though significant amounts of magnesium oxide contaminants tend to be present. The diameter and degree of magnesium oxide contaminants vary along the chip, and it is important to examine the sample in the SEM to find the best quality tubes. The method is very reliable, and almost always results in some good tubes which can be useful in single-tube experiments if they can be properly

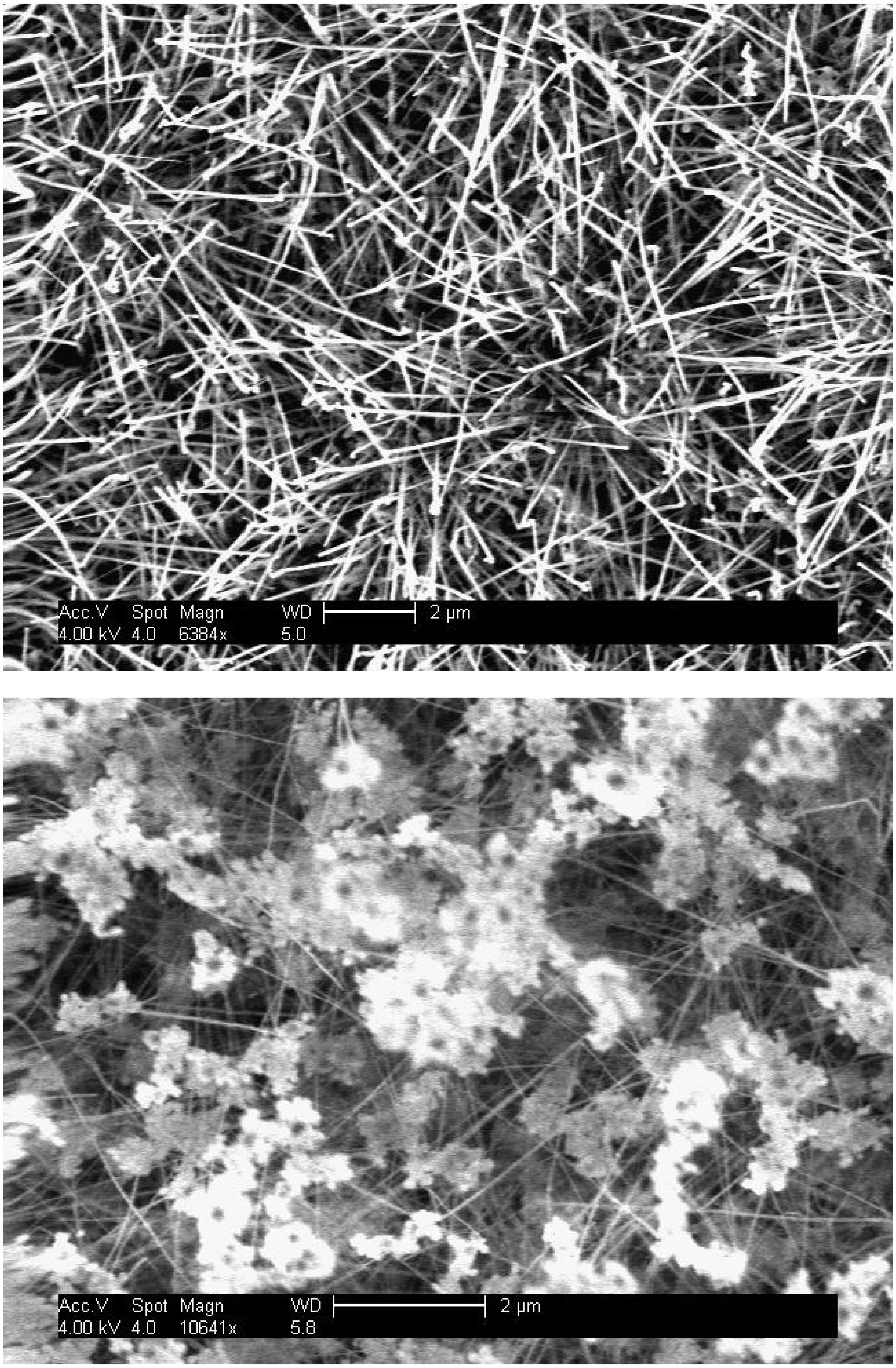

Figure 7.2: SEM images of BNNTs grown *via* the silicon chip method.

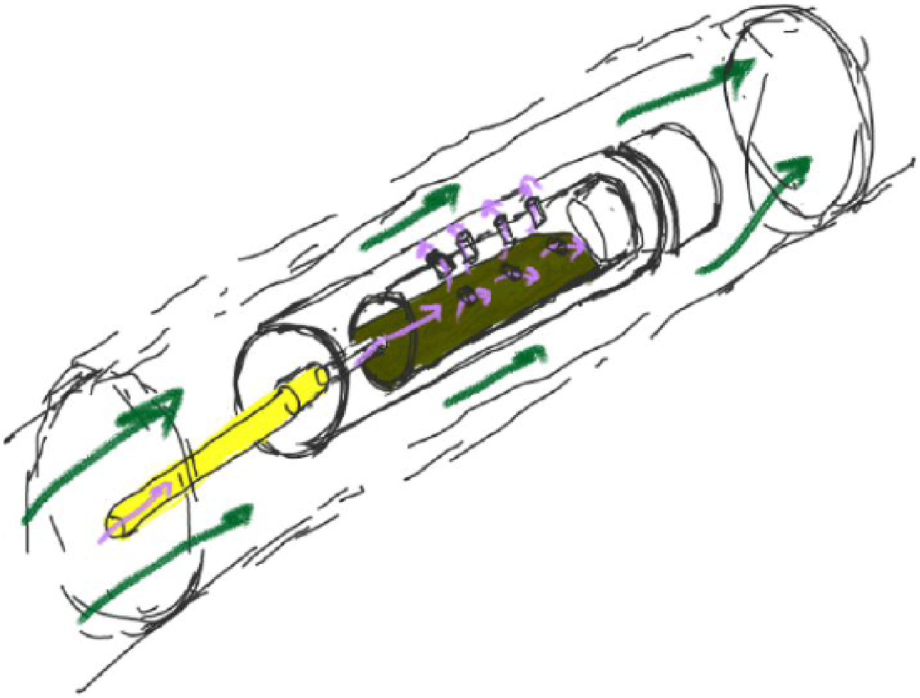

Figure 7.3: Schematic of sprinklerhead method for synthesizing BNNTs *via* the BOCVD method.

separated from the contaminants.

Sprinklerhead Method

One of the points stressed by Tang and Bando is that, in order to get good results, the ammonia and the precursor powder should be well separated. In the above process, the powder is exposed to the ammonia which tends to passivate it quickly. In an effort to improve the synthesis, I designed a new setup where the powder is kept in a separate BN tube and is carried into an ammonia region, as in Tang and Bando's original process.

Figure 7.3 shows a schematic of the apparatus. A blind $3/8$" cavity is first machined from a $1/2$" diameter BN rod; the blind end is drilled through with a $1/16$" hole, and on the exterior face a $1/8$" counterbore is drilled to allow for insertion of an alumina rod which delivers an inert carrier gas to the cavity. Small holes are drilled into the sides of the vessel out of which the reactive gases flow. The precursor powder is placed inside the cavity and the open end is capped off with a BN plug.

The assembly is placed in slipped into a quartz tube mounted in a horizontal resistance furnace, and the carrier gas is flowed at around 25 sccm while the temperature is raised to 1200 °C. Then, a flow of ammonia at around 40 sccm is introduced into the quartz, and reaction run for about 15 minutes. It is useful to monitor the pressure of the carrier gas, as

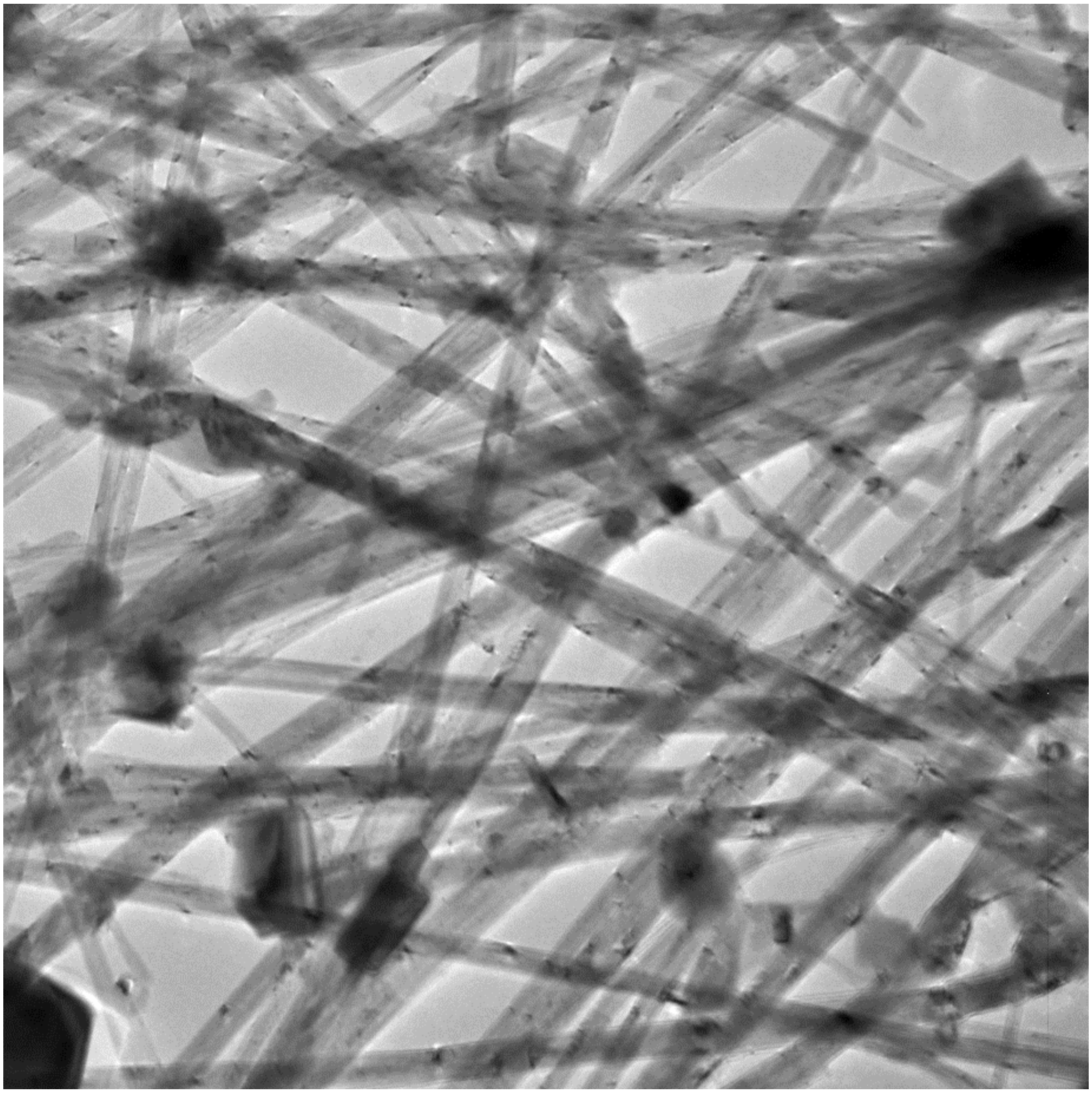

Figure 7.4: TEM image of BNNTs synthesized *via* the sprinklerhead method.

the small holes through which the reactive gases escape the cavity can easily become clogged up with magnesium oxide.

On successful runs, a fine, silky white material will condense on the exterior of the small holes in the vessel, which can be scraped off carefully with a spatula. It was found that in the most successful run, the precursor material remains a brownish-black color, indicating that no ammonia is able to diffuse into the cavity. The flow rate of the carrier gas needs to a adjusted appropriately in order to achieve this.

Figure 7.4 shows a TEM image of the resulting material. It is composed almost exclusively of multiwalled BNNTs with good crystallinity. The concentration of contaminants is relatively low. The alternating dark fringes are thought to be indications of a faceted structure on the surface of the tubes.[93]

7.2 Decomposition of Metal Borides

An alternative route is to consider the decomposition of metal borides, which can release boron upon decomposition. For example, in the case of iron boride, we have

$$\mathrm{FeB} \longrightarrow \mathrm{Fe} + \mathrm{B} \tag{7.3}$$

The boron can then subsequently react with ammonia via Equation 6.2 to form BN. The synthesis route was suggested by Dr. Zhengzong Sun, together with whom I conducted some experiments synthesizing BNNTs in this manner.

The approach was simply to take iron boride powder and heat it to high temperatures in the induction furnace under a flow of ammonia. The iron boride was sprinkled onto a 2" diameter graphite disk, which was placed in the center of the induction furnace chamber under sufficient insulation; the chamber was flushed with inert gas several times, after which about 5 kW of power was supplied. Induction heating heats the disk non-uniformly, with the exterior edge receiving a larger amount of powder. After reaching high temperature, a flow of about 200 sccm of ammonia was introduced, and the reaction was run for about 10 minutes. Upon cooling, the disk is removed and examined. A white fluffy substance can be found on the rim of the disk, while in the center, small iron particles remain.

Figure 7.5 shows an SEM image of BNNTs synthesized *via* decomposition of iron boride. It is evident that a large number of contaminants, presumably iron, boron, or iron boride particles decorate the tubes. The tubes are up to 10 microns long and are found tangled in bunches.

Figure 7.6 shows a TEM image of a BNNT from the same sample. The tube has fairly good crystalline quality, and is about 15 nm in diameter. The square end cap is typical of BNNTs.

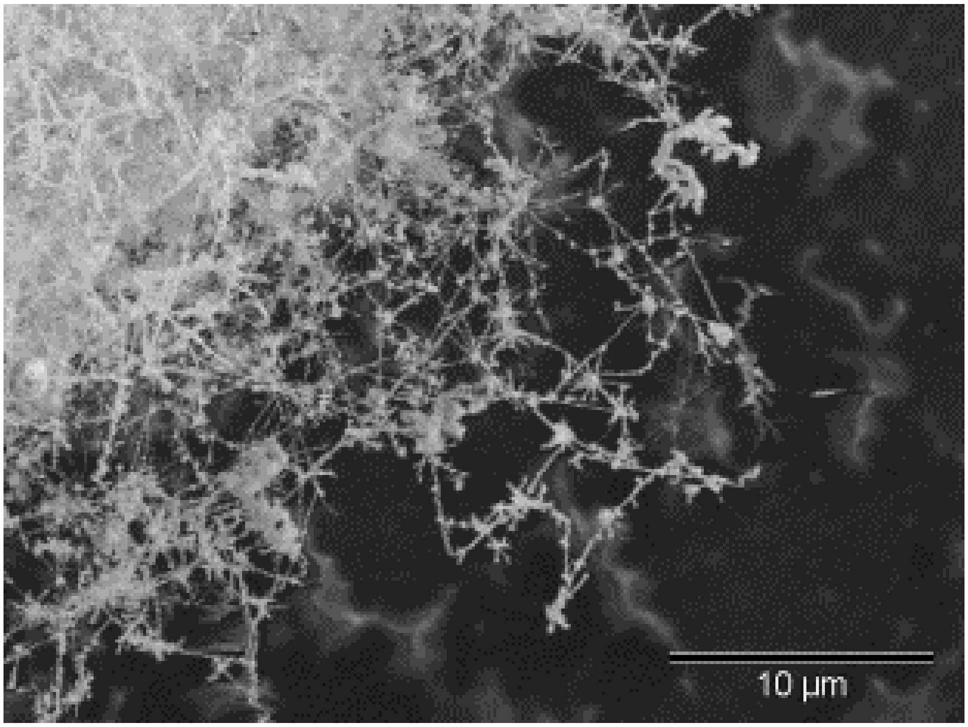

Figure 7.5: SEM image of BNNTs synthesized *via* decomposition of iron boride.

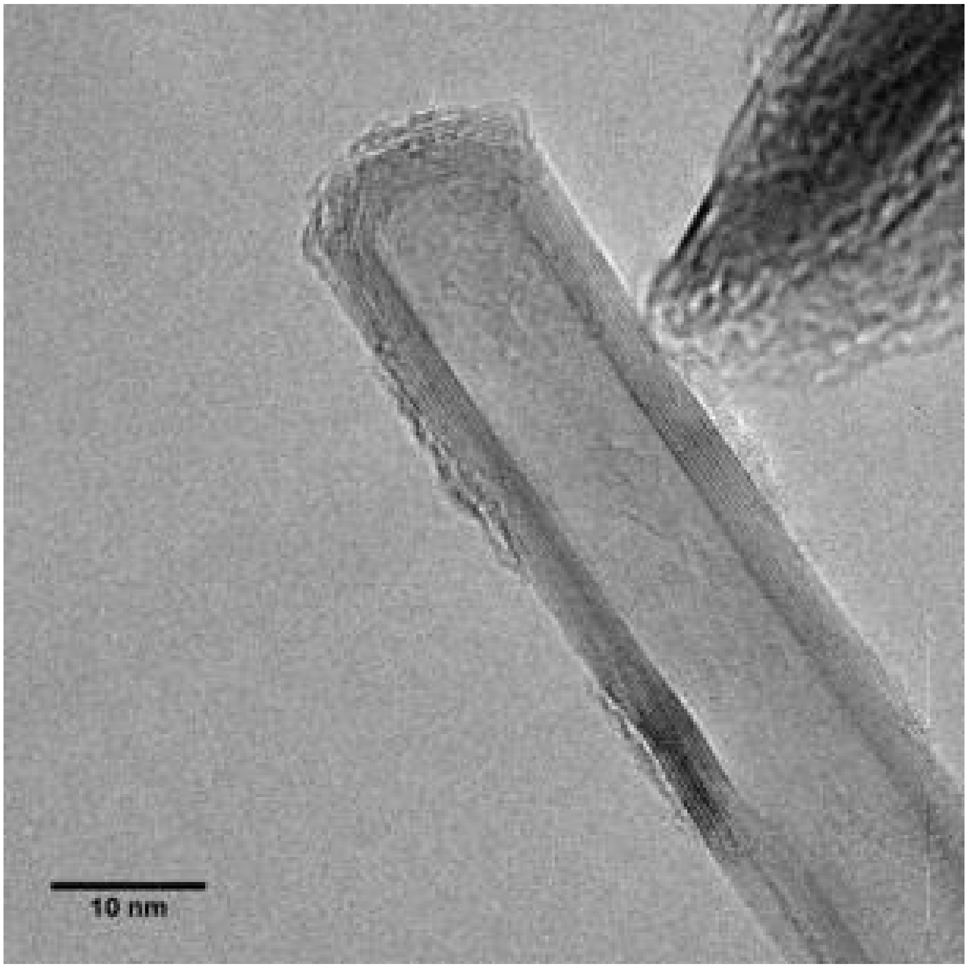

Figure 7.6: TEM image of a BNNT synthesized *via* decomposition of iron boride.

Bibliography

[1] Tim J Booth et al. "Macroscopic graphene membranes and their extraordinary stiffness." In: *Nano letters* 8.8 (Aug. 2008), pp. 2442–6. ISSN: 1530-6984. DOI: `10.1021/nl801412y`. URL: `http://www.ncbi.nlm.nih.gov/pubmed/18593201`.

[2] D Nelson. "The Statistical Mechanics of Membranes and Interfaces". In: *Statistical Mechanics of Membranes and Surfaces*. Ed. by David R. Nelson, T. Piran, and S. Weinberg. Singapore: World Scientific Publishing, 1989.

[3] Neville H. Fletcher and Thomas D. Rossing. *The Physics of Musical Instruments*. New York: Springer-Verlag, 1991.

[4] Changgu Lee et al. "Measurement of the elastic properties and intrinsic strength of monolayer graphene." In: *Science* 321.5887 (July 2008), pp. 385–8. ISSN: 1095-9203. DOI: `10.1126/science.1157996`. URL: `http://www.ncbi.nlm.nih.gov/pubmed/18635798`.

[5] L. D. Landau and E. M. Lifshitz. *Theory of Elasticity*. 3rd. Pergamon Press, 1986.

[6] M. Poot and H. S. J. van der Zant. "Nanomechanical properties of few-layer graphene membranes". In: *Applied Physics Letters* 92.6 (2008), p. 063111. ISSN: 00036951. DOI: `10.1063/1.2857472`. URL: `http://link.aip.org/link/APPLAB/v92/i6/p063111/s1\&Agg=doi`.

[7] Niklas Lindahl et al. "Determination of the bending rigidity of graphene via electrostatic actuation of buckled membranes." In: *Nano letters* 12.7 (July 2012), pp. 3526–31. ISSN: 1530-6992. DOI: `10.1021/nl301080v`. URL: `http://www.ncbi.nlm.nih.gov/pubmed/22708530`.

[8] D.-B. Zhang, E. Akatyeva, and T. Dumitrică. "Bending Ultrathin Graphene at the Margins of Continuum Mechanics". In: *Physical Review Letters* 106.25 (June 2011), p. 255503. ISSN: 0031-9007. DOI: `10.1103/PhysRevLett.106.255503`. URL: `http://link.aps.org/doi/10.1103/PhysRevLett.106.255503`.

[9] R Nicklow, N Wakabayashi, and HG Smith. "Lattice dynamics of pyrolytic graphite". In: *Physical Review B* 5 (1972), pp. 4951–4962. URL: `http://prb.aps.org/abstract/PRB/v5/i12/p4951\_1`.

[10] Qiang Lu, Marino Arroyo, and Rui Huang. "Elastic bending modulus of monolayer graphene". In: *Journal of Physics D: Applied Physics* 42.10 (May 2009), p. 102002. ISSN: 0022-3727. DOI: `10.1088/0022-3727/42/10/102002`. URL: `http://stacks.iop.org/0022-3727/42/i=10/a=102002?key=crossref.7b9cd79ee1443d013bc3d9c215937c03`.

[11] Konstantin Kudin, Gustavo Scuseria, and Boris Yakobson. "C2F, BN, and C nanoshell elasticity from ab initio computations". In: *Physical Review B* 64.23 (Nov. 2001), p. 235406. ISSN: 0163-1829. DOI: `10.1103/PhysRevB.64.235406`. URL: `http://link.aps.org/doi/10.1103/PhysRevB.64.235406`.

[12] Rudolph Szilard. *Theories and Applications of Plate Analysis.* Hoboken: John Wiley & Sons, Ltd., 2004.

[13] Konstantin V. Zakharchenko. "Tempeature effects on graphene: from flat cystal to 3D liquid". PhD thesis. 2011. ISBN: 9789081732901. arXiv: `arXiv:0903.3847`.

[14] William Regan et al. "A direct transfer of layer-area graphene". In: *Applied Physics Letters* 96 (2010), p. 113102. DOI: `10.1063/1.3337091`.

[15] Eugen Ermantraut, Klaus Wohlfart, and Willem Tichelaar. "Perforated support foils with pre-defined hole size, shape and arrangement". In: *Ultramicroscopy* 74.1-2 (July 1998), pp. 75–81. ISSN: 03043991. DOI: `10.1016/S0304-3991(98)00025-4`. URL: `http://linkinghub.elsevier.com/retrieve/pii/S0304399198000254`.

[16] Joel Quispe et al. "An improved holey carbon film for cryo-electron microscopy." In: *Microscopy and microanalysis* 13.5 (Oct. 2007), pp. 365–71. ISSN: 1431-9276. DOI: `10.1017/S1431927607070791`. URL: `http://www.ncbi.nlm.nih.gov/pubmed/17900388`.

[17] Robert a Barton et al. "High, size-dependent quality factor in an array of graphene mechanical resonators." In: *Nano letters* 11.3 (Mar. 2011), pp. 1232–6. ISSN: 1530-6992. DOI: `10.1021/nl1042227`. URL: `http://www.ncbi.nlm.nih.gov/pubmed/21294522`.

[18] R R Nair et al. "Fine structure constant defines visual transparency of graphene." In: *Science (New York, N.Y.)* 320.5881 (July 2008), p. 1308. ISSN: 1095-9203. DOI: `10.1126/science.1156965`. URL: `http://www.ncbi.nlm.nih.gov/pubmed/18388259`.

[19] Alexander a Balandin et al. "Superior thermal conductivity of single-layer graphene." In: *Nano letters* 8.3 (Mar. 2008), pp. 902–7. ISSN: 1530-6984. DOI: `10.1021/nl0731872`. URL: `http://www.ncbi.nlm.nih.gov/pubmed/18284217`.

[20] Nicolas Mounet and Nicola Marzari. "First-principles determination of the structural, vibrational and thermodynamic properties of diamond, graphite, and derivatives". In: *Physical Review B* 71.20 (May 2005), pp. 1–14. ISSN: 1098-0121. DOI: `10.1103/PhysRevB.71.205214`. URL: `http://link.aps.org/doi/10.1103/PhysRevB.71.205214`.

[21] Zhuangchun Wu et al. "Transparent, conductive carbon nanotube films." In: *Science* 305.5688 (Aug. 2004), pp. 1273–6. ISSN: 1095-9203. DOI: `10.1126/science.1101243`. URL: `http://www.ncbi.nlm.nih.gov/pubmed/15333836`.

[22] Christian Reichardt. *Solvents and Solvent Effects in Organic Chemistry.* 3rd. Wiley-VHC Publishers, 2003.

[23] M Paczuski, M Kardar, and DR Nelson. "Landau theory of the crumpling transition". In: *Physical review letters* 60.25 (1988), pp. 2638–2640. URL: `http://adsabs.harvard.edu/abs/1988PhRvL..60.2638P`.

[24] C. Moreno-Castilla and F.J. Maldonado-Hódar. "Carbon aerogels for catalysis applications: An overview". In: *Carbon* 43.3 (Jan. 2005), pp. 455–465. ISSN: 00086223. DOI: `10.1016/j.carbon.2004.10.022`. URL: `http://linkinghub.elsevier.com/retrieve/pii/S0008622304006037`.

[25] J. Lee, J. Kim, and T. Hyeon. "Recent Progress in the Synthesis of Porous Carbon Materials". In: *Advanced Materials* 18.16 (Aug. 2006), pp. 2073–2094. ISSN: 0935-9648. DOI: `10.1002/adma.200501576`. URL: `http://doi.wiley.com/10.1002/adma.200501576`.

[26] C Yin, M Aroua, and W Daud. "Review of modifications of activated carbon for enhancing contaminant uptakes from aqueous solutions". In: *Separation and Purification Technology* 52.3 (Jan. 2007), pp. 403–415. ISSN: 13835866. DOI: `10.1016/j.seppur.2006.06.009`. URL: `http://linkinghub.elsevier.com/retrieve/pii/S1383586606002024`.

[27] Deyang Qu and Hang Shi. "Studies of activated carbons used in double-layer capacitors". In: *Journal of Power Sources* 74.1 (July 1998), pp. 99–107. ISSN: 03787753. DOI: `10.1016/S0378-7753(98)00038-X`. URL: `http://linkinghub.elsevier.com/retrieve/pii/S037877539800038X`.

[28] Juergen Biener et al. "Advanced carbon aerogels for energy applications". In: *Energy and Environmental Science* 4.3 (2011), pp. 656–667. ISSN: 1754-5692. DOI: `10.1039/c0ee00627k`. URL: `http://xlink.rsc.org/?DOI=c0ee00627k`.

[29] Ying Chen et al. "Boron nitride nanotubes: Pronounced resistance to oxidation". In: *Applied Physics Letters* 84.13 (2004), pp. 2430–2432. ISSN: 00036951. DOI: `10.1063/1.1667278`. URL: `http://link.aip.org/link/APPLAB/v84/i13/p2430/s1\&Agg=doi`.

[30] Seung-Hoon Jhi and Young-Kyun Kwon. "Hydrogen adsorption on boron nitride nanotubes: A path to room-temperature hydrogen storage". In: *Physical Review B* 69.24 (June 2004), p. 245407. ISSN: 1098-0121. DOI: `10.1103/PhysRevB.69.245407`. URL: `http://link.aps.org/doi/10.1103/PhysRevB.69.245407`.

[31] Weiwei Lei et al. "Porous boron nitride nanosheets for effective water cleaning". en. In: *Nature Communications* 4 (Apr. 2013), p. 1777. ISSN: 2041-1723. DOI: `10.1038/ncomms2818`. URL: `http://www.nature.com/ncomms/journal/v4/n4/full/ncomms2818.html\#affil-auth`.

[32] TT Borek et al. "Highly microporous boron nitride for gas adsorption". In: *Langmuir* 73.3 (1991), pp. 2844–2846. URL: `http://pubs.acs.org/doi/abs/10.1021/la00059a070`.

[33] Jie Li et al. “Porous boron nitride with a high surface area: hydrogen storage and water treatment”. In: *Nanotechnology* 24 (2013), p. 155603. DOI: `10.1088/0957-4484/24/15/155603`.

[34] Renzhi Ma et al. “Hydrogen Uptake in Boron Nitride Nanotubes at Room Temperature”. In: *Journal of the American Chemical Society* 124 (2002), pp. 7672–7673.

[35] Jinhong Kim et al. “High-surface area ceramic-derived boron-nitride and its hydrogen uptake properties”. In: *Journal of Materials Chemistry A* 1.4 (2013), pp. 1014–1017. ISSN: 2050-7488. DOI: `10.1039/c2ta00904h`. URL: `http://xlink.rsc.org/?DOI=c2ta00904h`.

[36] Qunhong Weng et al. “Boron Nitride Porous Microbelts for Hydrogen Storage”. In: *ACS Nano* 7.2 (2013), pp. 1558–1565. URL: `http://pubs.acs.org/doi/abs/10.1021/nn305320v`.

[37] Jurik F Janik et al. “Boron Nitride as a Selective Gas Adsorbent”. In: *Langmuir* 10 (1994), pp. 514–518.

[38] R. T. Paine and Chaitanya K. Narula. “Synthetic Routes to Boron Nitride”. In: *Chemical Reviews* 90 (1990), pp. 73–91.

[39] C Schafhaeutl. “On the combinations of carbon with silicon and iron, and other metals, forming the different species of cast iron, steel, and malleable iron”. In: *Philosophical Magazine* 16.104 (1840), pp. 570–90. URL: `http://www.tandfonline.com/doi/pdf/10.1080/14786444008650094`.

[40] William S. Hummers and Richard E. Offeman. “Preparation of Graphitic Oxide”. In: *Journal of the American Chemical Society* 80.6 (Mar. 1958), pp. 1339–1339. ISSN: 0002-7863. DOI: `10.1021/ja01539a017`. URL: `http://pubs.acs.org/doi/pdf/10.1021/ja01539a017http://pubs.acs.org/doi/abs/10.1021/ja01539a017`.

[41] Daniel R Dreyer et al. “The chemistry of graphene oxide.” In: *Chemical Society reviews* 39.1 (Jan. 2010), pp. 228–40. ISSN: 1460-4744. DOI: `10.1039/b917103g`. URL: `http://www.ncbi.nlm.nih.gov/pubmed/20023850`.

[42] Anton Lerf et al. “Structure of Graphite Oxide Revisited”. In: *The Journal of Physical Chemistry B* 102.23 (June 1998), pp. 4477–4482. ISSN: 1520-6106. DOI: `10.1021/jp9731821`. URL: `http://pubs.acs.org/doi/abs/10.1021/jp9731821`.

[43] Luis R. De Jesus et al. “Inside and Outside: X-ray Absorption Spectroscopy Mapping of Chemical Domains in Graphene Oxide”. In: *The Journal of Physical Chemistry Letters* 4.18 (Sept. 2013), pp. 3144–3151. ISSN: 1948-7185. DOI: `10.1021/jz401717j`. URL: `http://pubs.acs.org/doi/abs/10.1021/jz401717j`.

[44] Radosav S Pantelic et al. “Graphene oxide: a substrate for optimizing preparations of frozen-hydrated samples.” In: *Journal of structural biology* 170.1 (Apr. 2010), pp. 152–6. ISSN: 1095-8657. DOI: `10.1016/j.jsb.2009.12.020`. URL: `http://www.ncbi.nlm.nih.gov/pubmed/20035878`.

[45] Kris Erickson et al. "Determination of the local chemical structure of graphene oxide and reduced graphene oxide." In: *Advanced materials (Deerfield Beach, Fla.)* 22.40 (Oct. 2010), pp. 4467–72. ISSN: 1521-4095. DOI: `10.1002/adma.201000732`. URL: `http://www.ncbi.nlm.nih.gov/pubmed/20717985`.

[46] Si Zhou and Angelo Bongiorno. "Origin of the chemical and kinetic stability of graphene oxide." In: *Scientific reports* 3 (Aug. 2013), p. 2484. ISSN: 2045-2322. DOI: `10.1038/srep02484`. URL: `http://www.pubmedcentral.nih.gov/articlerender.fcgi?artid=3748429\&tool=pmcentrez\&rendertype=abstract`.

[47] Deepak K. Pandey et al. "Folding and cracking of graphene oxide sheets upon deposition". In: *Surface Science* 605.17-18 (Sept. 2011), pp. 1669–1675. ISSN: 00396028. DOI: `10.1016/j.susc.2011.04.034`. URL: `http://linkinghub.elsevier.com/retrieve/pii/S0039602811001713`.

[48] Je-Luen Li et al. "Oxygen-Driven Unzipping of Graphitic Materials". In: *Physical Review Letters* 96.17 (May 2006), p. 176101. ISSN: 0031-9007. DOI: `10.1103/PhysRevLett.96.176101`. URL: `http://link.aps.org/doi/10.1103/PhysRevLett.96.176101`.

[49] Raymond L D Whitby et al. "Driving forces of conformational changes in single-layer graphene oxide." In: *ACS nano* 6.5 (May 2012), pp. 3967–73. ISSN: 1936-086X. DOI: `10.1021/nn3002278`. URL: `http://www.pubmedcentral.nih.gov/articlerender.fcgi?artid=3357922\&tool=pmcentrez\&rendertype=abstract`.

[50] Sasha Stankovich et al. "Synthesis of graphene-based nanosheets via chemical reduction of exfoliated graphite oxide". In: *Carbon* 45.7 (June 2007), pp. 1558–1565. ISSN: 00086223. DOI: `10.1016/j.carbon.2007.02.034`. URL: `http://linkinghub.elsevier.com/retrieve/pii/S0008622307000917`.

[51] Yuxi Xu et al. "Self-assembled graphene hydrogel via a one-step hydrothermal process." In: *ACS nano* 4.7 (July 2010), pp. 4324–30. ISSN: 1936-086X. DOI: `10.1021/nn101187z`. URL: `http://www.ncbi.nlm.nih.gov/pubmed/20590149`.

[52] Marcus a Worsley et al. "Synthesis of graphene aerogel with high electrical conductivity." In: *Journal of the American Chemical Society* 132.40 (Oct. 2010), pp. 14067–9. ISSN: 1520-5126. DOI: `10.1021/ja1072299`. URL: `http://www.ncbi.nlm.nih.gov/pubmed/20860374`.

[53] MA Worsley, TY Olson, and JRI Lee. "High surface area, sp2-cross-linked three-dimensional graphene monoliths". In: *Journal of Physical Chemistry Letters* 2 (2011), pp. 921–925. URL: `http://pubs.acs.org/doi/abs/10.1021/jz200223x`.

[54] Marcus a Worsley et al. "Mechanically robust 3D graphene macroassembly with high surface area." In: *Chemical Communications* 48.67 (Aug. 2012), pp. 8428–30. ISSN: 1364-548X. DOI: `10.1039/c2cc33979j`. URL: `http://www.ncbi.nlm.nih.gov/pubmed/22797515`.

[55] Francisco Rodríguez-Reinoso et al. “The reduction of graphene oxide”. In: *Carbon* 50.9 (2012), pp. 3210–3228. URL: `http://www.sciencedirect.com/science/article/pii/S0008622311008967`.

[56] Parambath M Sudeep et al. “Covalently interconnected three-dimensional graphene oxide solids.” In: *ACS nano* 7.8 (Aug. 2013), pp. 7034–40. ISSN: 1936-086X. DOI: `10.1021/nn402272u`. URL: `http://www.ncbi.nlm.nih.gov/pubmed/23845011`.

[57] MS Spector et al. “Conformations of a tethered membrane: Crumpling in graphitic oxide?” In: *Physical review letters* 73.21 (1994), p. 2867. URL: `http://prl.aps.org/abstract/PRL/v73/i21/p2867\_1`.

[58] TA Witten and H Li. “Asymptotic shape of a fullerene ball”. In: *EPL (Europhysics Letters)* 23 (1993), pp. 51–55. URL: `http://iopscience.iop.org/0295-5075/23/1/009`.

[59] Weiqiang Han et al. “Synthesis of boron nitride nanotubes from carbon nanotubes by a substitution reaction”. In: *Applied Physics Letters* 73.21 (1998), pp. 3085–3087. ISSN: 00036951. DOI: `10.1063/1.122680`. URL: `http://link.aip.org/link/APPLAB/v73/i21/p3085/s1\&Agg=doi`.

[60] T. Witten. “Stress focusing in elastic sheets”. In: *Reviews of Modern Physics* 79.2 (Apr. 2007), pp. 643–675. ISSN: 0034-6861. DOI: `10.1103/RevModPhys.79.643`. URL: `http://link.aps.org/doi/10.1103/RevModPhys.79.643`.

[61] A. A. Giardini. *Boron Nitride*. Washington, D.C.: U.S. Dept. of the Interior, Bureau of Mines, 1953. URL: `http://catalog.hathitrust.org/Record/005889245`.

[62] A. Aydoğdu and N. Sevinç. “Carbothermic formation of boron nitride”. In: *Journal of the European Ceramic Society* 23.16 (Dec. 2003), pp. 3153–3161. ISSN: 09552219. DOI: `10.1016/S0955-2219(03)00092-X`. URL: `http://linkinghub.elsevier.com/retrieve/pii/S095522190300092X`.

[63] Anton Meller. “The System Boron-Nitrogen”. In: *Gmelin Handbook of inorganic and organometallic chemistry*. Berlin: Springer-Verlag, 1992.

[64] T S Bartnitskaya et al. “Structure and Some Properties of Fine-Grained Graphite-Like Boron Nitride”. In: *Journal of Less-Common Metals* 117 (1986), pp. 253–258.

[65] Wei-Qiang Han et al. “Activated Boron Nitride Derived from Activated Carbon”. In: *Nano Letters* 4.1 (Jan. 2004), pp. 173–176. ISSN: 1530-6984. DOI: `10.1021/nl034843a`. URL: `http://pubs.acs.org/doi/abs/10.1021/nl034843a`.

[66] a.R. Bushroa et al. “Approximation of crystallite size and microstrain via XRD line broadening analysis in TiSiN thin films”. In: *Vacuum* 86.8 (Feb. 2012), pp. 1107–1112. ISSN: 0042207X. DOI: `10.1016/j.vacuum.2011.10.011`. URL: `http://linkinghub.elsevier.com/retrieve/pii/S0042207X11003745`.

[67] RJ Nemanich, SA Solin, and RM Martin. “Light scattering study of boron nitride microcrystals”. In: *Physical Review B* 23 (1981), pp. 6348–6356. URL: `http://prb.aps.org/abstract/PRB/v23/i12/p6348\_1`.

[68] R. F. Egerton. *Electron Energy-Loss Spectroscopy in the Electron Microscope*. 2nd. New York: Plenum Press, 1996.

[69] O. P. Bahl et al. “Manufacture of Carbon Fibers”. In: *Carbon Fibers*. Ed. by Jean-Baptiste Donnet et al. 3rd. New York: Marcel Dekker, 1998, pp. 1–83.

[70] Mildred S Dresselhaus et al. *Graphite Fibers and Filaments*. New York: Springer-Verlag, 1988.

[71] Sara Black. *Carbon fiber market: Gathering momentum*. URL: `http://www.compositesworld.com/articles/carbon-fiber-market-gathering-momentum`.

[72] J Economy and RV Anderson. “Boron nitride fibers”. In: *Journal of Polymer Science Part C: ...* 297.19 (1967), pp. 283–297. URL: `http://onlinelibrary.wiley.com/doi/10.1002/polc.5070190122/abstract`.

[73] B. Toury et al. “Complete characterisation of BN fibres obtained from a new polyborylborazine”. In: *Journal of the European Ceramic Society* 25.2-3 (Jan. 2005), pp. 137–141. ISSN: 09552219. DOI: `10.1016/j.jeurceramsoc.2004.07.022`. URL: `http://linkinghub.elsevier.com/retrieve/pii/S0955221904003218`.

[74] Y. Kimura, Y. Kubo, and N. Hayashi. “High-performance boron-nitride fibers from poly(borazine) preceramics”. In: *Composites Science and Technology* 51.2 (Jan. 1994), pp. 173–179. ISSN: 02663538. DOI: `10.1016/0266-3538(94)90188-0`. URL: `http://linkinghub.elsevier.com/retrieve/pii/0266353894901880`.

[75] RW Rice. “BN coating of ceramic fibers for ceramic fiber composites”. In: *US Patent 4,642,271* (1987). URL: `http://www.google.com/patents?hl=en\&lr=\&vid=USPAT4642271\&id=6cwuAAAAEBAJ\&oi=fnd\&dq=BN+Coating+of+Ceramic+Fibers+for+Ceramic+Fiber+Composites\&printsec=abstract`.

[76] D Golberg et al. “Single-walled B-doped carbon , B/N-doped carbon and BN nanotubes synthesized from single-walled carbon nanotubes through a substitution reaction”. In: *Chemical Physics Letters* July (1999), pp. 337–342.

[77] Marcus a. Worsley et al. “Mechanically robust and electrically conductive carbon nanotube foams”. In: *Applied Physics Letters* 94.7 (2009), p. 073115. ISSN: 00036951. DOI: `10.1063/1.3086293`. URL: `http://link.aip.org/link/APPLAB/v94/i7/p073115/s1\&Agg=doi`.

[78] C R Dean et al. “Boron nitride substrates for high-quality graphene electronics.” In: *Nature Nanotechnology* 5.10 (Oct. 2010), pp. 722–726. ISSN: 1748-3395. DOI: `10.1038/nnano.2010.172`. URL: `http://www.ncbi.nlm.nih.gov/pubmed/20729834`.

[79] Matthew Yankowitz et al. "Emergence of superlattice Dirac points in graphene on hexagonal boron nitride". In: *Nature Physics* 8.5 (Mar. 2012), pp. 382–386. ISSN: 1745-2473. DOI: `10.1038/nphys2272`. URL: `http://www.nature.com/doifinder/10.1038/nphys2272`.

[80] Ki Kang Kim et al. "Synthesis of monolayer hexagonal boron nitride on Cu foil using chemical vapor deposition." In: *Nano letters* 12.1 (Jan. 2012), pp. 161–6. ISSN: 1530-6992. DOI: `10.1021/nl203249a`. URL: `http://www.ncbi.nlm.nih.gov/pubmed/22111957`.

[81] B Glorieux, M. L. Saboungi, and J. E. Enderby. "Electronic conduction in liquid boron". In: *Europhysics Letters* 56.1 (2001), pp. 81–85. URL: `http://iopscience.iop.org/0295-5075/56/1/081`.

[82] Sumio Iijima. "Helical microtubules of graphitic carbon". In: *Nature* 354 (1991), pp. 56–58. URL: `http://www.nature.com/physics/looking-back/iijima/`.

[83] O Stephan et al. "Doping graphitic and carbon nanotube structures with boron and nitrogen." In: *Science* 266.5191 (Dec. 1994), pp. 1683–5. ISSN: 0036-8075. DOI: `10.1126/science.266.5191.1683`. URL: `http://www.ncbi.nlm.nih.gov/pubmed/17775629`.

[84] NG Chopra and RJ Luyken. "Boron nitride nanotubes". In: *SCIENCE-NEW YORK ...* 269 (1995), pp. 966–967. URL: `http://www.phys.psu.edu/~crespi/docs/BNSynthesis.pdf`.

[85] John Cumings and A Zettl. "Mass-production of boron nitride double-wall nanotubes and nanococoons". In: January (2000), pp. 211–216.

[86] C.M. Lee et al. "Synthesis of boron nitride nanotubes by arc-jet plasma". In: *Current Applied Physics* 6.2 (Feb. 2006), pp. 166–170. ISSN: 15671739. DOI: `10.1016/j.cap.2005.07.032`. URL: `http://linkinghub.elsevier.com/retrieve/pii/S1567173905001793`.

[87] D. Golberg et al. "Nanotubes in boron nitride laser heated at high pressure". In: *Applied Physics Letters* 69.14 (1996), p. 2045. ISSN: 00036951. DOI: `10.1063/1.116874`. URL: `http://link.aip.org/link/APPLAB/v69/i14/p2045/s1\&Agg=doi`.

[88] R. Lee et al. "Catalyst-free synthesis of boron nitride single-wall nanotubes with a preferred zig-zag configuration". In: *Physical Review B* 64.12 (Sept. 2001), p. 121405. ISSN: 0163-1829. DOI: `10.1103/PhysRevB.64.121405`. URL: `http://link.aps.org/doi/10.1103/PhysRevB.64.121405`.

[89] Michael W Smith et al. "Very long single- and few-walled boron nitride nanotubes via the pressurized vapor/condenser method." In: *Nanotechnology* 20.50 (Dec. 2009), p. 505604. ISSN: 1361-6528. DOI: `10.1088/0957-4484/20/50/505604`. URL: `http://www.ncbi.nlm.nih.gov/pubmed/19907071`.

[90] Raul Arenal et al. "Root-growth mechanism for single-walled boron nitride nanotubes in laser vaporization technique." In: *Journal of the American Chemical Society* 129.51 (Dec. 2007), pp. 16183–9. ISSN: 1520-5126. DOI: `10.1021/ja076135n`. URL: `http://www.ncbi.nlm.nih.gov/pubmed/18052251`.

[91] R. Arenal, M. Kociak, and N. J. Zaluzec. "High-angular-resolution electron energy loss spectroscopy of hexagonal boron nitride". In: *Applied Physics Letters* 90.20 (2007), p. 204105. ISSN: 00036951. DOI: `10.1063/1.2740185`. URL: `http://link.aip.org/link/APPLAB/v90/i20/p204105/s1\&Agg=doi`.

[92] Chengchun Tang et al. "A novel precursor for synthesis of pure boron nitride nanotubes." In: *Chemical communications (Cambridge, England)* 2.12 (June 2002), pp. 1290–1. ISSN: 1359-7345. URL: `http://www.ncbi.nlm.nih.gov/pubmed/12109120`.

[93] Amir Pakdel et al. "A comprehensive analysis of the CVD growth of boron nitride nanotubes." In: *Nanotechnology* 23.21 (June 2012), p. 215601. ISSN: 1361-6528. DOI: `10.1088/0957-4484/23/21/215601`. URL: `http://www.ncbi.nlm.nih.gov/pubmed/22551670`.